ORBITAL AND FLIGHT STABILITY MODELS FOR BREAKTHROUGH STARSHOT'S AO SYSTEM

by

Matthew Ryan Noyes

A Thesis Submitted to the Faculty of the

JAMES C. WYANT COLLEGE OF OPTICAL SCIENCES

In Partial Fulfillment of the Requirements
For the Degree of

MASTER OF SCIENCE

In the Graduate College

THE UNIVERSITY OF ARIZONA

2020

THE UNIVERSITY OF ARIZONA
GRADUATE COLLEGE

As members of the Master's Committee, we certify that we have read the thesis prepared by **Matthew Ryan Noyes**, titled ***Orbital and Flight Stability Models for Breakthrough Starshot's AO System*** and recommend that it be accepted as fulfilling the thesis requirement for the Master's Degree.

Professor Michael Hart, Chair Date: May 12, 2020

Professor Daewook Kim Date: 5-12-2020

Professor J. Roger P. Angel Date: May 12, 2020

Final approval and acceptance of this thesis is contingent upon the candidate's submission of the final copies of the thesis to the Graduate College.

I hereby certify that I have read this thesis prepared under my direction and recommend that it be accepted as fulfilling the Master's requirement.

Professor Michael Hart Date: 5/28/2020
Master's Thesis Committee Chair
Wyant College of Optical Sciences

Acknowledgements

To Dr. Hart: For a long time, I had this idea that I would need *years* of experience before I would be ready to work on advanced astronomical optical systems. After taking your courses and joining your group, I discovered a confidence in myself that allowed to me to accomplish so much more than I would have thought in my internships and thesis work. Your leadership and the attention you gave me is without question a large part of what allowed me to obtain the job I have always wanted. So thank you, Michael, for your guidance and support, and for helping me grow as an optical engineer. I am so very happy to have had you as my advisor.

To my friends: Thank you for the being there with me through some of the most fun and most challenging times of our lives. I will forever cherish the memories spent adventuring, relaxing, and staying up late studying together. The compassion and care you gave me and the times we spent together are what kept me grounded when things got stressful. As hard as it was for all of us to have had our last semester taken from us, I cannot wait to see how much you achieve and to make new memories together in the future.

To my parents: Your confidence in me and interest in my passions are, throughout my life, what enabled me to soar so high in my education. You both showed me what hard work and dedication really meant, and those lessons helped me achieve more than I could have ever imagined. You both have given me endless love and support and I am so incredibly happy to have you two as my parents. You have set me up for an incredible future, and I cannot wait to show to where it takes me. Thank you, Mom and Dad, because you both are why I have been able to achieve my dreams.

TABLE OF CONTENTS

LIST OF FIGURES

LIST OF TABLES

ABSTRACT

Breakthrough Starshot is an international engineering project which aims to develop a spacecraft launch system capable of reaching our nearest star neighbors in under 1 human lifetime. To achieve such high-speed interstellar travel, the Starshot system plans to accelerate an ultra-lightweight nanocraft with 100 GW of radiation pressure. This laser light will come from a massive ground-based launch projector and will focus through the atmosphere onto a 4 meter wide lightsail attached to the nanocraft. With 10 minutes of continuous laser power, the force of this light can accelerate a 1g nanocraft to 20% the speed of light. Such speeds can enable travelling to our nearest star neighbor in just 20 years.

For the laser to effectively focus on the nanocraft after traversing the turbulence of Earth's atmosphere, the Starshot system will need an Adaptive Optics system to 'pre-correct' the beam before transmission. To measure the distorting effects of the atmosphere, an artificial beacon must be placed high in altitude near the nanocraft through its launch. Proposed is a satellite-based laser guide star (SLGS) which will be attached to the mothercraft satellite which releases the nanocraft during launch. However, the satellite's lateral and radial motion in the sky from the nanocraft threatens to introduce angular and focal anisoplanatic errors, respectively, that would make proper adaptive correction impossible. By creating a fully parameterizable orbital simulation of the mothercraft and nanocraft's positions relative to the launch projector, it was found that there exist orbital configurations which keep these anisoplanatic errors within reason. One such orbit has an orbital period of 4 days and an eccentricity of 0.88.

Following adaptive correction, it is vital that residual wavefront error does not introduce perturbances which cause the sail to fall out of the beam. Given that the sail behaves like a particle trapped in a potential well, a statistical model was created which was used to determine the likelihood a sail would fall out of a beam. This model, coupled with a dynamic numerical simulation of a sail riding in a beam with a given distribution of residual tilt error, was used to determine that the Starshot system is expected to be highly intolerant to residual tip/tilt errors. It is recommended that future work involve identifying a method for dampening the sail's lateral energy throughout launch.

1. INTRODUCTION

Breakthrough Starshot is an international research and engineering project to develop a spacecraft system capable of achieving high-speed interstellar travel. High-speed in this context means considerable fractions of the speed of light. At such speeds, a spacecraft could travel to nearby stars within a human lifetime. Starshot's high-speed spacecraft would allow our species to begin the exploration of our galaxy and to survey other worlds for habitability and potential future colonization. It could even lead to discovery of life elsewhere in the Milky Way. High-speed interstellar travel, until recently, has been nothing more than science fiction; today's fastest rocket propelled spacecraft would take over 70,000 years to reach our nearest star neighbor. However, advancements in science and technology over the past 2 decades have revealed that it may be possible to visit another star within the next 60 years[1].

The current impossibility of high-speed interstellar travel is a problem of distance and acceleration. The 10 closest stars to our solar system range 4.24-11 lightyears, or 24-65 trillion miles, from the Earth. These massive distances are the reason travel with rocket propelled spacecraft would take millennia, even with cruise speeds of 10 miles per second. Travel time could be reduced by building bigger rockets with higher accelerations and top speeds, but the heavier a rocket is the more of its propellent is used to lift itself instead of accelerating its payload. To solve this problem, a new propulsion system with either a greater force or smaller launch mass must be developed.

The Breakthrough Starshot propulsion system proposes this new concept. This system aims to achieve high acceleration with the use of ultra-lightweight spacecraft (referred to as the nanocraft) which would house all the same sensor and communications suites as modern day space probes. These nanocraft would be affixed to a 4 meter wide sail and be accelerated by light (Figure 1). A lightsail would operate similar to sails of a boat, but with light in place of wind to accelerate the nanocraft. This light would come in the form of laser light from a 4km wide ground based projection system (Figure 2). With 100 GW of laser power focused onto the sail of a 1g nanocraft, it would only take 10 minutes to accelerate the nanocraft to 130 million mph (1/5 the speed of light)[2]. At this speed, a nanocraft could reach our nearest star neighbor (Proxima Centauri) in only 20 years.

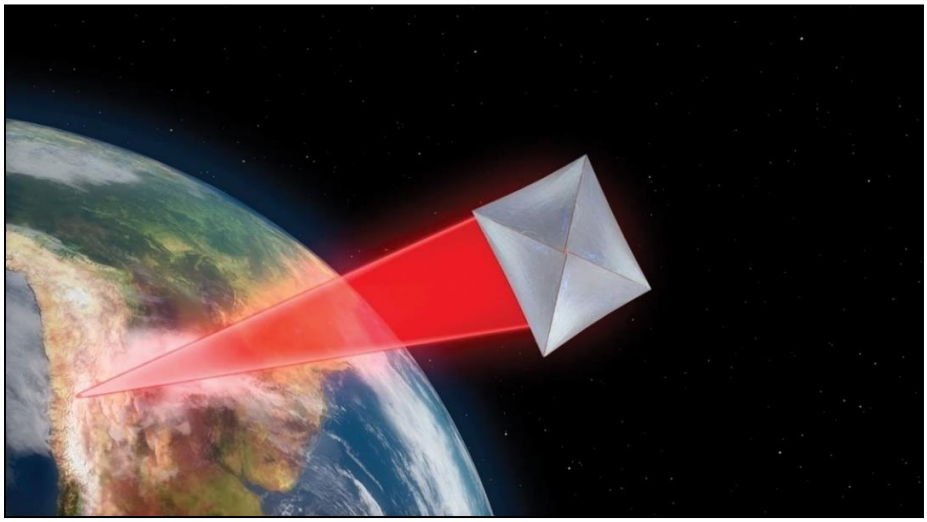

Figure 1 – The Starshot Nanocraft Lightsail Riding a Beam of Light[3]

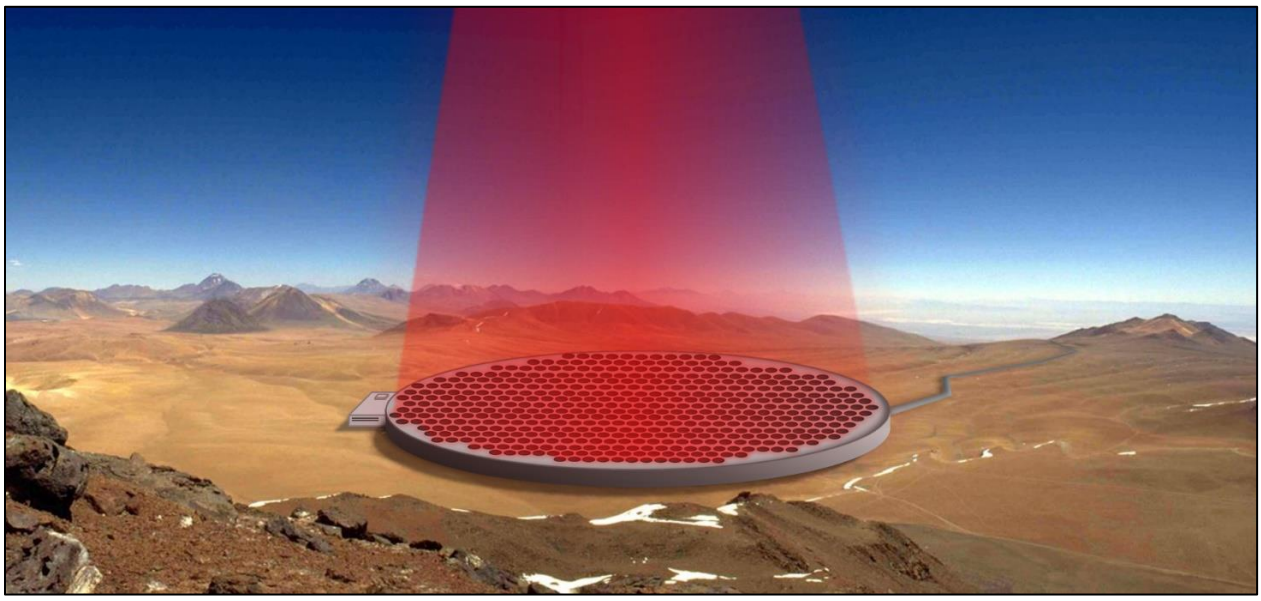

Figure 2 – The Starshot Launch Projector

In order for this laser projector to accelerate the nanocraft from its position on Earth, its beam needs to be well aimed and focused onto the lightsail throughout a 10 minute interaction period. This 10 minute laser-lightsail interaction is what provides propulsion and is referred to as the nanocraft's launch period. However, the nanocraft will be placed in orbit before the activation of the laser, causing the beam to travel through Earth's turbulent atmosphere before reaching the nanocraft. The atmosphere causes the laser's focus to blur and its aim to deflect which causes most of the projector's light to miss the nanocraft. To assure the laser light effectively transfers its momentum onto the lightsail, an Adaptive Optics (AO) system will need to be designed for the laser projection system[4].

1.1 Adaptive Optics

Adaptive Optics are used to remove both internal and external aberrations from optical systems. Internal aberrations are those caused by component misalignments or imperfections in optical elements, while external aberrations are caused by disturbances in the air through an optical system's line of sight. AO systems were first developed for use on astronomical telescopes and this remains one of their most common uses. Most astronomical targets are far away and extremely dim and, without adaptive correction, would be impossible to resolve through the turbulence of the atmosphere.

An AO system enhances an optical system's performance by reshaping the wavefronts captured by the system. A wavefront is defined as the surface passing through all points with the same phase of a propagating light wave and are always perpendicular to the direction of travel (i.e. perpendicular to the direction of light rays). In unaberrated systems, wavefronts are usually planar or spherical, and are manipulated passively by lenses and mirrors to form images (Figure 3).

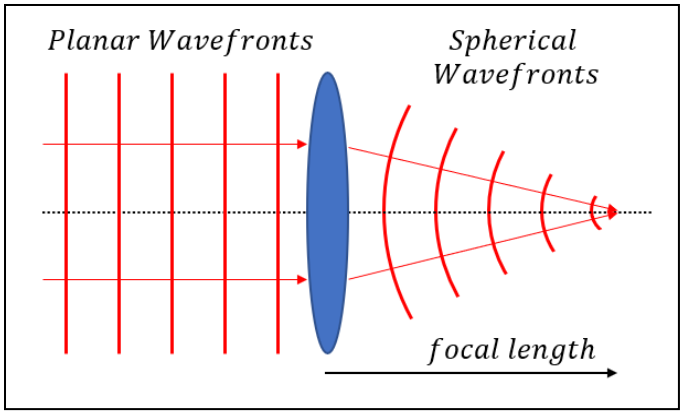

Figure 3 – Unaberrated System Wavefronts

An unaberrated system is able to focus down to a small spot, the size of which is limited by diffraction caused by the edge of the system's aperture. This means that an optical system always has some intrinsic 'blur' and the image of a perfect point will spread out to some finite spot size. The function that describes this spread is a system's Point Spread Function or PSF[5]. The diffraction limited PSF of a system with a circular aperture has the shape of an Airy Disk[6]. The diameter of this disk is

$$D_{airy} = 2.44\lambda F_{\#} \quad \textbf{(1)}$$

The airy disk's diameter is defined as the distance to the first dark ring of a focused spot (Figure 4).

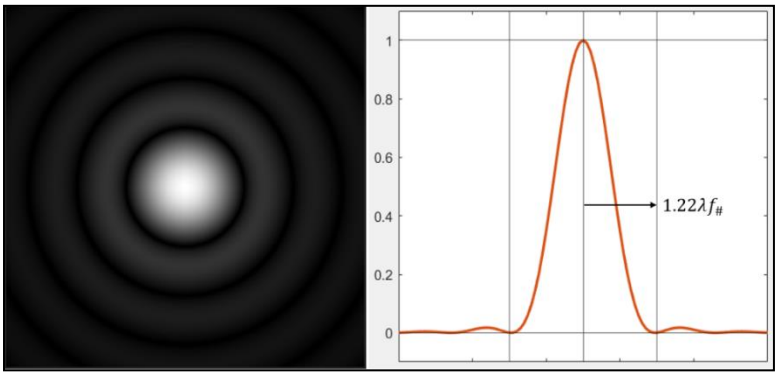

Figure 4 – Airy Disk Irradiance Pattern and its Cross Section

In the presence of atmospheric turbulence or significant optical aberrations, wavefronts are distorted into non-planar or non-spherical shapes (Figure 5). This results in a PSF which is spread beyond its diffraction limit, resulting in a blurred image. "Wavefront error" is the term used to describe the difference between an aberrated wavefront and its ideal counterpart.

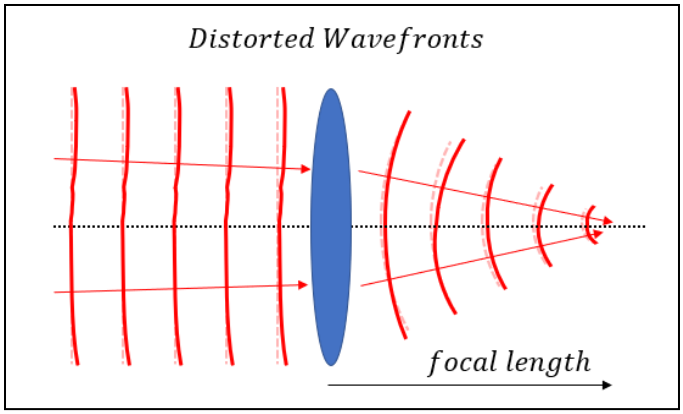

Figure 5 – Aberrated System Wavefronts

The Strehl ratio[7] is a metric that describes the quality of an optical system relative to a perfect one. It is defined as the ratio between the peak irradiance of an aberrated spot to the peak irradiance of a diffraction limited (unaberrated) spot. In Figure 6, the Strehl ratio of the aberrated spot is 0.8.

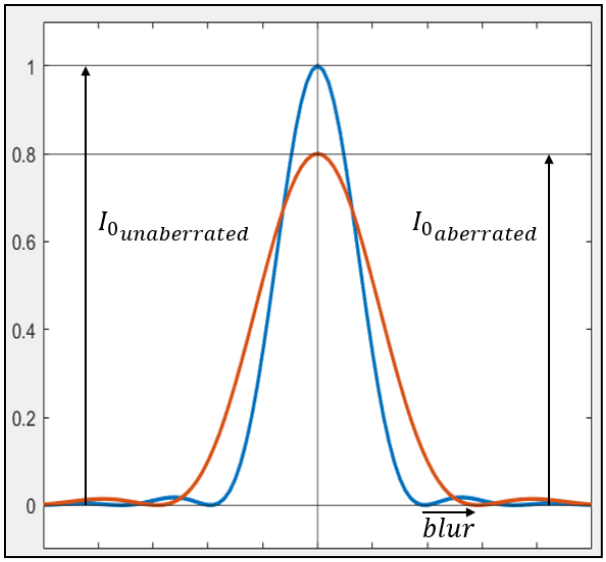

Figure 6 – The Strehl Ratio

Strehl ratio ranges from 0 to 1, and the closer it is to 1 the better the performance of the system. AO systems increase the Strehl ratio of aberrated systems by reshaping the incoming wavefront s to tighten (deblur) the focus spot toward its diffraction limited size. An AO system does this using three subsystems: a wavefront sensor, a processing computer, and a deformable mirror (DM). The wavefront sensor measures the shape of the incoming wavefronts[1,[8]], the processing computer calculates the mirror shape (the reconstructer) necessary to correct those wavefronts, and the DM deforms to match the calculated shape[9]. Upon reflection off the DM, wavefronts are no longer misshapen and come to a sharp focus to form an unblurred image (Figure 7).

[1] Commonly done so indirectly by measuring the wavefront's slopes rather than its direct phase. These measurements must then be reconstructed into the wavefront's phase (or shape) for use by the deformable mirror.

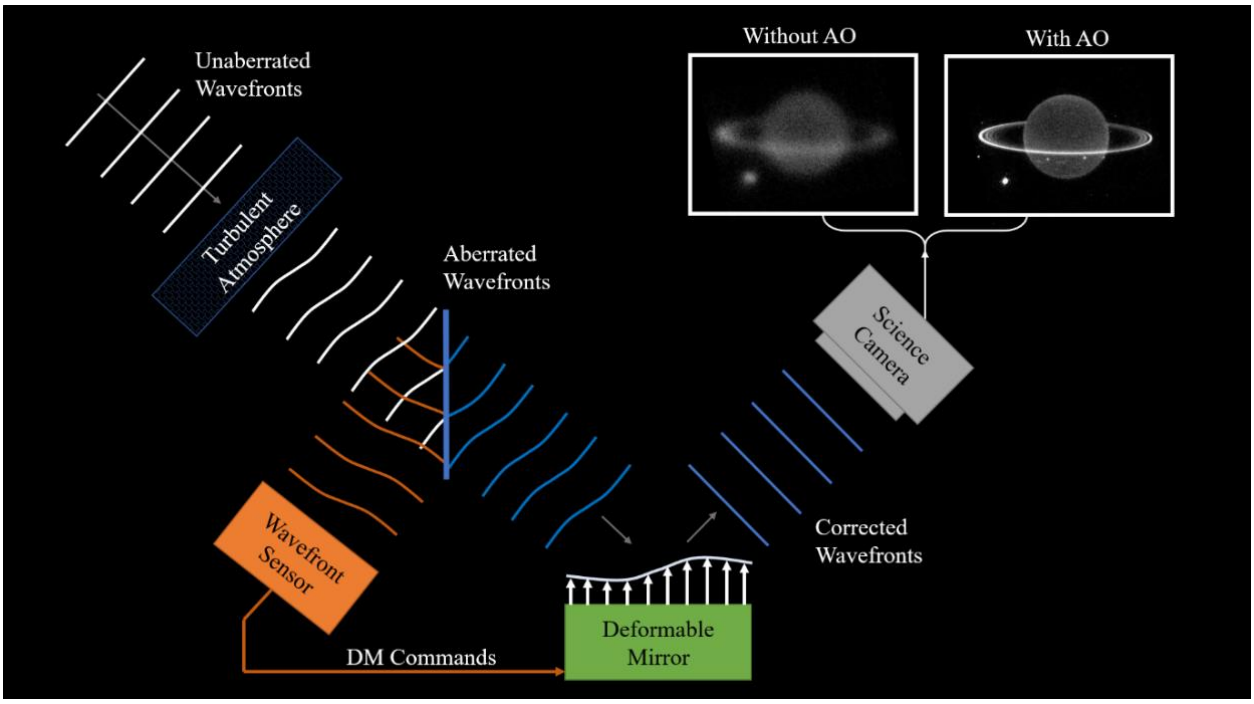

Figure 7 – A Simplified Diagram of an Open-Loop Adaptive Optics System

The Breakthrough Starshot AO system operates in reverse of a typical AO system used with a telescope, since it is projecting light rather than collecting it. Instead of receiving and correcting incoming aberrated wavefronts, the DM will 'pre-correct' the system's launch laser so that after transmitting through the atmosphere it will tightly focus on the nanocraft (Figure 8)[9].

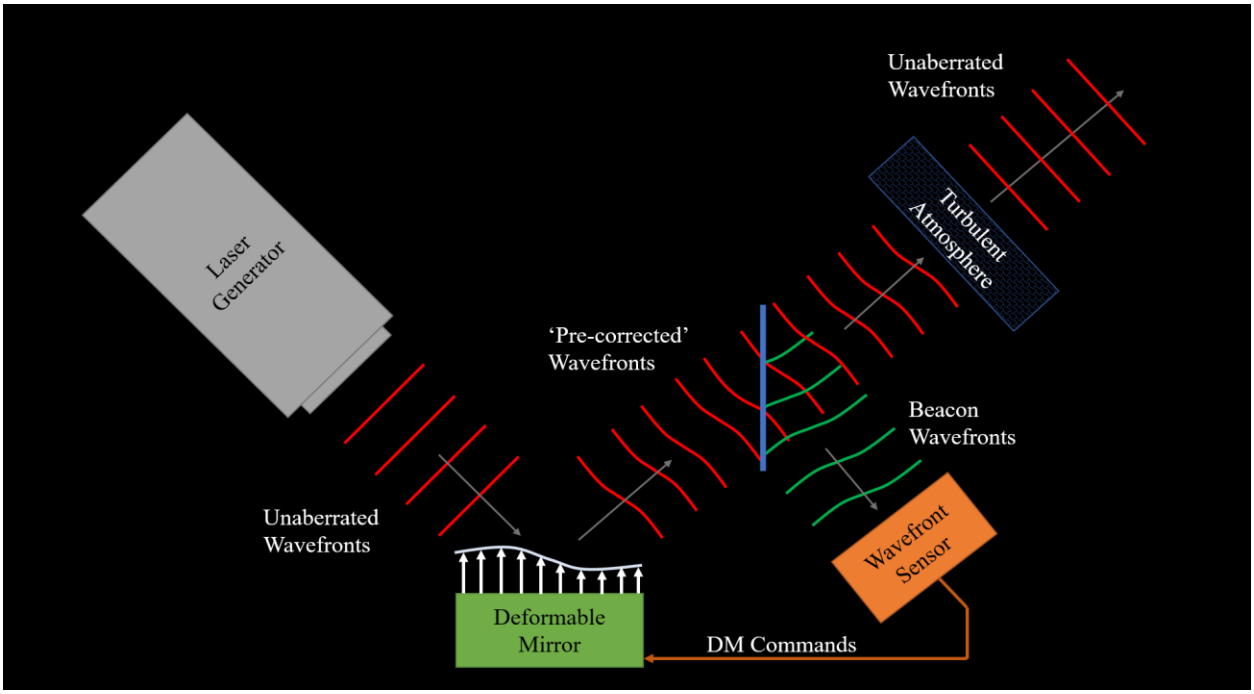

Figure 8 – A Simplified Diagram of the Breakthrough Starshot Adaptive Optics System

1.1.1 Wavefront Sensing and Correction

There are several types of wavefront sensors, and they are typically found following a beam splitter. A beam splitter samples a percentage of the entrance pupil's light. The percentages are precisely controlled with the used of specialized coatings, and in AO systems, are usually designed to aim most of the light towards the imaging camera. However, most astronomical objects of interest are too dim to sacrifice any light to a wavefront sensor without losing sacrificing signal-to-noise ratio on the science camera. This is often solved with the use of an Artificial Guide Star (AGS). Artificial Guide Star systems remove the need to use real stars for wavefront sensing by placing bright artificial stars or beacons in the sky with powerful lasers (Figure 9). One common type of AGS are high powered sodium laser guide stars (LGS) which are projected to the atmosphere's sodium layer (a dense 10km thick layer of atomic sodium about 90km in altitude)[10]. These sodium atoms resonate with the laser light and scatter it back towards the telescope. During this light's return flight, its wavefront experiences the same turbulent atmosphere that the astronomical object's light does and is thus distorted in the same way. This return laser light is collected alongside the signal and is separated with a dichroic (a color specific beamsplitter) to be sent to the wavefront sensor. This technique allows the LGS light to be used for wavefront sensing while preserving all the of signal for the science camera. There are many considerations in the design of an LGS wavefront sensing sub-system, but the two big concerns that relate to the Breakthrough Starshot program are laser beacon color (or *wavelength*) and its path through the atmosphere. Wavelength must be chosen such that it can both interact with the atmosphere and be differentiable from the outgoing propulsion beam, and an LGS's path-of-travel though the atmosphere must be as similar to the outgoing beam as possible. The challenges of these design choices are presented below.

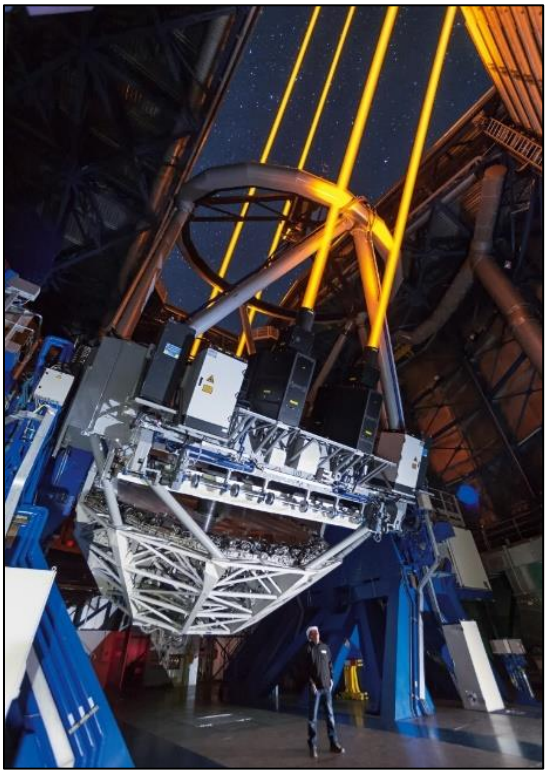

Figure 9 – Four Sodium Laser Guides Stars in use on Paranal Observatory's UT4 of the VLT[11]

A LGS is necessary to perform the adaptive correction for the launch of the nanocrafts using the laser projector. For the majority of the 10 minute launch period, the nanocraft itself can be used as the LGS beacon (Figure 10). Photons from the launch laser will strike the accelerating nanocraft and reflect back towards the projector. This return can serve as the wavefront sensor's beacon. As the nanocraft is accelerated it will be traveling at high speeds, causing the light reflected by the nanocraft to be Doppler shifted to a different color (or wavelength). This wavelength shift allows the light reflecting off the nanocraft to be differentiated from the atmospheric backscatter of the main laser. However, the Doppler shift will not become appreciable until the nanocraft has accelerated to about 1% of the speed of light. Given that the nanocraft is 1g and the laser imparts an average 100 N force, the nanocraft will not achieve 1% c until after 30 seconds of acceleration. Therefore, for the first 30 seconds of acceleration, a different LGS system will be needed.

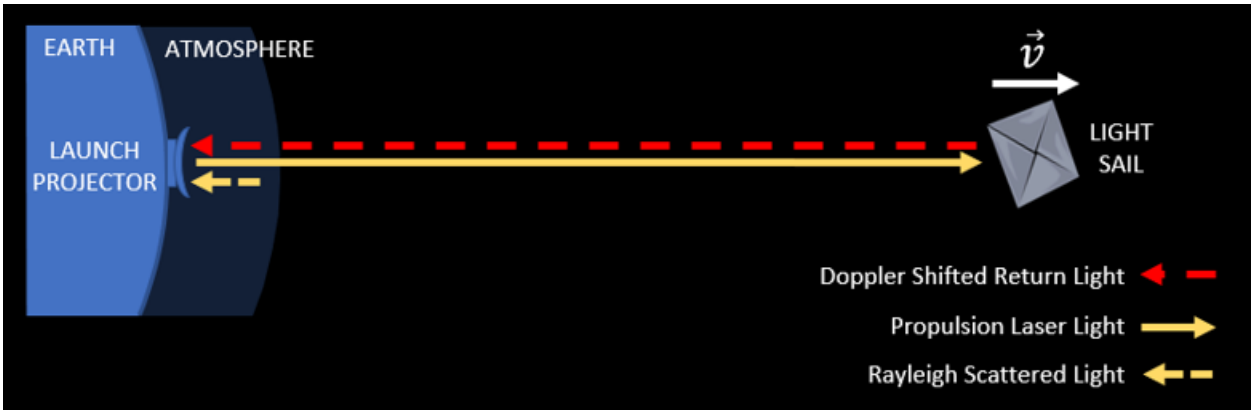

Figure 10 – Starshot's LGS Method for t > 30s

A satellite-based laser guide star (SLGS) (Figure 11)[3] is a proposed solution for the initial 30 s acceleration. The SLGS can be integrated into the "mothercraft," which is a larger satellite that would house the nanocraft for release into orbit at the moment of launch. As the launch projector activates and begins accelerating the nanocraft away, the mothercraft emits a beacon of a different color to be used for wavefront sensing. This satellite beacon picks up the same atmospheric distortion seen by the projection laser and is split off from the return light with a dichroic to be used for wavefront sensing, thus creating a suitable guide start for the first 30s of launch.

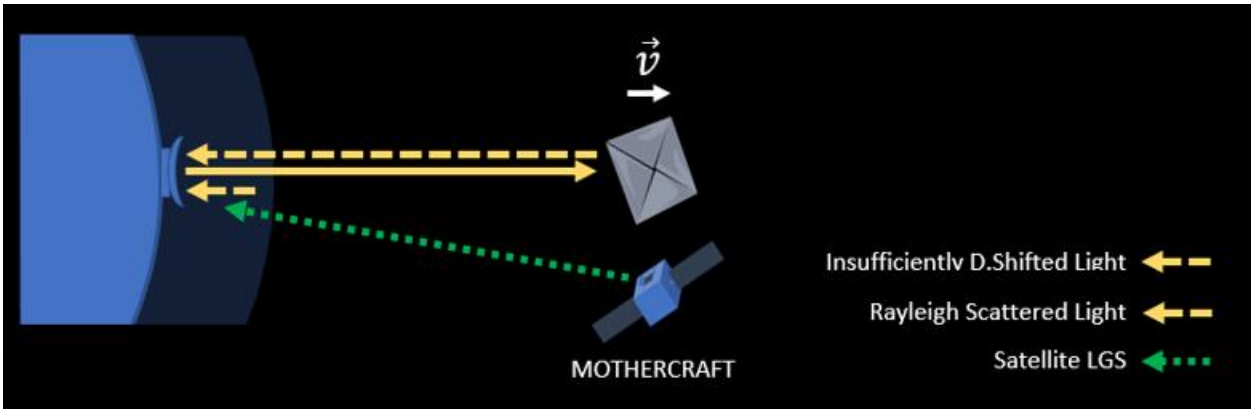

Figure 11 – Starshot's LGS Method for t < 30s

However, this method introduces a new potential issue. For an LGS to be useful to the Starshot system, its beam must travel through the *same* portion of the atmosphere as the projection laser will travel through. If the LGS travels through a different volume of turbulent atmosphere, it will not pick up the same distortions that the projected laser will see. In this scenario, the wavefront sensor measures irrelevant distortions making the DM's pre-corrections ineffective. A SLGS would become displaced in the sky from the direction of the nanocraft as it progresses in its orbit. As time passes, this separation could become large enough that the portion of atmosphere the LGS beacon travels through is very different from the portion of atmosphere that the launch laser has to travel through[12].

It is conceivable a certain orbital configuration could be established to keep the lateral motion of the mothercraft small enough that its angular separation from the nanocraft grows slowly and remains below a specified limit during the 30 second window. To determine if such an orbital configuration exists, a parameterizable orbital dynamics simulation was created to track the 3D positions of the nanocraft, mothercraft, and launch projector as functions of time during this 30 second launch period. This model was then used to locate the mothercraft's optimal orbital parameters and analyze their effects on AO correction.

1.1.2 Effects of Residual Error

Although the function of an AO system is to remove distortions from ideal wavefronts, there is always some residual error in a wavefront following correction. There are several sources of error which contribute to these correction imperfections, two of which are spatial and temporal mismatch between the DM and the wavefront error. Spatial mismatch occurs when an imperfect shape is applied to the DM either because the wavefront sensor did not measure the aberrated wavefront perfectly[2] or because the DM has only a finite number of actuators which it can use to deform[13]. The number of actuators on a DM of a given size defines the maximum spatial frequency it is able to correct, and any spatial frequencies in the wavefront beyond the limit of the DM are not corrected. Temporal mis-match arises when the correction being applied to the DM is applied too late or too infrequently[13]. How often a DM has to change shape is determined by how turbulent the atmosphere is. The frequency at which the atmosphere changes enough that a given measurement and correction become obsolete is known as the Greenwood Frequency (f_G). The length of one of these cycles is a function of wavelength, zenith view angle, and atmospheric turbulence and wind velocity profiles. Most AO systems operate around 10 times faster than f_G.[14]

Another major source of error results from having a beacon LGS travel through a different portion of the atmosphere than your reconstruction light will pass through. For all AO systems that use LGS, there is always some amount of angular and altitude difference between the beacon source and the object of interest[12]. The angular difference comes from an intentional displacement so as not to cover the object of interest with the beacon. The altitude difference, traditionally, comes from the finite height of the sodium layer[15].

[2] Or could not measure a given aberration such as tip/tilt for traditional LGS systems, or waffle distortion for Shack-Hartmann wavefront sensors.

For most applications, these residual errors can be engineered to be small enough that the correction is still good for capturing sufficiently resolved images. However, because of the unique wavefront sensing and correction configuration of the Breakthrough Starshot system (i.e. the use of an SLGS), the effects of these residual errors must be reassessed. For Starshot, residual error can lead to improper beam aiming/focusing which would lead the sail to fly out of the beam. Determining the effects of these residual errors will be necessary to identify how much the system can tolerate them, and therefore, how the system must be engineered.

Because the nanocraft will be propelled by the force of light at the projector's focus, it is necessary that this focus spot be stable and uniform throughout launch. Any residual irregularities in the irradiance distribution of the focus spot will result in irregularities in force distribution on the sail. Such force irregularities could lead the nanocraft to redirect away from Proxima or out of the propulsion beam entirely. In addition to irradiance irregularities, aiming irregularities can lead the nanocraft to fall out of the beam. In traditional astronomical AO systems, object of interests must be well tracked and centered on the science camera. Proper tracking involves both precisely pointing the telescope to counteract the rotation of the Earth and adaptively removing the random jitter of the object of interest caused by the atmosphere. In wavefront error terms, this jitter error is caused by fluctuations to the overall tip and tilt in the wavefront from the one that is perfectly perpendicular to the optical axis. For perfect line-of-sight transmission from projector to nanocraft (perfect aiming) tip and tilt must be zero. However, like residual shape irregularities, there is always some residual tip/tilt in a corrected beam. This residual aiming error leads to the beam not focusing perfectly on the center of the light sail or missing the sail entirely. A model to study the effects of this residual error on flight stability was developed and analyzed to identify the effects of residual tip/tilt errors on the flight stability of the nanocraft throughout launch.

Overall, there are many problems which must be addressed in order for the Breakthrough Starshot mission to become a success. In this thesis, two of those problems are addressed in detail. The first problem is what type of laser guide star will be used for the AO system. This problem is addressed by determining the orbital conditions which make a novel satellite based LGS system viable. The second problem is determining what correction performance the AO system will need to operate at for the lightsail to remain in stable flight within the laser beam throughout the 10 minute launch. This was accomplished by developing a flight stability model and determining how different correction performances affected the statistical likelihood of mission success. The answer to these two problems will allow the project to progress towards lower level system analysis and design and its eventual goal of exploring other star systems.

2. ORBITAL MODELING

A possible wavefront sensing solution for the first 30 seconds of the Starshot launch involves using a mothercraft satellite as a laser guide star beacon. For such a beacon to be an effective guide star, its light must travel through the same distorted volume of atmosphere that the launch laser will travel through. Although it will be impossible for the satellite beacon to travel through the exact same volume of atmosphere, it must travel through a volume extremely close or similar to that of the launch laser. To understand how close is close enough, it is necessary to understand how these errors are classified and quantified.

There are two related errors associated with a satellite LGS. To remain within the tolerance of these errors, the mothercraft's orbital configuration must satisfy 2 primary criteria: 1) relative to the nanocraft, the mothercraft's angular separation in the sky from the perspective of the wavefront sensor must remain within a specified limit known as the isoplanatic angle (θ_0) and 2) the altitude of the beacon should be high enough that it adequately samples the same cone volume of atmosphere the projection beam will travel through. These two error sources are referred to as angular and focal anisoplanatism, respectively (Figure 12)[12][15].

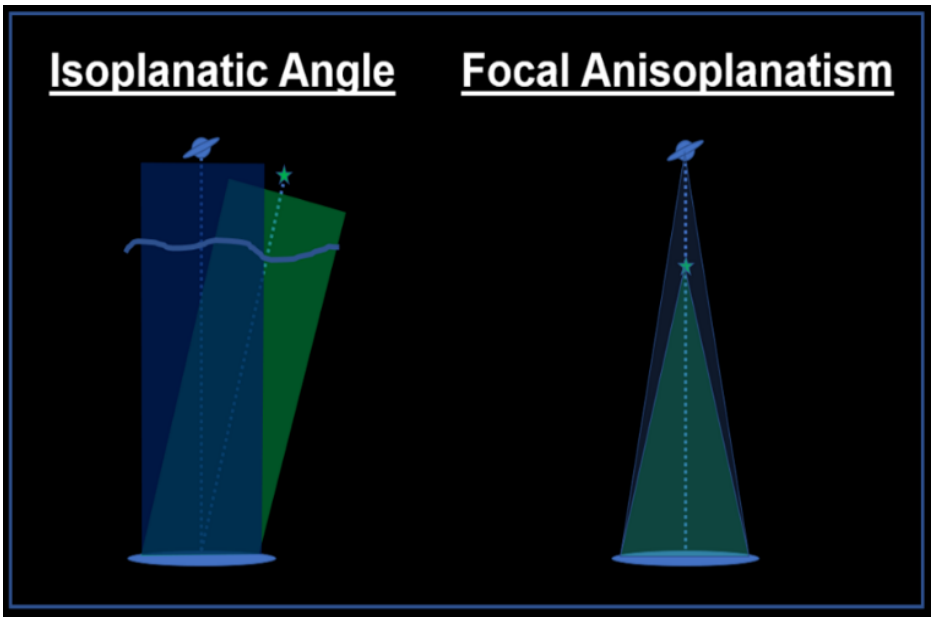

Figure 12 – Angular and Focal Anisoplanatism

Each of these sources of error depends on the magnitude of the atmosphere's turbulence and the relative positions of the beacon and object of interest in the sky from the perspective of the wavefront sensor (Figure 13).

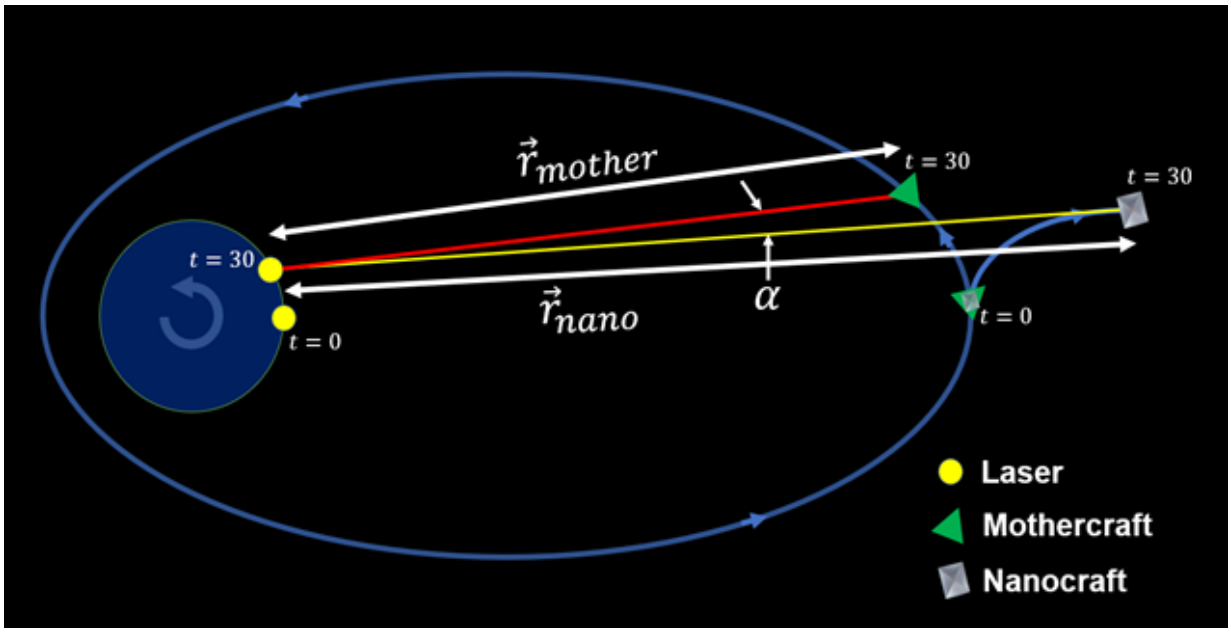

Figure 13 – Starshot Orbital Launch Geometry

Figure 13 shows the launch geometry. At the moment the mothercraft reaches its apogee (its highest point in orbit), the nanocraft will be released ($t = 0$). At this same time, the launch projector will be on Earth directly below apogee and will activate its beam. As the nanocraft accelerates away from Earth, the beam projector will constantly refocus its beam onto the sail. The mothercraft, still continuing in its orbit, will activate its beacon laser and aim it towards the launch projector, acting as the SLGS. As time progresses, each of these three points of interest will move in 3D space: the launch projector because of Earth's rotation, the mothercraft because of its continued orbital motion, and the nanocraft because of its acceleration away from the launch projector. At each moment in time between $t = 0$ and $t = 30s$, the angle between the mothercraft and nanocraft (α) will increase, and so will the difference in their altitude ($\Delta_{alt} = \vec{r}_{nano} - \vec{r}_{mother}$). These two terms, α and Δ_{alt} are used to determine the expected contribution of angular and focal anisoplanatic error to adaptive correction given a certain orbital configuration.

The magnitude of these two geometrical terms (and thus their contribution to correction error) varies depending on the parameters of a given orbit and the location of the launch projector on Earth. To identify how these terms are affected by orbital configurations, a fully parameterizable orbit simulation was developed. This model calculates and tracks the 3-dimensional positions of the mothercraft, nanocraft, and launch projector over time. Before a computer simulation was created, the parameterization of orbits had to be described.

2.1 Orbital Parameterization

When two orbiting bodies are viewed from an inertial frame of references, they each trace out distinctly elliptical trajectories whose foci are both located at a common center of mass (assuming the absence of any additional external forces on each body). If one of the two orbital bodies has a mass significantly greater than the other, it can be viewed as the inertial reference frame, with the smaller body tracing an elliptical trajectory whose focus is the center of the larger body. Since Earth's mass is on the order of $6x10^{24}kg$ and satellites are around $3x10^{3}kg$, this simplification can be assumed[16].

Johannes Kepler's Laws of Planetary Motion are used to describe the shape of this elliptical trajectory, its orientation relative to Earth's center, and the satellites motion along this trajectory. The smaller body in motion will be referred to as the secondary body, and the reference body will be referred to as the primary body. Kepler's Planetary Motion are comprised of 3 laws[16]:

1) The secondary body orbits in an ellipse with a foci at the system's center of mass, or barycenter[3].
2) A line segment connecting the two bodies sweeps out equal areas during equal intervals of time.
3) The square of the orbital period is proportional to the cube of the ellipse's semi-major axis.

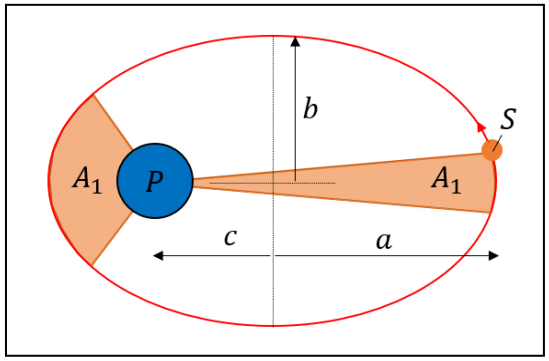

Figure 14 – A Keplerian Orbit

Figure 14 is an illustration of an orbit following Kepler's laws. First, Law 1 is illustrated by the elliptical orbit with its left focus (c) at the center of the primary body (*P*) and its semi-major and semi-minor axes (*a* and *b* respectively). Second, Law 2 is illustrated in the swept areas A_1 by the secondary object (*S*). These areas are swept by the secondary object in the same amount of time. The effect of this law is that the secondary object orbits much slower the further it is away from the primary object. Finally, Law 3, although not illustrated, relates the time it takes the secondary object to complete one full orbit (its orbital period, T_{orbit}) to the orbit's size (or semi-major axis: *a*). Law 3 gives the relationship between semi-major axis and orbital period (Equation 2)[16].

$$\boldsymbol{T_{orbit} = 2\pi\sqrt{\frac{a^3}{GM}}} \tag{2}$$

Where G is the gravitational constant and M is the mass of the primary body.

[3] Given the approximation that $m_{primary} \gg m_{secondary}$, the barycenter is located at primary's center of mass.

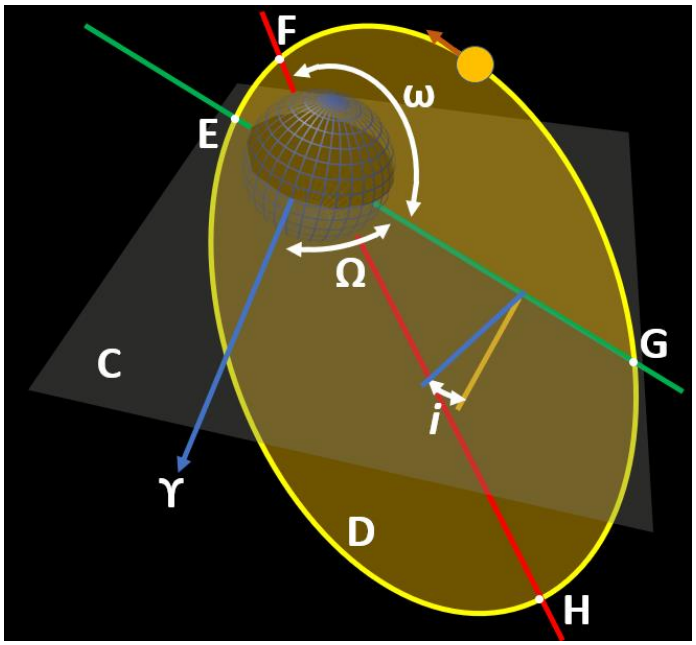

Figure 15 – Keplerian Orbital Parameters

There are several parameters used to describe how Keplerian orbits are oriented relative to Earth's axis (Figure 15). A secondary body (yellow) orbits a primary body (blue). The orientation of this orbital plane (D) is referenced from the primary body's equatorial plane (C) and Vernal point (γ). The equatorial plane is the plane along the primary's body equator, or normal to its axis of rotation. The Vernal direction for Earth is defined as the intersection point of Earth's equatorial plane and its ecliptic plane. Earth's ecliptic plane is the plane of its orbit around the sun. At the moment of the Vernal equinox around March 21 each year, the sun transitions from one side of Earth's equatorial plane to the other. In other words, the sun lies on the line of intersection – the Vernal point - of these two planes[17].

With the orbital reference points defined, several other parameters can be used to describe an orbit's orientation. Along the trajectory of the elliptical orbit, the points closest and farthest from the primary body are referred to as the orbit's Perigee (F) and Apogee (H), respectively. The red line that connects these two points is known as the "Apsides line". Orbital inclination (i) is defined as the angle between the orbital and equatorial planes about their line of intersection, and it ranges from 0° to 180°. Inclinations between 0° and 90° are orbits whose body orbits with the primary body's rotation and are referred to as 'prograde orbits.´ Inclinations between 90° and 180° are orbits whose body orbits opposite to their primary body's rotation and are called 'retrograde orbits'. Those with $i = 90°$ are 'polar orbits.[18]' The intersection line of C and D, depicted in green, is referred to as the "Node line". The points of the orbit that intersect the Node line are referred to as the Ascending (G) and Descending (H) Nodes and the direction the secondary body orbits determines which node is which (e.g. is a secondary body transitions from the southern hemisphere to the northern hemisphere, it's referred to as the Ascending Node). The direction of this Node line (i.e. the orbital plane's rotational axis) is defined by the angle between the Ascending Node and the Vernal point. This angle is referred to as the Longitude of the Ascending Node (Ω). Lastly, the rotation of the orbit around its orbital plane is defined as the angle between Perigee and the Ascending Node. This angle is referred to as the Argument of Perigee (ω)[17].

The shape of these orbits, of course, are elliptical and are fully defined by two shape factors: Semi-major axis (a) and orbital eccentricity (ϵ). As mentioned above, semi-major axis is analogous to the orbit's *size*. Eccentricity is a description of the orbit's ellipticity, and ranges between 0 and 1. The closer ϵ is to 0, the more circular an orbit is, and the closer ϵ is to 1, the more elliptical it is. Eccentricity is defined as the ratio of the semi-minor axis (b) and the semi-major axis (a)[16].

2.2 Model Architecture

In order to determine if the nanocraft and its mothercraft satellite become too separated for a satellite laser guide star (SLGS) beacon to be viable, the mothercraft's orbital motion can be simulated mathematically with the above orbital formulation. The orbit of the mothercraft will determine the component of its velocity transverse to the line of sight following the release of the nanocraft and thus its angular separation versus time. There are two orbital characteristics desirable for the mothercraft which minimize this separation over time: 1) a large semi-major axis, and 2) high orbital eccentricity. Because of Kepler's 2nd law, a large semi-major axis results in a longer orbital period which means the secondary body orbits with a lower average orbital angular velocity. Also, a high orbital eccentricity results in a high altitude apogee which, according to Kepler's 3rd law, leads to low instantaneous orbital angular velocities at apogee.

In order to determine which orbits yield an angular separation less than the isoplanatic angle θ_0, the position of the nanocraft over time must also be simulated. Because the nanocraft is being acted on by an external force (the propulsion force of the launch laser) it does not travel in an elliptical trajectory and its path cannot be determined analytically by Kepler's laws and equations. Because the motion of the nanocraft is too complex to be solved with analytical solutions, a numerical simulation will have to be created to solve for its motion. The positions of each craft obtained from their respective model can be used to determine their separation with time. The two names of these models are referred to as the 1) Keplerian Model (for the motion of the mothercraft), and 2) Dynamic Numerical Model (for the motion of the nanocraft).

2.2.1 Keplerian Model

A Keplerian Orbital Model was created in MATLAB (Figure 16) to model the position of the mothercraft in the sky. This modeling method was chosen because the mothercraft's motion is assumed to be free of external forces and because it is computationally easy.

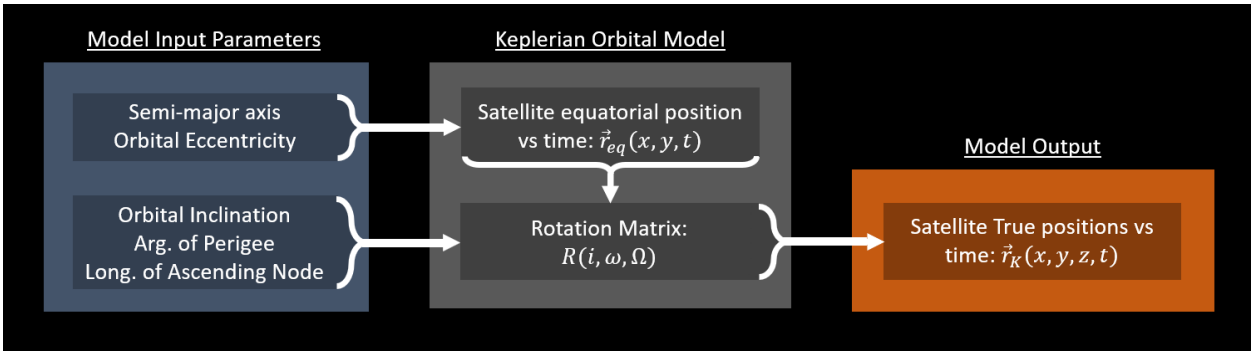

Figure 16 – Keplerian Orbital Model Block Diagram

The model is composed of two parts. The first part defines the positions of an orbital body within an elliptical orbit at any time ($\vec{r}_{eq}(x, y, t)$). This is done within the span of the Earth's equatorial plane (i.e. in the x-y plane, and not yet accounting for i, ω, or Ω) with the orbit's focus as the coordinate origin (i.e. Earth's center), the positive x-axis set as the Vernal point (γ), the z-axis set towards Earth's North pole, and $t = 0$ set to the time the body is at Perigee (referred to as the Pericenter Time)[19]. Once these positions are calculated in the equatorial plane, they are handed to the second part of the model which uses a rotation matrix ($R(i, \omega, \Omega)$) to orient the orbit to the defined i, ω, and Ω[20]. This output gives the position of the satellite in 3-dimensions at any time ($\vec{r}_K(x, y, z, t)$) as defined by the set of input orbital parameters (a, ϵ, i, ω, and Ω)[21].

To determine $\vec{r}_{eq}(x, y, t)$, the model uses Kepler's Equation (Equation 3). Kepler derived this equation to determine the position of an object in its orbit considering his second law:

$$\boldsymbol{M = E - \epsilon * \sin{(E)}} \quad \textbf{(3)}$$

In Kepler's Equation above, M is referred to as the Mean Anomaly and E is referred to as the Eccentric Anomaly. The Mean Anomaly is the fraction of an elliptical orbit's period that has elapsed since the orbiting body has passed through perigee. The Eccentric Anomaly is an angular term used to compute a body's position within its elliptical orbit. Eccentric Anomaly can also be used to determine the true angle swept by an object in its orbit since it passed perigee. This true angle is called the True Anomaly.

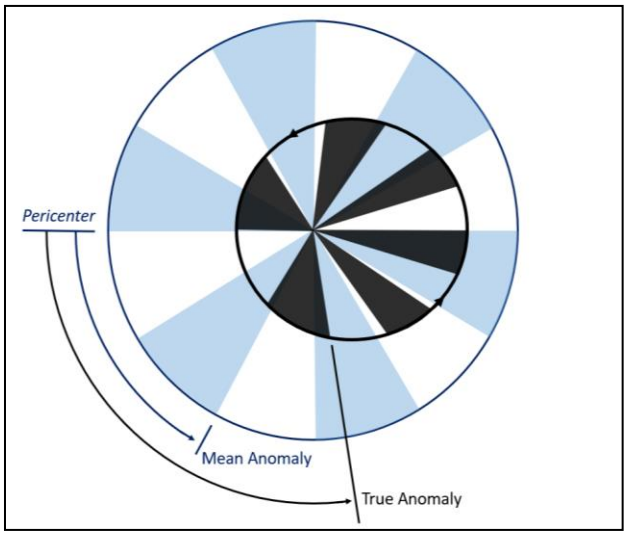

Figure 17 – Keplerian Angular Anomalies

Figure 17 illustrates how Mean Anomaly relates to the true angular position of a body in an elliptical orbit. The dark gray regions are areas that are swept out by a body in an elliptical orbit. The light blue regions are areas that are swept out by a body in an imaginary circular orbit with the same orbital period[4]. Both grey and blue areas are swept out in equal times. Mean Anomaly is defined as:

[4] For visual clarity, the circular orbit is drawn larger than its true scale relative to the elliptical orbit. For the scale to be true, the circular orbit would have to have a diameter equal to the elliptical orbit's semi-major axis. This would have led each orbit to intersect at two points, making the diagram visually messy.

$$\boldsymbol{M(t) = 2\pi/T_{orbit}(t - \tau)} \tag{4}$$

Where t is the elapsed time since Pericenter. The term τ is used to set $t = 0$ somewhere other than the Pericenter. In Figure 17 above, $\tau = 0$.

Because Kepler's Equation is a transcendental function, there is no closed-form solution for the Eccentric Anomaly (and therefore for the True Anomaly). Kepler solved this problem through a simple fixed-point iteration algorithm. A commonly used fixed-point iteration algorithm is called the Newton-Raphson Method[22].

With the Eccentric Anomalies computed for all Mean Anomalies, the True Anomalies (ν) are found using the follow equation:

$$\boldsymbol{\nu(t) = 2arctan\left(\sqrt{\frac{1+\epsilon}{1-\epsilon}}tan\left(\frac{E(t)}{2}\right)\right)} \tag{5}$$

Finally, the x-y position vector of a body in an elliptical orbit are given as:

$$\boldsymbol{\vec{r}_{eq}(x,y,t) = \begin{bmatrix} a*\left(1-\epsilon*cos\left(E(t)\right)\right)*cos\left(\nu(t)\right) \\ a*\left(1-\epsilon*cos\left(E(t)\right)\right)*sin\left(\nu(t)\right) \end{bmatrix}} \tag{6}$$

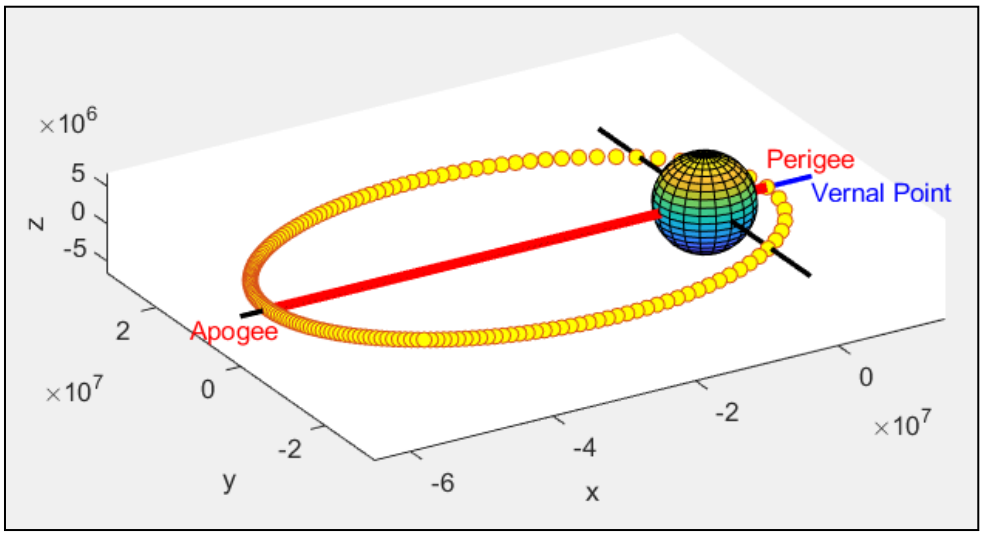

Figure 18 – An Illustration of an Equatorial Keplerian Orbit

Figure 18 illustrates a simulation output ($\vec{r}_{eq}(x, y, t)$) using Equation 3-6. The orbit shown has a semi-major axis that corresponds to an 18 hour long orbit, eccentricity $\epsilon = 0.75$, and $\omega = \Omega = i = 0$. The points drawn in the orbit's trajectory are spaced equal time frames apart. The low and high density of points around perigee and apogee, respectively, illustrate Kepler's 2nd law. It can also be seen that the location of perigee is referenced from the Vernal point.

With these position vectors solved within the equatorial plane of the primary body, the second part of the Keplerian model performs 3 matrix rotations. First, a z-axis rotation is performed to rotate the Node line by the Longitude of Ascending Node (Ω). The axis of this Node line is then stored. Second, another z-axis rotation is performed to set the appropriate angle between the Node and Apsides line, or the Argument of Perigee (ω). Finally, a rotation of the positions about the Node line introduces the appropriate orbital inclination (Equation 8)[21].

$$\vec{r}_K(x, y, z, t) = R(i, \omega, \Omega) * \vec{r}_{Eq}(x, y, t) \quad \textbf{(7)}$$

In the above equation, *R* is the rotation matrix combination of three individual rotation operations (Equation 8)[20].

$$R(i, \omega, \Omega) = R_{\hat{u}_N}(i) * R_z(\omega) * R_z(\Omega) \quad \textbf{(8)}$$

The right-most rotation sets the angle between the Node line and the Vernal point, the middle rotation sets the angle between the Apsides line and the Node line, and the left most rotation sets the orbital inclination by rotation about the Node line (denoted as a unit vector $\hat{u}_N$). The direction of the Node line can be found by rotating the Vernal point ($\hat{u}_V = \langle 1,0,0 \rangle$) with $R_z(\Omega)$.

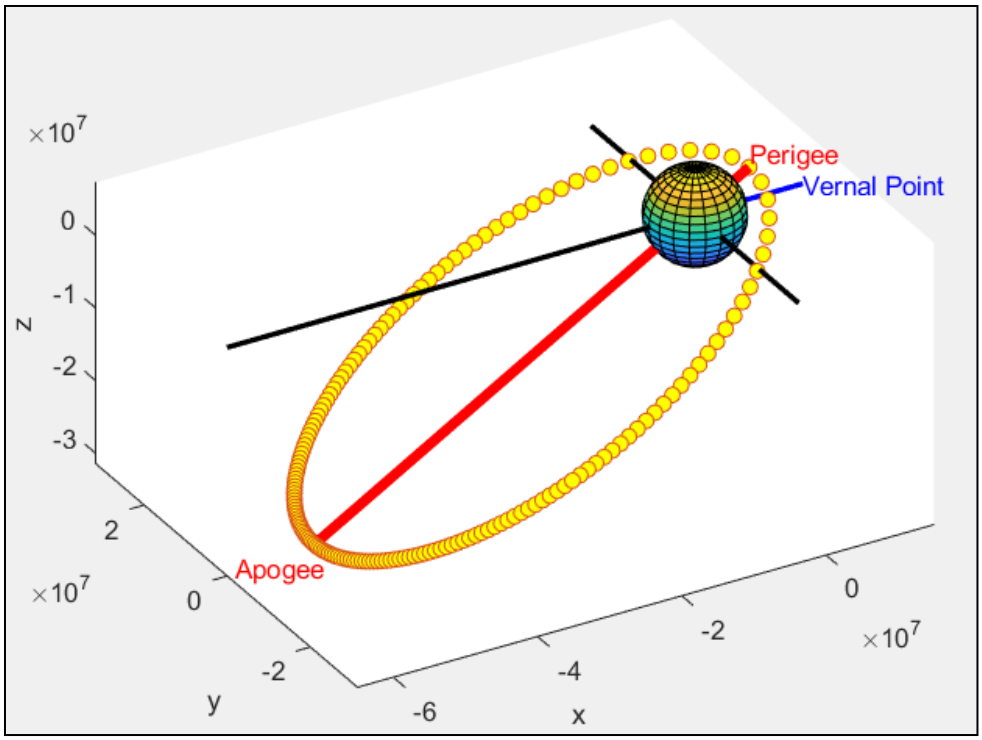

Figure 19 – An Illustration of the Keplerian Model Output

In Figure 19, the output of the Keplerian Model is shown. The orbital period and eccentricity is the same as in Figure 18, however, this diagram illustrates to inclusion of orbital inclination ($i = 30°$), Long. of Ascending Node ($\omega = 90°$), and the Argument of Perigee ($\Omega = 270°$).

With the above equations, definitions, and model, any orbit can be created, and a satellite's positions and velocities can be used to identify its performance as a SLGS.

2.2.2 Dynamic Numerical Model

For the nanocraft, another method for modeling its position in orbit is needed. This is because the nanocraft changes its orbit dynamically due to the applied force of the launch laser. This external force violates the assumptions required to use Kepler's equation. Additionally, the propulsion force and direction on the nanocraft changes with time and its resulting motion varies widely with different mothercraft orbital configurations. This complex system leads to nonlinear algebraic and differential equations that make it impossible to obtain a closed-form model of the nanocraft's motion. Dynamic Numerical Models (DNM) are a way of determining the behavior of a complex time-varying processes. Their basic operational principle is to approximate the dynamics of a system by integrating their derivatives over sufficiently small time steps[23][24].

The complex system which cannot be determined in closed-form is the time-varying position of the nanocraft. However, using a DNM, the nanocraft's position and velocity can be integrated step-by-step using each time interval's acceleration:

$$\boldsymbol{\Sigma\vec{F}(t) = \vec{F}_G\left(\vec{r}(t)\right) + \vec{F}_L\left(\vec{r}(t), \vec{r}_L(t)\right)} \quad \textbf{(9)}$$

$$\boldsymbol{\vec{a}(t) = \Sigma\vec{F}(t)/m} \quad \textbf{(10)}$$

$$\boldsymbol{\vec{v}(t + \delta t) = \vec{v}(t) + \vec{a}(t) * \delta t} \quad \textbf{(11)}$$

$$\boldsymbol{\vec{r}(t + \delta t) = \vec{r}(t) + \vec{v}(t) * \delta t} \quad \textbf{(12)}$$

The total force acting on the nanocraft is initially comprised of two forces: gravity ($\vec{F}_G$), and the force of the propulsion laser ($\vec{F}_L$). The gravitational force direction is determined by the nanocraft's position relative to Earth's center ($\vec{r}(t)$), and its magnitude is calculated using the classical Newtonian equation. The propulsion laser force direction is determined by the nanocraft's position ($\vec{r}(t)$) relative to the launch projector's position on Earth's surface ($\vec{r}_L(t)$). The force magnitude of the propulsion laser uses the formulation laid out by Parkin et al[25]. The following equations consider the beam power transfer efficiency of a Goubau type beam from the launch projector to the nanocraft's sail. The beam power transfer efficiency is affected by the diffraction limit of the launch projector's aperture, the relativistic doppler shift of the propulsion light, and atmospheric transmittance.

$$\boldsymbol{\tau(t) = \sqrt{8\lambda z(t)/D_s D_L}} \quad \textbf{(13)}$$

$$\boldsymbol{P_b(t) = \eta_a \eta_b(t) P_0} \quad \textbf{(14)}$$

$$\boldsymbol{\beta(t) = \frac{v(t)}{c}} \quad \textbf{(15)}$$

$$\boldsymbol{P_s'(t) = \frac{1-\beta(t)}{1+\beta(t)} P_b(t)} \quad \textbf{(16)}$$

$$\boldsymbol{F_L(t) = 2\frac{P_s'(t)}{c}} \quad \textbf{(17)}$$

P_0 is the power transmitted at the launch projector and P_b is the fraction of transmitted power that is able to reach the sail. The value of P_b is given by two transfer efficiency coefficients η_a and η_b. η_a is the fraction of power that is able to transmit through the atmosphere without being absorbed or scattered, and η_b describes the transfer efficiency caused by diffraction. Both terms range from 0 to 1. η_a is a function of wavelength, local site atmospheric properties, and transmission zenith angle, and for this simulation is assumed to be 1[5]. η_b, however, changes over the course of the launch and is implemented in the Dynamic Numerical model. It is a function of the dimensionless parameter τ which is given in Equation 13. Qualitatively, η_b is inversely proportional to τ, and their exact quantitative relationship is described in Parkin's paper[25]. The larger the launch projector's aperture is, and the larger the sail is to receive those photons, the higher the transfer efficiency. The farther the two are from each other, the lower the transfer efficiency. These two facts arise because the projector's beam has a finite beam divergence and, at large nanocraft distances, the propulsion beam spills beyond the edges of the sail[2]. The distance at which the projector's focus spot size becomes larger than the sail is:

$$\boldsymbol{L_0 = \frac{D_s D_L}{2\lambda\alpha}} \quad \textbf{(18)}$$

α is a term that depends on the shape of a launch projector and is equal to 1.22 for a circular aperture. Assuming sail diameters and a projector diameter of $D_s = 4m$ and $D_L = 4km$, and a projection wavelength of $\lambda = 1064nm$, the critical distance L_0 is approximately 6,000 megameters ($6 * 10^9\ m$). At this distance, the value of η_b begins to fall off from unity. However, for the initial 30 second acceleration period, the nanocraft will not have had enough time travel beyond this critical distance. The result is an η_b that is near unity through the use of the SLGS.

With both transfer efficiencies being fairly close to 1 during the 30 second period, the amount of power that makes it to the sail (P_b) is nearly the amount sent by the projector (P_0). The power felt by the sail, however, depends on its relativistic velocity (β). If the sail is moving at a high

[5] This is because over the 10 minute launch, the launch wavelength, local atmospheric absorption/scattering properties, and transmission zenith angle are not expected to change by amounts that would affect the value η_a. Additionally, propulsion wavelength is chosen to be extremely transmissive through Earth's atmosphere ($\lambda = 1064nm$).

relativistic speed (one comparable to the speed of light), it will experience a Doppler shift in the color of the incoming photons. Because the conservation of momentum between the sail and the reflected photons must be equal in the projector's frame of reference, there is an effective momentum transfer loss due to the nanocraft's velocity (Equation 16). For the first 30 seconds, this transfer loss is only about 2% at 0.01c, while at 10 minutes it is around 30% at 0.2c. Finally, Equation 17 relates the amount of power on the sail ($P_s{}'$) to the amount of force felt from reflection (F_L). This equation assumes a sail that is perfectly reflective. The force variation given a sail with some amount of absorption and transmission is also described by Parkin et al[25]. Given that the transfer losses from η_a, η_b, and β are small during the first 30 seconds, the propulsion force on the nanocraft at every time step is very near the ideal 100 N.

For Equation 9-11 to work, the position ($\vec{r}(t_0)$) and velocity ($\vec{v}(t_0)$) of the nanocraft at the moment of launch are needed. The initial launch position and velocity of the nanocraft can easily be found using the Keplerian Model derived for the mothercraft. Because the mothercraft will house and release the nanocraft in orbit at the time of launch, the nanocraft will share the same initial position and velocity as the mothercraft. However, as time progresses forward, all future positions, velocities, and accelerations for the nanocraft will be determined with Equation 9-11 above. Equation 9, however, requires knowledge of where the launch projector is on Earth's surface ($\vec{r}_L(t)$) at every time step.

The launch projector's positions over time (t) can be calculated with the following equation:

$$\vec{\boldsymbol{r}}_{\boldsymbol{L}}\left(\boldsymbol{\theta}_{\boldsymbol{lat}}, \boldsymbol{t}_{\boldsymbol{p}}, \boldsymbol{t}\right) = \left(\boldsymbol{R}_{\boldsymbol{e}} \cos \boldsymbol{\theta}_{\boldsymbol{lat}}\right) * \begin{bmatrix} \cos\left(\dfrac{2\pi}{\boldsymbol{T}_{\boldsymbol{day}}} * \left(\boldsymbol{t} + \boldsymbol{t}_{\boldsymbol{p}}\right)\right) \\ \sin\left(\dfrac{2\pi}{\boldsymbol{T}_{\boldsymbol{day}}} * \left(\boldsymbol{t} + \boldsymbol{t}_{\boldsymbol{p}}\right)\right) \\ \tan\left(\boldsymbol{\theta}_{\boldsymbol{lat}}\right) \end{bmatrix} \quad \textbf{(19)}$$

In Equation 19, θ_{lat} is the latitude line that the launch projector is built, R_e is the radius of the Earth, and T_{day} is the length of one Earth rotation (i.e. 24 hours). The time (t) is referenced from the moment the projector is under the vernal point. The parameter t_p can control the location of this reference position.

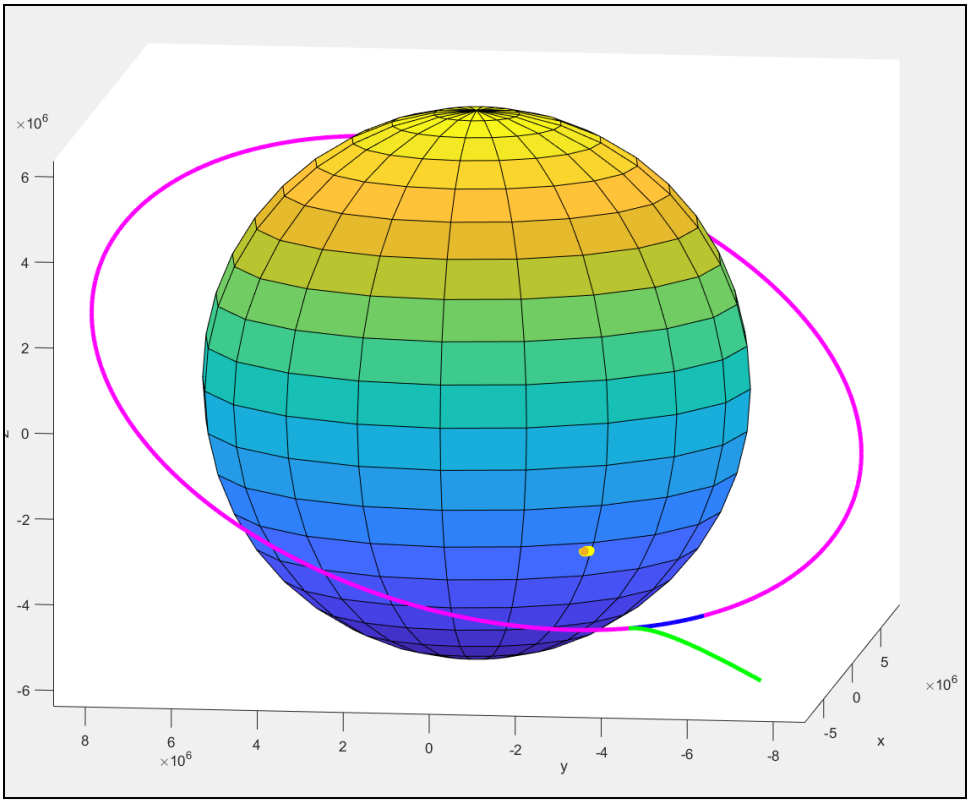

Figure 20 – An Illustration of the Dynamic Numerical Simulation Output

Figure 20 above illustrates how the Dynamic Numeric Model simulates the complex motions of the Starshot system over 30 seconds using Equation 9-19 above. The Earth is orbited by the mothercraft in a circular orbital trajectory (magenta). The yellow points on Earth demonstrate how the launch projector would move due to Earth's rotation. The blue and green lines show the paths the mothercraft and nanocraft, respectively, during a 30s period[6].

[6] NOTE: The propulsion force is drastically reduced in this illustration to show a slower departure of the nanocraft from its original orbit. The nanocraft's distance from Earth after 30 seconds with a full 100N of force would be too great to illustrate clearly relative to the launch projector.

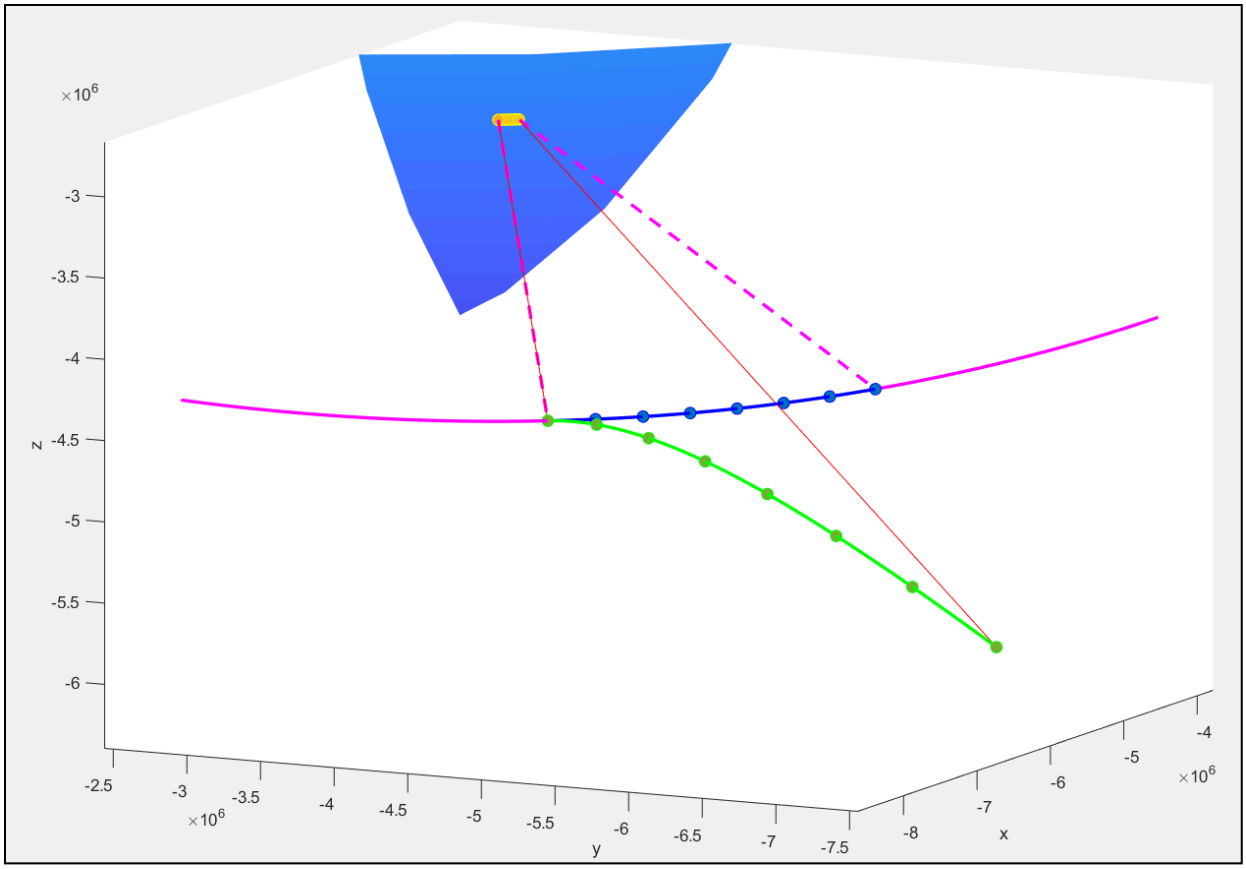

Figure 21 – A Close Up of the Dynamic Numerical Model Output

Figure 21 is a close up of Figure 20. It is also a simulation representation of the geometry posed earlier in Figure 13. Above, there are 8 points along each of the spacecraft's respective trajectory, spaced equally apart in time. Initially, the lines connecting the mothercraft and the nanocraft to the launch projector (dashed and solid, respectively) are coincident with each other. However, after 30 seconds, these lines separated from each other in angle. For this low period circular orbit, this angle is too large for adaptive correction to work but illustrates nicely the functionality of the simulation. Discussed later are the various orbital configurations used to study this angular separation.

Now, with the initial position of the nanocraft ($\vec{r}(t_0)$) and the positions of the launch projector easily parameterizable, the nanocraft's acceleration vector can be determined at each time-step (as illustrated in Figure 20 and 21). However, it is not as simple as the vector connecting the launch projector to the nanocraft at a given time *t*. This is because light has a finite speed (c) and it takes time for the propulsion beam to reach nanocraft's sail. If at a time t_1, the projector sends a beam of light towards the position of nanocraft at that same moment in time ($\vec{r}(t_1)$), by the time the beam reaches that location the nanocraft will have moved out of way. To account for this, the launch projector's aim must lead the nanocraft and anticipate where it will be by the time a given photon arrives. This is analogous to an American football quarterback throwing his ball ahead of his receiver. However, unlike the quarterback and receiver, the projector and lightsail will be constantly sending and receiving photons. Because this is being simulated numerically, this otherwise continuous stream of photons is being modeled as a discrete number of light "pulses"

leaving the projector every time step. These time steps are set to be small enough that the dynamic behavior is indistinguishable from a continuous stream. Each of these "pulses" not only have to lead where the nanocraft will be given that pulses time of flight, but it must also consider the non-linear motion of the sail caused by the pulses that were sent the few time steps ahead of it.

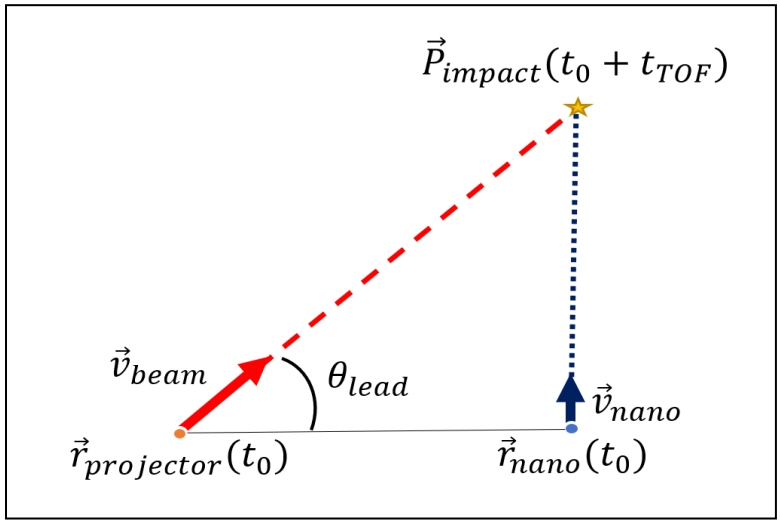

Figure 22 – Aim Leading

Given the initial positions of the launch projector ($\vec{r}_L(\theta_{lat}, t_p, t = 0) \rightarrow \vec{r}_{L,0}$) and the nanocraft ($\vec{r}(t = 0) \rightarrow \vec{r}_{nano,0}$), the initial velocity of the nanocraft ($\vec{v}(t = 0) \rightarrow \vec{v}_{nano,0}$), and the speed of light (c), the leading direction of the launch projector ($\hat{L}_L$) can be determined to assure the light impacts the nanocraft at an impact location ($\vec{P}_{impact}$). The time of flight (t_{TOF}) of a pulse between the laser projector and the location of impact is given as the distance required to travel divided by the speed of travel:

$$\boldsymbol{t_{TOF}} = \frac{\sqrt{\left(\vec{\boldsymbol{P}}_{\boldsymbol{impact,x}} - \vec{\boldsymbol{r}}_{\boldsymbol{,x}}\right)^2 + \left(\vec{\boldsymbol{P}}_{\boldsymbol{impact,y}} - \vec{\boldsymbol{r}}_{\boldsymbol{L,y}}\right)^2 + \left(\vec{\boldsymbol{P}}_{\boldsymbol{impact,z}} - \vec{\boldsymbol{r}}_{\boldsymbol{Laz,z}}\right)^2}}{\boldsymbol{c}} \quad \textbf{(20)}$$

In order for the impact to occur, the position of the nanocraft after an elapsed t_{TOF} must be equal to the position of impact:

$$\vec{\boldsymbol{r}}_{\boldsymbol{nano}} = \vec{\boldsymbol{P}}_{\boldsymbol{impact}} = \vec{\boldsymbol{r}}_{\boldsymbol{nano,0}} + \vec{\boldsymbol{v}}_{\boldsymbol{nano,0}}\boldsymbol{t_{TOF}} \quad \textbf{(21)}$$

Expressing Equation 21 above component by component yields:

$$\vec{\boldsymbol{P}}_{\boldsymbol{impact,x}} = \vec{\boldsymbol{r}}_{\boldsymbol{nano,0,x}} + \vec{\boldsymbol{v}}_{\boldsymbol{nano,0,x}}\boldsymbol{t_{TOF}} \quad \textbf{(22)}$$

$$\vec{\boldsymbol{P}}_{\boldsymbol{impact,y}} = \vec{\boldsymbol{r}}_{\boldsymbol{nano,0,y}} + \vec{\boldsymbol{v}}_{\boldsymbol{nano,0,y}}\boldsymbol{t_{TOF}} \quad \textbf{(23)}$$

$$\vec{\boldsymbol{P}}_{\boldsymbol{impact,z}} = \vec{\boldsymbol{r}}_{\boldsymbol{nano,0,z}} + \vec{\boldsymbol{v}}_{\boldsymbol{nano,0,z}}\boldsymbol{t_{TOF}} \quad \textbf{(24)}$$

Plugging Equation 22-24 into Equation 20, rearranging, and squaring both sides gives:

$$t^2c^2 = \left(\vec{r}_{nano,0,x} + \vec{v}_{nano,0,x}t_{TOF} - \vec{r}_{L,x}\right)^2 + \left(\vec{r}_{nano,0,y} + \vec{v}_{nano,0,y}t_{TOF} - \vec{r}_{L,y}\right)^2 + \left(\vec{r}_{nano,0,z} + \vec{v}_{nano,0,z}t_{TOF} - \vec{r}_{L,z}\right)^2 \quad (25)$$

Expanding and rearranging Equation 25 yields:

$$\left[\vec{v}^2_{nano,0,x} + \vec{v}^2_{nano,0,y} + \vec{v}^2_{nano,0,z} - c^2\right] * {t_{TOF}}^2 + [2\left(\vec{v}_{nano,0,x}(\vec{r}_{nano,0,x} - \vec{r}_{L,x}) + \vec{v}_{nano,0,y}(\vec{r}_{nano,0,y} - \vec{r}_{L,y}) + \vec{v}_{nano,0,z}(\vec{r}_{nano,0,z} - \vec{r}_{L,z})\right)] * t_{TOF} + \left[\left(\vec{r}_{nano,0,x} - \vec{r}_{L,x}\right)^2 + \left(\vec{r}_{nano,0,y} - \vec{r}_{L,y}\right)^2 + \left(\vec{r}_{nano,0,z} - \vec{r}_{L,z}\right)^2\right] = 0 \quad (26)$$

Equation 26 appears to be of the quadratic form: $Ax^2 + Bx + C = 0$, with:

$$A = \left|v_{nano,0}\right|^2 - c^2 \quad (27)$$

$$B = 2 * \left[v_{nano,0} \cdot \left(\vec{r}_{nano,0,} - \vec{r}_{L,0}\right)\right] \quad (28)$$

$$C = \left|\left(\vec{r}_{nano,0,} - \vec{r}_{L,0}\right)\right|^2 \quad (29)$$

The above three equations can be plugged into the quadratic equation to find time of flight necessary for coincident impact. If the discriminant of the quadratic equation is negative, then there is no real solution. Fortunately, this only occurs when the velocity of the target (the nanocraft) is faster than the velocity of the projectile (light), which is impossible for our system. For our system, the solution will include both positive and negative solutions for time of flights. The physical solution is taken as the positive one. This solution can then be plugged back into Equation 22-24 to find $\vec{P}_{impact}$. The leading direction, $\hat{L}_L$, can be found with the following equation:

$$\hat{L}_{L,0} = \left(\vec{P}_{impact} - \vec{r}_{L,0}\right)/\left|\vec{P}_{impact} - \vec{r}_{L,0}\right| \quad (30)$$

This leading direction is then used to determine the direction of the force the laser beam imparts onto the nanocraft.

However, Equation 30 is only useful for the very first point in the numerical model. This is because the nanocraft is traveling in a straight line[7] before the initial pulse impact. This un-hindered straight path is what makes Equation 21 valid. Unfortunately, future leading directions, say $\hat{L}_{L,i}$, will have to account for the trajectory manipulations caused by those pulses sent just before it. In order to determine $\hat{L}_{L,i}$, where *i* is some interval index within the numerical analysis, one must know how the force of the beam from $\hat{L}_{L,i-1}$ affected $\vec{r}_{nano,i-1}$, and $\vec{v}_{nano,i-1}$; however, because the time length of the numerical interval ($\delta t \approx 1ms$) is much shorter than any expected time of flight ($t_{TOF,i} > 1s$) the photons sent from $\hat{L}_{L,i}$ will have to have been traveling for ($t_{TOF,i} - \delta t$) before the time the nanocraft reaches $\vec{P}_{impact,i-1}$ (or the point used to calculated $\hat{L}_{L,i}$ in the first place). The question then becomes: How can $\hat{L}_{L,i}$ be determined if its pulse must be launched *before* the nanocraft is impacted and redirected at $\vec{P}_{impact,i-1}$? What can $\hat{L}_{L,i}$ use for Equation 30 in lieu of $\vec{P}_{impact,i-1}$?

[7] Rather, in an ostensibly straight line. The initial flight times are under 1 second, and the curvature of the traversed trajectory of a satellite over 1 second is negligible.

The solution is to take the position of the nanocraft at a given interval ($\vec{r}_{nano,i}$) and use its velocity at that same time interval ($\vec{v}_{nano,i}$) to determine where it would have been ($t_{TOF,i} - \delta t$) seconds ago. This dummy position, call it $\vec{r}'_{nano,i}$, and the unaltered $\vec{v}_{nano,i}$ can then be used as the 'initial position and velocity' for each interval calculation of $\hat{L}_{L,i}$. With this trick, each interval now has a 'dummy' nanocraft position and velocity which travel in un-hindered straight lines during an interval's $t_{TOF,i}$, Equation 21 becomes valid for all numerical intervals, i.

With the implementation of aim leading in the Dynamic Numerical Model and the positions of the launch projector calculated, the complex motion of the nanocraft in response to a given orbit defined in the Keplerian Model can be simulated.

2.3 System Performance Characterization

With the 3-dimensional positions of the mothercraft, nanocraft, and laser projector established, the anisoplanatic contributions to the wavefront correction error can be calculated to characterize the expected performance of the AO system's pre-correction. To determine the mean squared wavefront phase aberration (or error) attributed to angular anisoplanatism, the following equation is used[12][14]:

$$\boldsymbol{\sigma_{iso}^2 = \left(\frac{\alpha}{\theta_0}\right)^{5/3}} \tag{31}$$

where α is the angular separation in the sky between the mothercraft and nanocraft, and θ_0 is the isoplanatic angle. When the angle between the mothercraft yields $\sigma_{iso}^2 = 1.0\ [rad^2]$, that angular separation is called the isoplanatic angle. It is a function of wavelength, atmospheric turbulence profile, and viewing zenith angle. The value of the isoplanatic angle can be approximated using the Hufnagel-Valley (H-V) Turbulence Model. For our system and wavelength, the isoplanatic angle is approximately $\theta_0 = 20\mu rad$[14]. α can be determined at each time step in the simulation by using the unit vectors that point from the launch projector to both the mothercraft and nanocraft ($\hat{r}_m$ & $\hat{r}_n$ respectively). Using the definition of a dot product, the angular separation is found as:

$$\boldsymbol{\alpha(t) = \mathbf{acos}(\hat{r}_m(t) \cdot \hat{r}_n(t))} \tag{32}$$

The next performance source of error is focal anisoplanatism. Classically, the following equation for its mean squared phase aberration is used[14][15]:

$$\boldsymbol{\sigma_{FA}^2 = \left(\frac{D_L}{d_0}\right)^{\frac{5}{3}}} \tag{33}$$

where D_L is the aperture diameter of the launch projector (2 km), d_0 is a characteristic length scale determined, by wavelength, atmospheric turbulence profile, and the beacon's altitude. However, because this equation is often used to correct an astronomical object, it assumes this object is at infinity, and thus, a correction volume that is a cylinder. For the Breakthrough Starshot, however, the beacon (the mothercraft) and the object of interest (the nanocraft) begin at the same altitude thus share the same cone of atmosphere from the perspective of the launch projector (Figure 23).

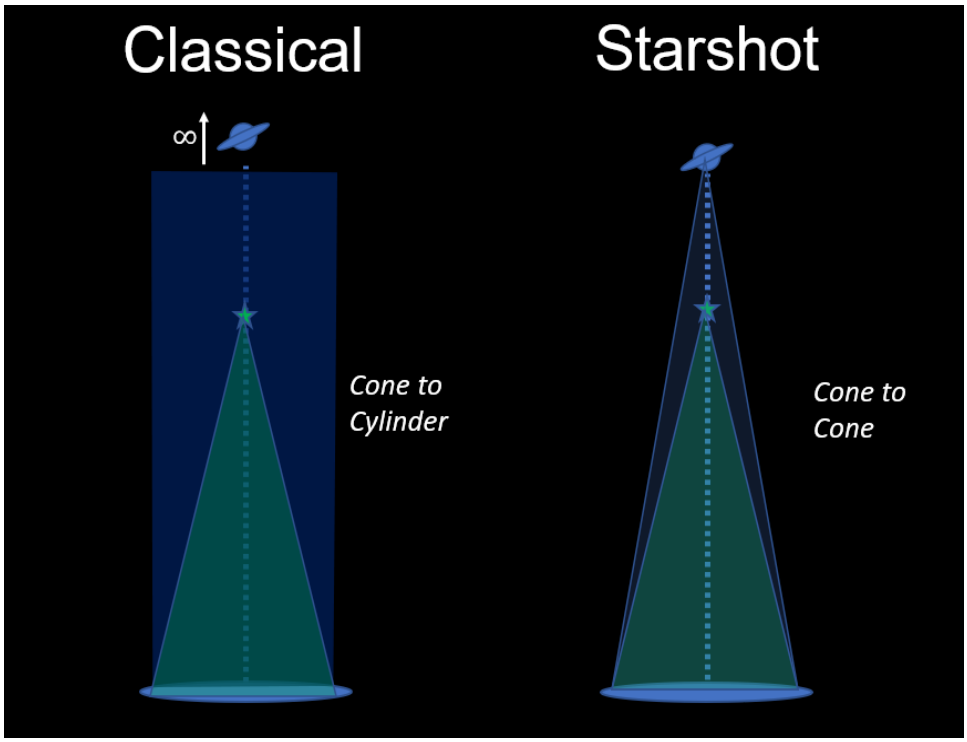

Figure 23 – Classical vs Starshot Focal Anisoplanatism

The effect of the beacon and object of interest initially having the same altitude is that there is no focal anisoplanatic error. As the launch projector begins propelling the nanocraft out of our solar system, focal anisoplanatism increases because the cone of the nanocraft becomes taller than the cone of the mothercraft's beacon. To account for this, a correction factor is added to the classical formula:

$$\boldsymbol{\sigma_{FA}^2 = \left(\frac{D_L}{d_0}\right)^{\frac{5}{3}} \left(1 - \frac{|\vec{r}_{mother}|}{|\vec{r}_{nano}|}\right)^{\frac{5}{3}}} \quad \textbf{(34)}$$

Where $|\vec{r}_{mother}|$ & $|\vec{r}_{nano}|$ are the distances (or altitudes) to the mothercraft and nanocraft [in km]. This correction factor respects two important boundary conditions for the Starshot system: 1) $\sigma_{FA}^2 = 0$ when the nanocraft and mothercraft are coincident in space, thus no focal anisoplanatism, and 2) $\sigma_{FA}^2 = \left(\frac{D_L}{d_0}\right)^{5/3}$ when the nanocraft approaches infinity, in which the cone of the object of interest becomes so tall that it is ostensibly a cylinder. The power of 5/3 is used to keep the appropriate scaling in relation to the atmospheric turbulence. Lastly, d_0 is assumed to also vary as the mothercraft's altitude changes, and like θ_0, can be approximated conservatively with the Hufnagel-Valley model[14]:

$$\boldsymbol{d_0 = 0.018|\vec{r}_{mother}| + 0.39\ [m]} \quad \textbf{(35)}$$

with the equation input, $|\vec{r}_{mother}|$, expressed in units of km.

2.4 Parameter Optimization

With the completed model for determining the viability of a given orbit for wavefront sensing, an optimizer was created that looped through a series of potential orbits to find those which yielded values $\alpha < \theta_0$ throughout the 30 s. To do this efficiently, a parameter space must be defined for analysis. This means defining as many fixed parameters possible so as to reduce the number of orbits to be studied. The processing time thus is drastically reduced by limiting the number of degrees of freedom the optimizer has to run through.

First, the mothercraft's orbit's longitude of ascending node, and argument of perigee (Ω, & ω) are pre-defined by where in the celestial sphere Proxima will be 20 years from launch[8]. This is because the final trajectory of the nanocraft is approximately the line connecting the launch projector and the nanocraft at the moment of launch. At that moment of launch, it is assumed that the nanocraft will be released at apogee and the launch projector will be directly below[9] it. This means that ω and Ω must be set so that the apogee of the orbit, is in line with both the launch projector and Proxima's point in the sky. The celestial coordinates of a star in the sky are defined by its Right Ascension (RA) and Declination (Dec). RA is the angle from the Vernal Point a star is around the celestial sphere, and Dec is the angle above or below the equatorial plane a star is on the celestial sphere. Proxima's celestial coordinates are $RA_{Prox.} = 14h\ 29m\ 43.84s$ and $Dec_{Prox.} = -62°\ 40'\ 48.36''$[26],[10]. To manipulate an orbit's apogee and major-axis line into this direction, the following Longitude of Ascending Node and Argument of Perigee were used:

$$\textbf{Longitude of Ascending Node:} \quad \boldsymbol{\Omega = RA_{Prox.} + 90° \approx 210°}$$

$$\textbf{Argument of Perigee:} \quad \boldsymbol{\omega = 90°}$$

Ω and ω only define two of the three rotational degrees of freedom necessary to send the nanocraft to Proxima. This third degree of freedom, the mothercraft's orbital inclination (i), is defined by what latitude the launch projector is on Earth. This is because the line connecting the projector to the orbit's apogee must make an angle with the equatorial plane equal to Proxima's Declination. Because of its Southernly latitude, its vastly open areas, its calm airs, and its high elevation, the Atacama Desert has been suggested for the location of the launch projector[27]. The Atacama Desert ranges in Earthly latitude between -18 and -30 degrees. For every latitude within the Atacama Plateau, there exists an orbital inclination which satisfies a trajectory angle that equals Proxima's Declination (Figure 24).

[8] Not only will the projector's aim have to lead the nanocraft's motion in orbit, but the nanocraft's trajectory has to lead Proxima's motion through the Milky Way.

[9] "Directly below" here means within the plane that spans the orbit's Apsides and Earth's poles.

[10] These coordinated represent the apparent position of Proxima in the Sky 20 years (the travel time of the nanocraft) after 50 years from now (the approximate project timeline for the Starshot program to launch).

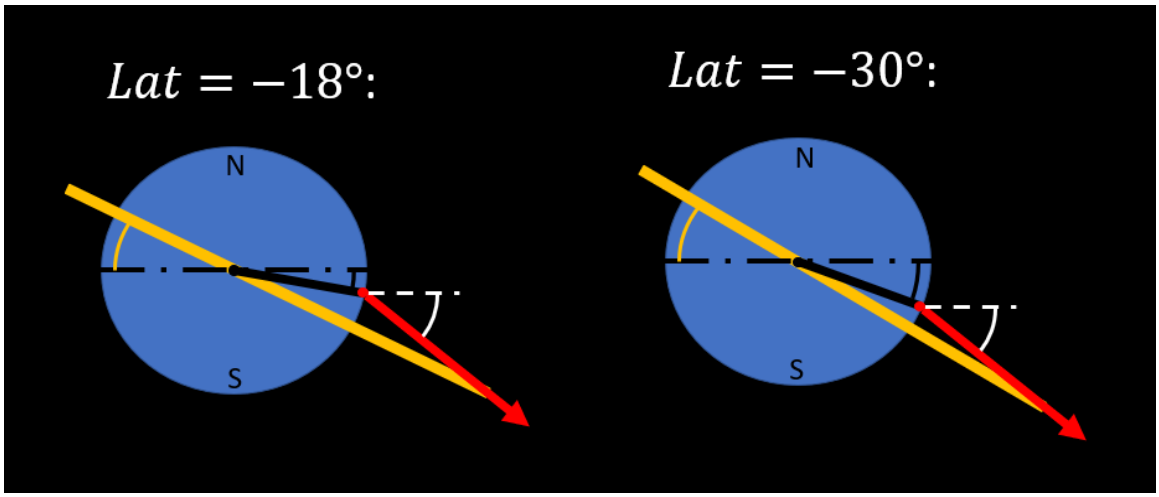

Figure 24 – Orbital Inclination vs Earthly Latitude of the Projector

Figure 24 above demonstrates the geometric relationship of orbital inclination and launch projector latitude. At both latitudes, there is a corresponding orbital inclination which keeps the trajectory angle (in white) the same. Thus, the main consideration in choosing an appropriate projector latitude is the zenith angle[11] it has to look through. The larger the zenith angle, the more air the beam has to travel through, and the more distortion it could obtain. Within the Atacama Plateau, the latitude which minimizes this effect is the one closest to Proxima's Declination. Therefore, the Earthly latitude of the projector and the orbital inclination of the mothercraft are set to be:

Launch Projector Latitude: $\mathbf{-30°}$

Orbital Inclination: $\boldsymbol{i = 61.32°}$

Therefore, the variables (or degrees of freedom) of the system that can be optimized for the AO system are: Semi-major axis (a) (which defines orbital period), orbital eccentricity (ϵ), and two new terms called Position of Release (p_r) and Position of Activation (p_A). Position of Release is how far ahead or behind the point of Apogee the mothercraft is at the moment of launch, and Position of Activation is how far ahead or behind the launch projector is from being directly below Apogee. These two parameters allow the simulation to probe whether or not tweaking the assumption of the launch geometry (Figure 13) can further reduce mothercraft/nanocraft separation. These two parameters are illustrated in Figure 25 below.

[11] The angle between the line of sight and the line that points directly upwards.

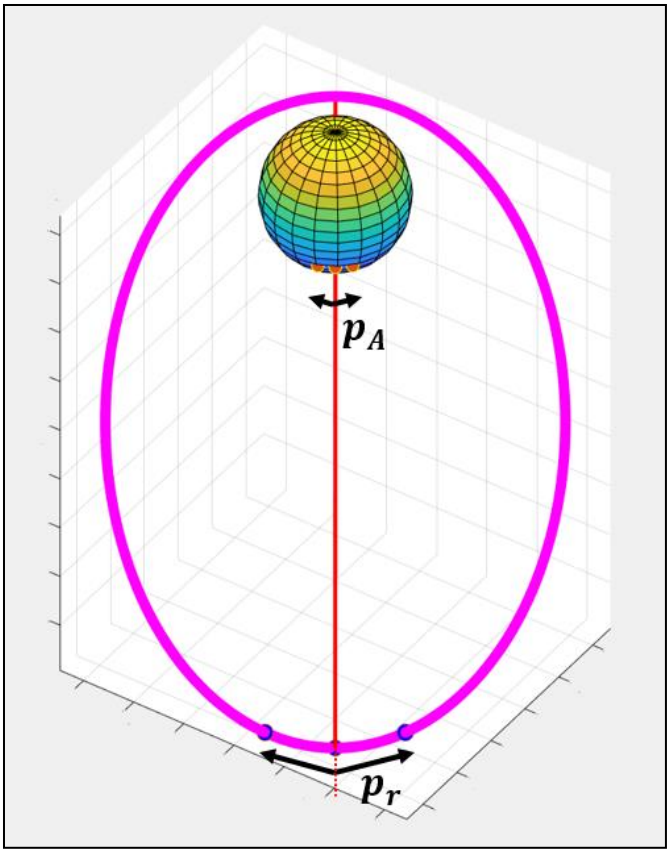

Figure 25 – The Launch Positions of Projector and Mothercraft

Lastly, there are some further bounds on these variables. The launch projector is designed to send not just one but hundreds of these nanocraft. By sending many clones of the nanocraft towards Proxima, the Starshot Program increases the statistical chances of mission success the same way insects ensure future reproduction by having many offspring. Because semi-major axis (*a)* defines orbital period (T_{orbit}), the system can only use those that yield orbital periods that are an integer multiple of 12 sidereal hours. This assures that at least one nanocraft can be launched every day with Proxima being in the same position in the sky. Also, the eccentricity should not be so high that the orbit's perigee intersects Earth's atmosphere. This would lead to a mothercraft re-entering the atmosphere and burning up from atmospheric drag. With these two constraints, the model could be run for every combination of the variables given in Table 1.

Parameter	Range of Values	Step Size
Orbital Period	[1 days, 10 days]	12hrs
Eccentricity	[0, 1]	0.02
Position of Release[12]	[-60m, 60m]	1m
Position of Activation	[-60m, 60m]	1m

Table 1 – Optimization Parameters

[12] The values of these positions are given in units of time. This is because the positions are defined discreetly with respect to time, and the exact distances from Apogee vary with orbital period and eccentricity.

2.5 Optimization and Model Results

The first parameters analyzed by the optimizer were Orbital Period and Eccentricity. To study their individual effects on mothercraft/nanocraft separation (α), the positions of release and activation are assumed to match with the launch geometry described below Figure 13 ($p_r = p_A = 0$).

Next, the optimizer was used to determine which combinations of orbital period and eccentricity minimized the angular separation of the mothercraft and nanocraft after a 30 second launch period. For the range of orbital periods and eccentricities laid out in Table 1, the optimizer simulated both craft's motion over a 30 second launch period and recorded final angular separations. The result is plotted in Figure 26.

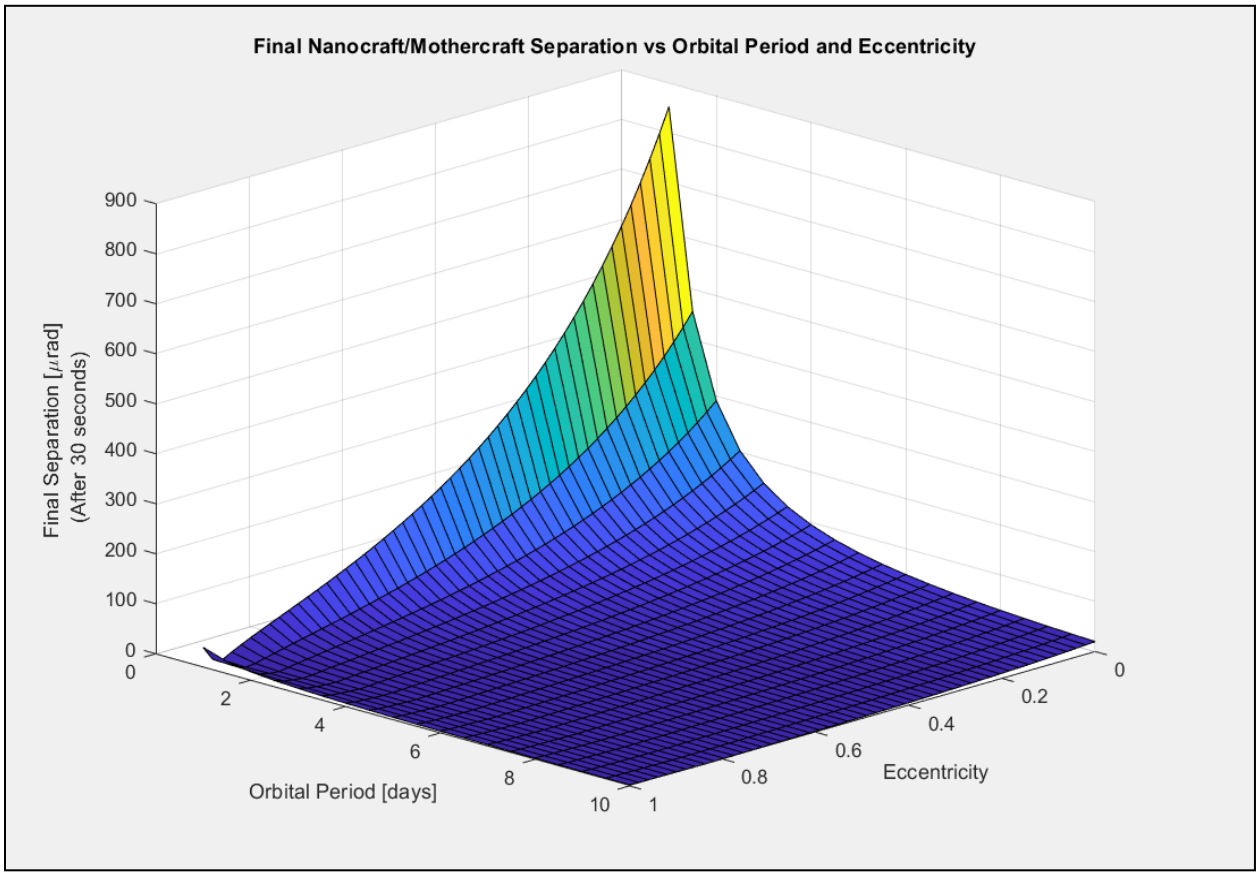

Figure 26 – Spacecraft Separation (t = 30s) vs Orbital Period and Eccentricity

As orbital period and orbital eccentricity increase, the final angular separation between the nanocraft and mothercraft decreases. This is expected because the larger these two orbital parameters are, the slower the lateral velocity of the craft is at its apogee. A slower lateral velocity means the mothercraft will separate in angle from the nanocraft much more slowly over time. However, circular orbits with a low orbital period (and small semi-major axis) have angular separations that drastically exceed the isoplanatic angle of $\theta_0 = 20\mu rad$. Taking the data obtained in Figure 26 above and separating those parameter combinations which keep the final angular separation (α) below $20\mu rad$, a list of potentially viable orbits for use by a mothercraft SLGS is

generated. This list contains orbital parameters which are not limited by angular anisoplanatism. However, because these orbits' final separations are below the isoplanatic limit, they still contribute some residual wavefront correction error. Using Equation 31, these contributions are plotted below in Figure 27.

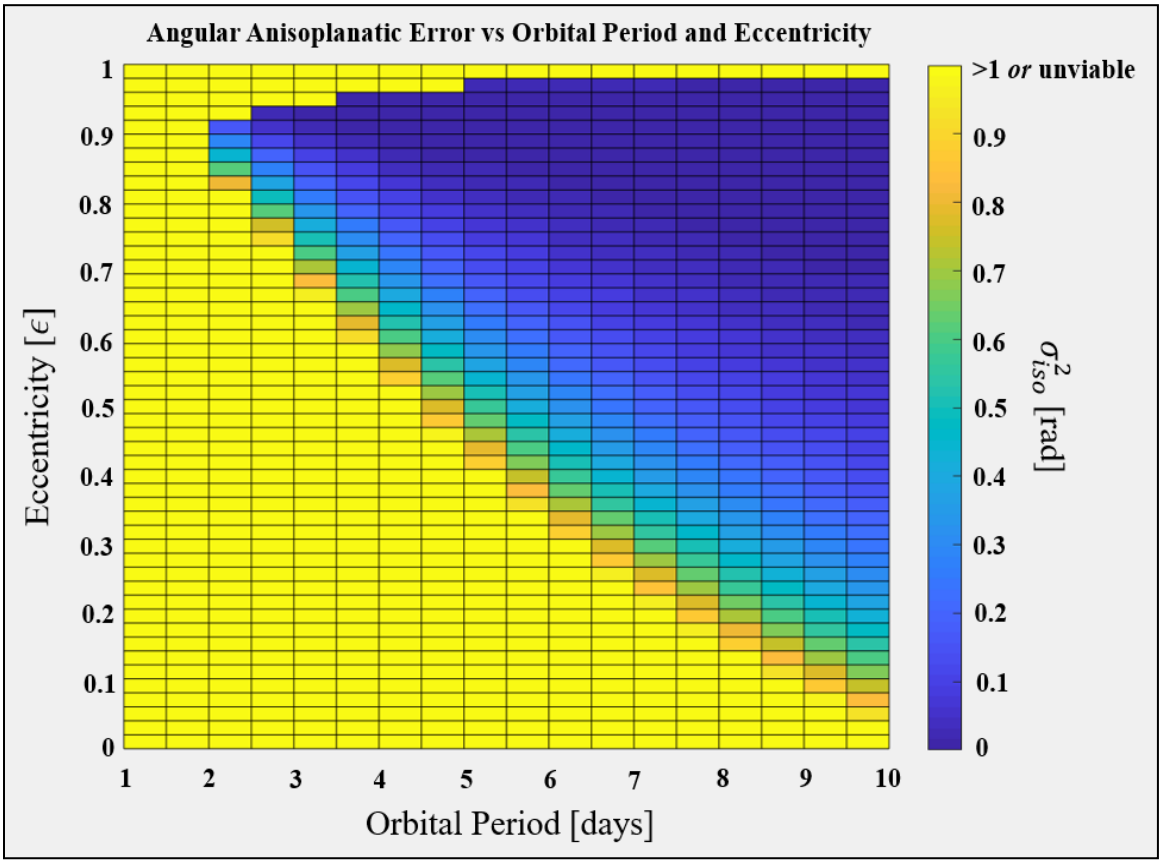

Figure 27 – Residual Error Contribution from Angular Anisoplanatism for Potentially Viable Orbits

The closer an orbit is to reaching the isoplanatic angle the more error it contributes to the AO system's correction. The large yellow region in the bottom left of the plot represents orbits that are too circular and whose average orbital velocities are too high for the SLGS to be a viable wavefront sensing method. The thin strip of yellow orbits at the top of Figure 27 represent those orbits whose perigees dip too close to Earth's atmosphere and are therefore unviable[28].

Within this list of potentially viable orbits, there may exist orbits that are limited by focal anisoplanatism (FA). Such orbits would have beacons that are too low in altitude and introduce too large of a cone effect for the end of launch. Because there is no FA error at the moment of launch, it is only after the nanocraft begins to accelerate away that a volumetric path difference between the mothercraft and nanocraft becomes appreciable. Using the final positions of the mothercraft and nanocraft during the 30 s launch period and Equation 34-35, the focal anisoplanatic error contributions for each orbit can be found (Figure 28).

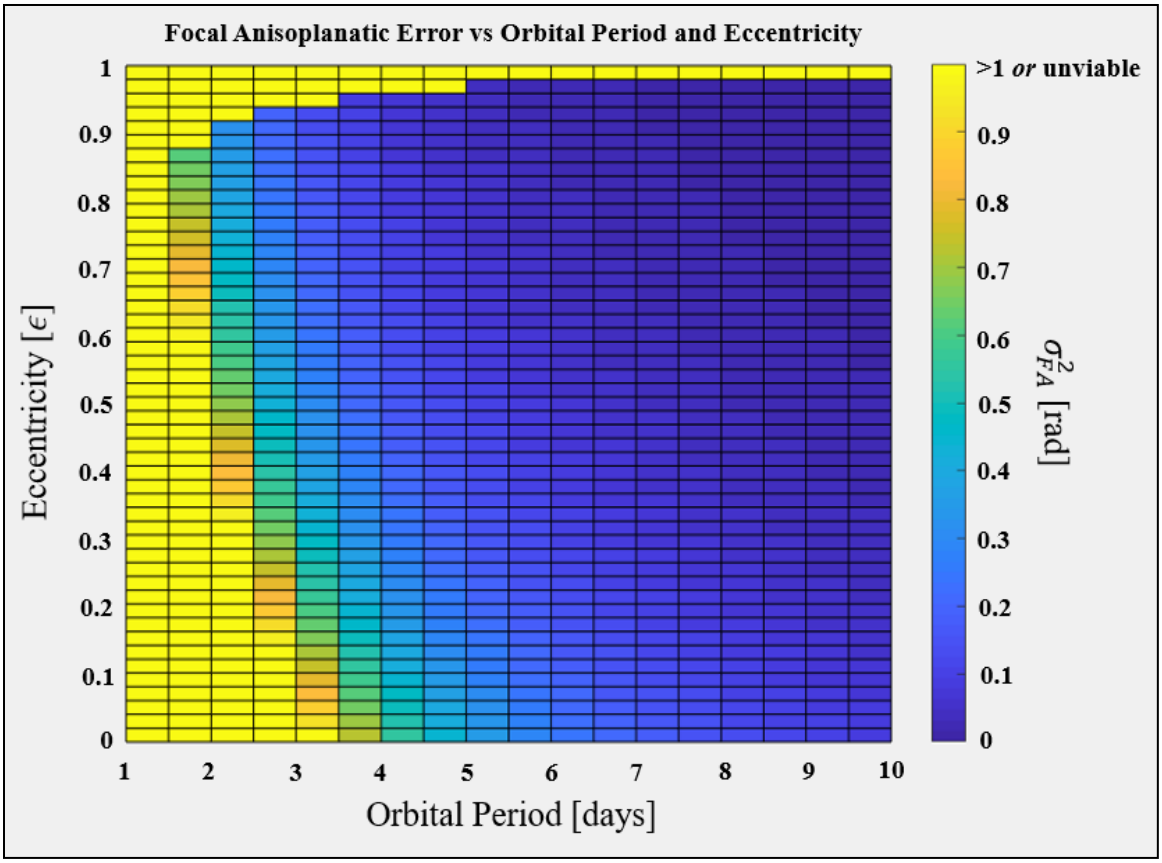

Figure 28 – Residual Error Contribution from Focal Anisoplanatism for Potentially Viable Orbits

FA does not contribute much correction error for the orbits deemed viable by isoplanatism in Figure 27. The largest errors here come from those orbits with the low eccentricities (low apogees), and thus low beacon altitude. As the orbital period increases, the height of the apogee (and therefore the beacon) increases and the FA error decreases. Ground based LGS systems have beacons which can only get up to around 90km in altitude, while the lowest an SLGS's beacon can viably go, according to Figure 27, is 37,000km in altitude. Adding the data from Figure 28 to Figure 27, the total reconstruction error that results from both focal and angular isoplanatism is generated in Figure 29.

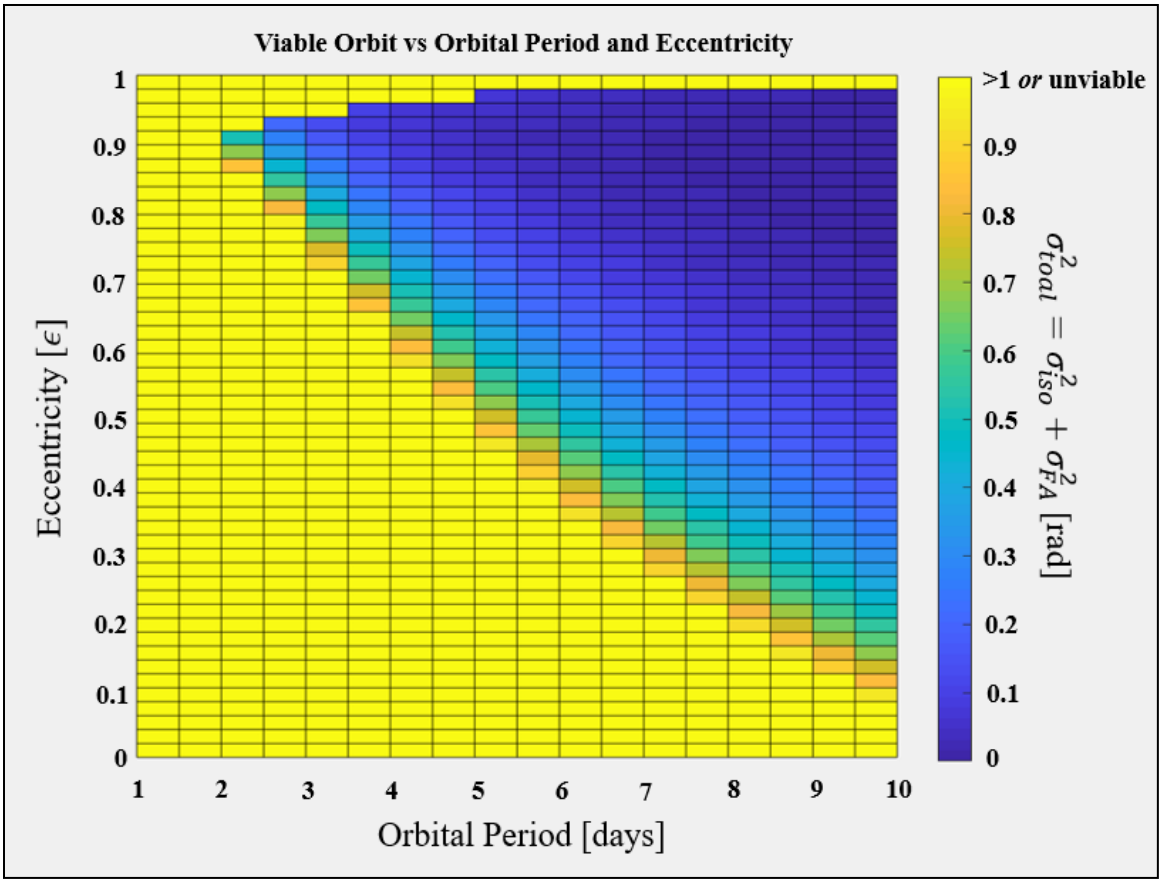

Figure 29 – Total Residual Error for Potentially Viable Orbits

To see the dynamics of how these errors change over the course of the first 30 seconds of a launch, one orbit can be analyzed. Choosing the smallest orbital period (and SMA) so as to maximize the frequency at which nanocraft can be launched, one optimized orbital parameter for the Starshot SLGS is given in Table 2.

System Parameter	**Parameter Value**
SMA | Orbital Period	106 Mm | 96 hours (4 days)
Eccentricity [ϵ]	0.88
Orbital Inclination [i]	-62 degrees
Latitude of Projector	-30 degrees

Table 2 – One Optimal Viable SLGS Orbital Configuration

The dynamic motion of the nanocraft and mothercraft, as well as some key analysis parameters over the 30 second launch period, are presented below.

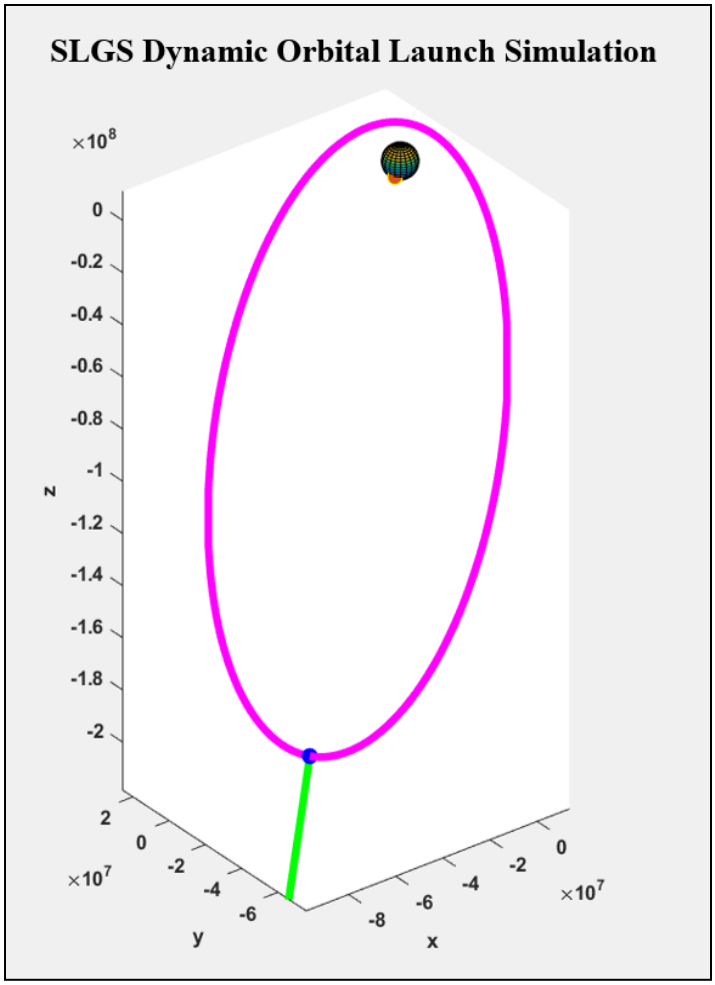

Figure 30 – A 30 s Launch Simulation of a Viable SLGS Orbit

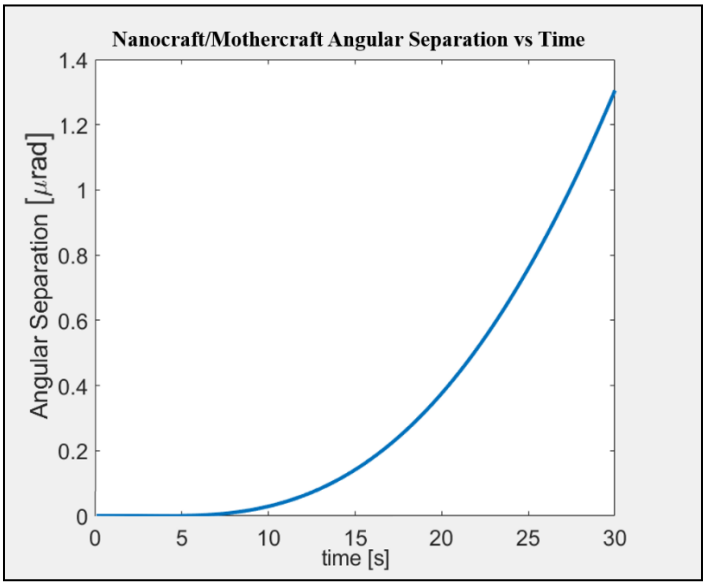

Figure 31 – Spacecraft Angular Separation vs Time

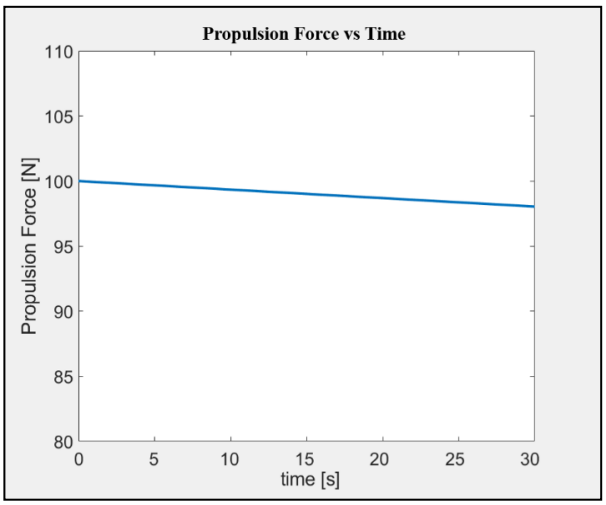

Figure 32 – Propulsion Force vs Time

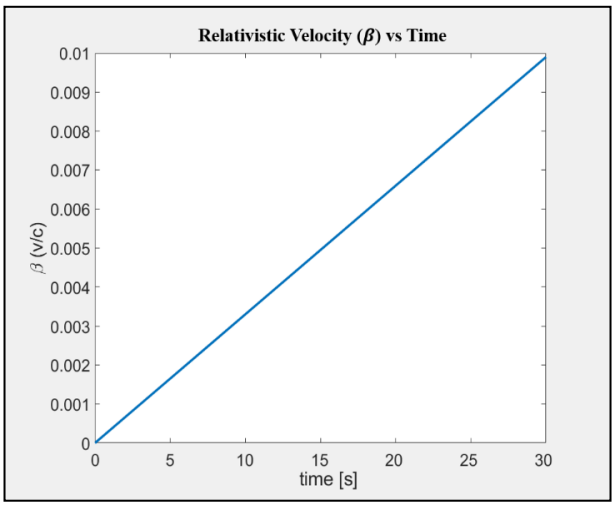

Figure 33 – Relativistic Velocity vs Time

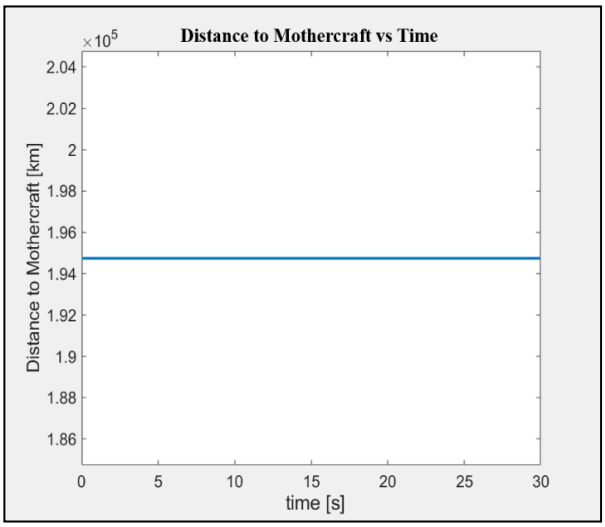

Figure 34 – Distance to Mothercraft vs Time

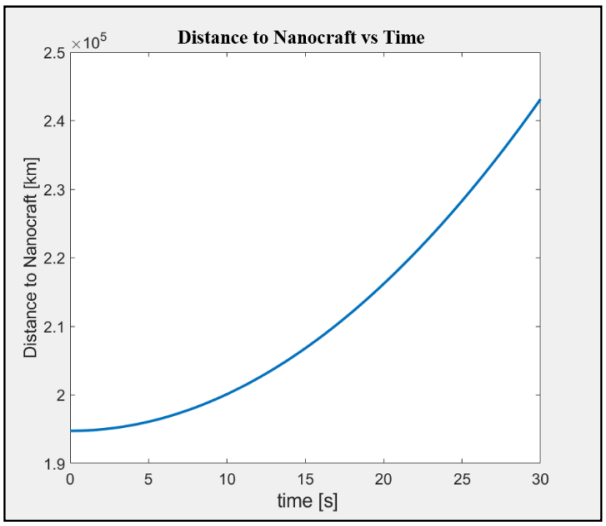

Figure 35 – Distance to Nanocraft vs Time

Figure 30 is a 3D plot of the Dynamic Numerical simulation of the parameters given in Table 2. Figure 31 shows how the Mothercraft and Nanocraft slowly drift apart, angularly, over time. The slow decrease in the propulsion force shown in Figure 32 comes from the power transfer loss caused by the nanocraft's relativistic velocity (Equation 16). Figure 33 shows that the nanocraft has reached the velocity (1% c) necessary for a sufficiently doppler shift reflected beacon return. Figure 34 shows that the Mothercraft's distance from the launch projector is largely the same over 30 seconds as compared the Nanocraft's distance (Figure 35).

Up until now, these analyses were performed using the orbital launch geometry assumed by Figure 13. This assumption stated that, at the moment of launch, the mothercraft was at its apogee and the launch projector was directly below its on Earth's surface ($p_r = p_A = 0$). To see how tweaking

this geometry affects the final mothercraft/nanocraft separation for the orbit listed in Table 2, the optimizer ran through each combination of p_r and p_a in Table 1 and recorded how much the final angular separation changed ($\Delta\alpha(t = 30)$) from the value found at the end of Figure 31 ($\alpha(t = 30) \approx 1.3\ \mu rad$). The result of this analysis is presented in Figure 36 below.

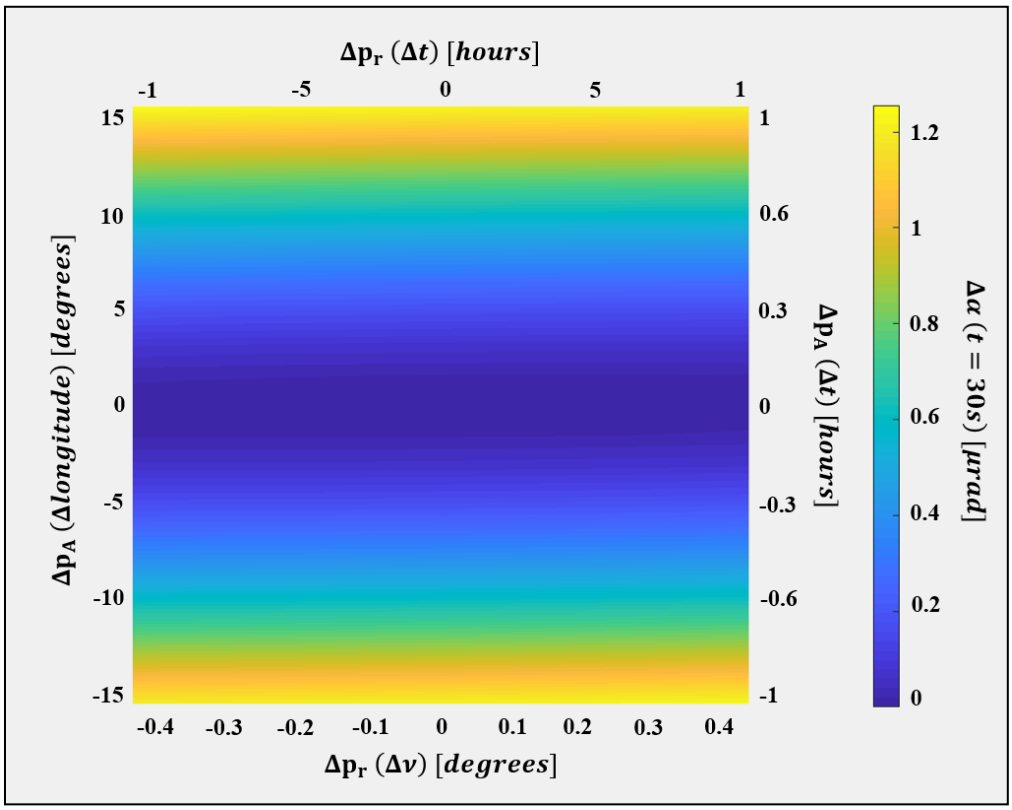

Figure 36 – Effects of Adjusted Launch Geometry on Final Angular Separation

The positions of activation and release do not significantly affect the final angular separation of the mothercraft and nanocraft (Figure 36). Because the mothercraft's orbital period is so long compared to a 30 second launch period, the angle its velocity vector makes with the propulsion force vector is largely the same over the hour ahead and behind its apogee. These means that the rate at which it departs from the launch projector's line of sight is largely the same over those p_r values. However, because the Earth rotates at 15° per hour, changing the position of activation has a much larger effect on the final separation. However, although the effect of p_A is much larger than p_r, the overall effect on system performance is low, with the maximal change in angular separation only being around 1.2 μrad within the range of parameters analyzed. Additionally, because no values in Figure 36 are negative, the optimal launch geometry for this orbit is the one assumed from Figure 13 ($p_r = p_A = 0$).

What is found from the above analysis is that 1) a mothercraft SLGS is a viable method for wavefront sensing for the first 30 seconds of launch and that 2) there exist a range of orbits which satisfy the performance criteria of focal and angular anisoplanatism. Choosing what specific orbit is ultimately be used for launch will depend on the projector's position, the type of mothercraft to be designed, the budget of this subsystem, and many other future system design considerations.

3. FLIGHT STABILITY ANALYSIS

The dynamics of the nanocraft were calculated under two assumptions that throughout the entire launch: 1) the beam is perfectly steered onto the nanocraft and 2) the nanocraft rides *stably* within the focus of that beam. However, residual correction and aiming error, as for any AO system, are expected. Random dense 'wedge' shaped layers of atmosphere will introduce fluctuations in the beam's overall tip and tilt, causing the beam's aim to deflect[10]. Some of these deflections may be large enough that the beam misses the sail entirely. Those that manage to still hit the sail, but do so off-center, will impart lateral forces that may push the sail into an unstable wobble that could lead to it falling out of the beam's path. Additionally, an imperfectly corrected beam shape will result in a non-uniform irradiance distribution at focus which can also lead to destabilizing lateral forces.

To determine how much the nanocraft can tolerate these destabilizing without falling out of the beam, an additional model was generated. This model simulates how the irradiance distribution of the projector's focus interacts with the nanocraft's sail and tracks how irregularities in this distribution affect the sail's lateral position in the beam during the duration of launch. Since these irregularities arise probabilistically, the success or failure of a given launch also varies probabilistically. In order to grasp how these lateral forces are expected to affect an average launch, a Monte-Carlo method was used to determine the statistical probability of launch success given an amount of residual error. These distributions can then be used to find the system's tolerances.

3.1 Radiation Pressure and Passive Stability

In order for the nanocraft to ride stably within the beam, the shape of both the sail and focus spot need to be uniquely controlled. The pressure felt by an object when light reflects off of it is referred to as radiation pressure. This pressure arises as a result of an exchange of momentum between a reflective body and an electromagnetic wave. When a normally incident beam with irradiance I_i perfectly reflects off of a surface, that surface feels a pressure:

$$\boldsymbol{P_i = 2\frac{I_i}{c}} \tag{36}$$

When light strikes a perfectly reflective surface with an angle of incidence θ_i and reflects at an angle $\theta_r = \theta_i$, the momentum change it experiences is always parallel to the surface's normal. This means that the force experienced by a perfect reflector from the reflection of a photon is always normal to its surface and proportional to the cosine of the angle of incidence. If this irradiance strikes an area A on the reflector, the radiation force is expressed[29]:

$$\boldsymbol{F_i(\theta_i) = 2\frac{I_i}{c} A * cos^2(\theta_i)} \tag{37}$$

The first cosine comes from taking the component of the incident light that is perpendicular to the surface and the second cosine comes from the cross sectional area (*A*) the beam lands on decreasing as $A * \cos(\theta_i)$.

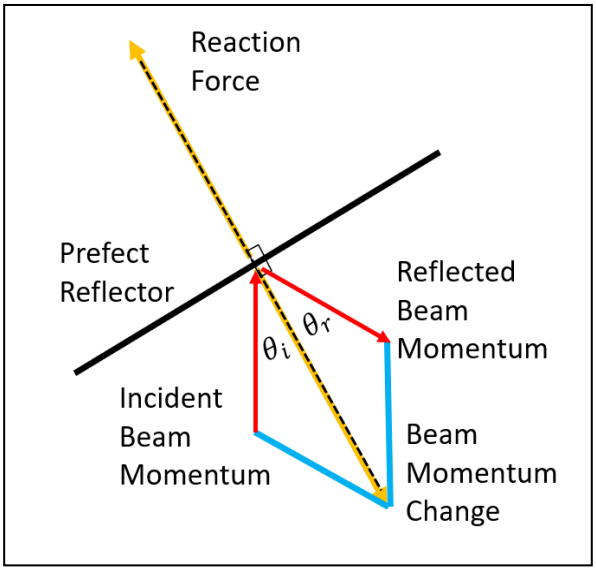

Figure 37 – Radiation Pressure

In order to determine the overall force a surface feels from a distribution of optical power, the integration of **Error! Reference source not found.** across the surface is used.

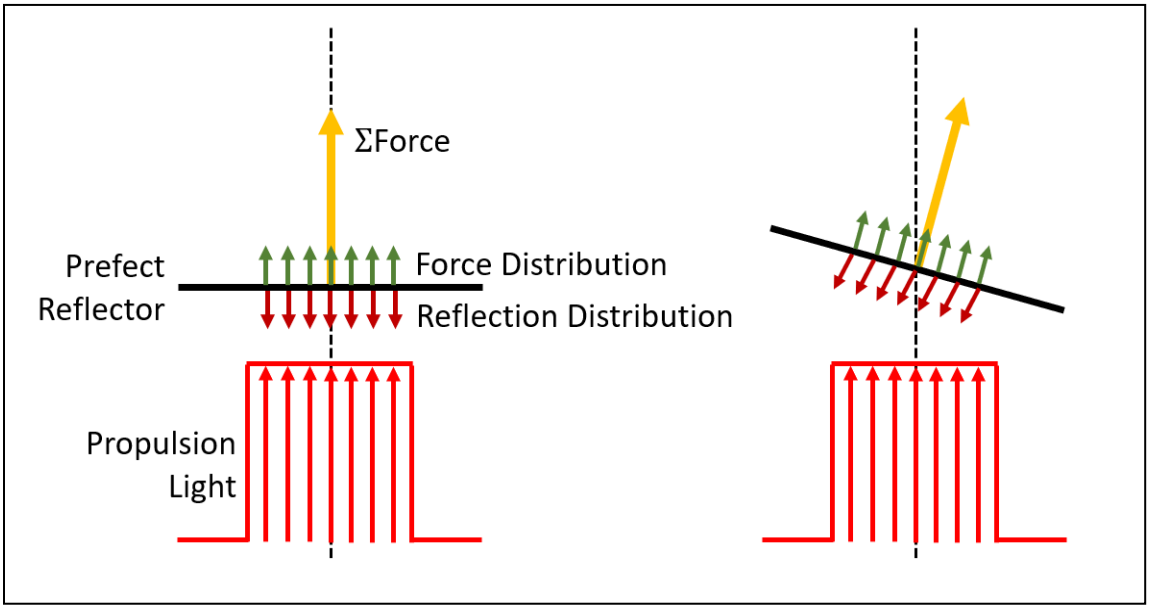

Figure 38 – Radiation Force Distribution and Unstable Configurations

In Figure 38, it can be seen how this irradiance distribution correlates to a force distribution. This force distribution is then summed to determine the overall force felt by the reflector. The scenarios depicted above demonstrate why a more sophisticated sail and focus geometry are necessary for flight stability. For a uniform irradiance distribution and a flat sail, the propulsion force is along the optical axis only when the sail oriented perfectly orthogonal to and centered on the optical axis (left scenario). Any perturbance that may tip or tilt the sail will introduce an angle of incidence and reflection that steers the force vector away from the optical axis (right scenario). The new

lateral component of force will cause the sail to move away from the optical axis. As the center of the irradiance pattern drifts away from the sail's center of mass, a rotational moment further increases the angle between the sail's normal and the optical axis. Like balancing a pencil on its tip, this self-compounding drift is what makes this sail-beam geometry unstable.

For a sail to ride stably in the beam, there needs to be some kind of reaction force to bring the sail back to the optical axis when the sail inevitably feels some perturbance. Many space flight systems use reaction control systems with thrusters to provide attitude control[30], but the nanocraft's 1g weight limit prevents it from having any such system onboard. Additionally, it is impossible for the launch projector to track the position of the nanocraft relative to the center of the beam because the travel time of photons back to the projector is too slow relative to the time it takes the nanocraft to fall out of focus. Therefore, this reaction force needs to be performed passively by the nanocraft.

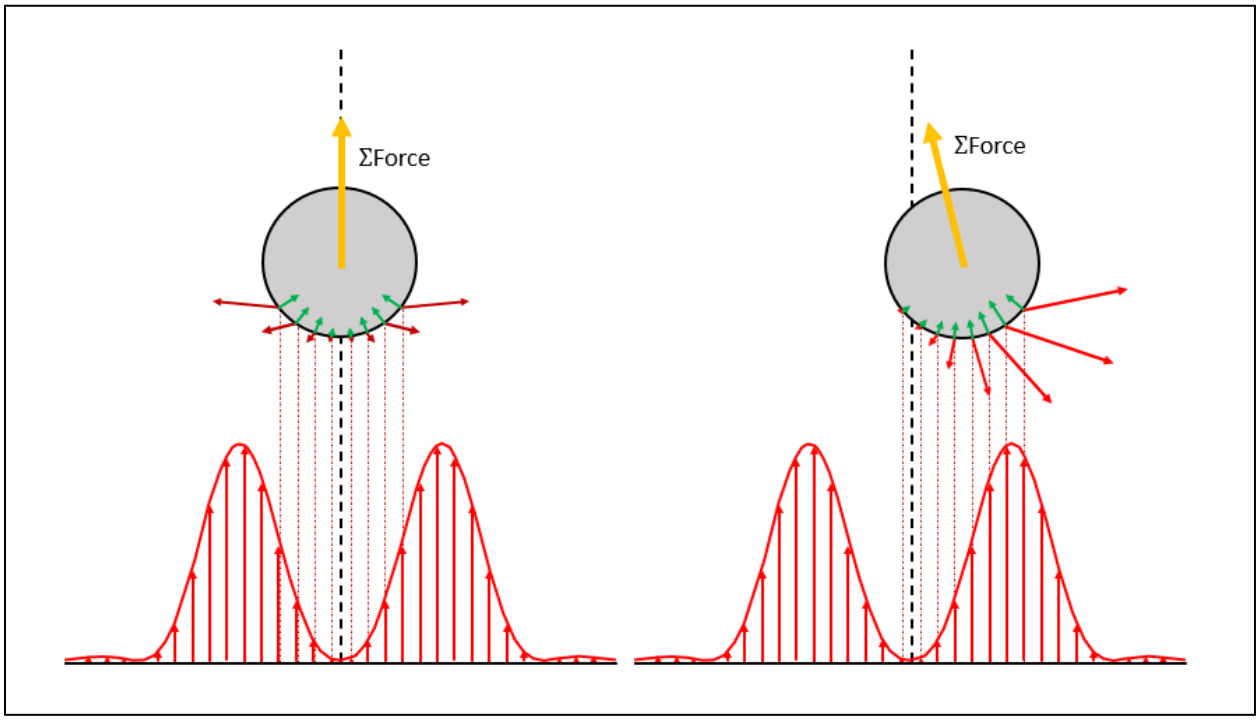

Figure 39 – A Passively Stabilized Beam/Sail Configuration

Figure 39 demonstrates the proposed stabilization geometry for the beam and sail. Here, a spherical sail rides within the center of a donut shaped beam focus (PSF). Unlike the Airy pattern which has a central peak that drops off away from the optical axis, a donut focus has a central zero surrounded by bright ring. In cross-section, the donut focus looks like two Airy peaks symmetric about the optical axis. On the left of Figure 39, the sail can be seen riding in the center of this donut irradiance pattern. Rays from each 'peak' reflect backwards and outwards from the optical axis. Because of this geometry's symmetry, the lateral components of force from one peak are balanced by those of the other. This leaves only longitudinal components of each force to sum to a propulsion force vector which is perfectly along the optical axis (in the direction of travel). On the right of Figure 39, the sail has been perturbed slightly to the right. As it drifts away from the donut's center, the sail feels more light from the right peak than it does from the left peak, and because of its spherical shape, more optical power is reflected to the right than to the left. This results in a net photon

momentum change to the right and therefore a net propulsion force vector to the left. This then drives the sail back to the optical axis.

There are two ways in which the launch projector can generate a donut shaped focus beam. The first is by defocusing the beam by ± 1 wave. Because of Fresnel diffraction, the pattern of the light at these two planes resembles the donut PSF described above.

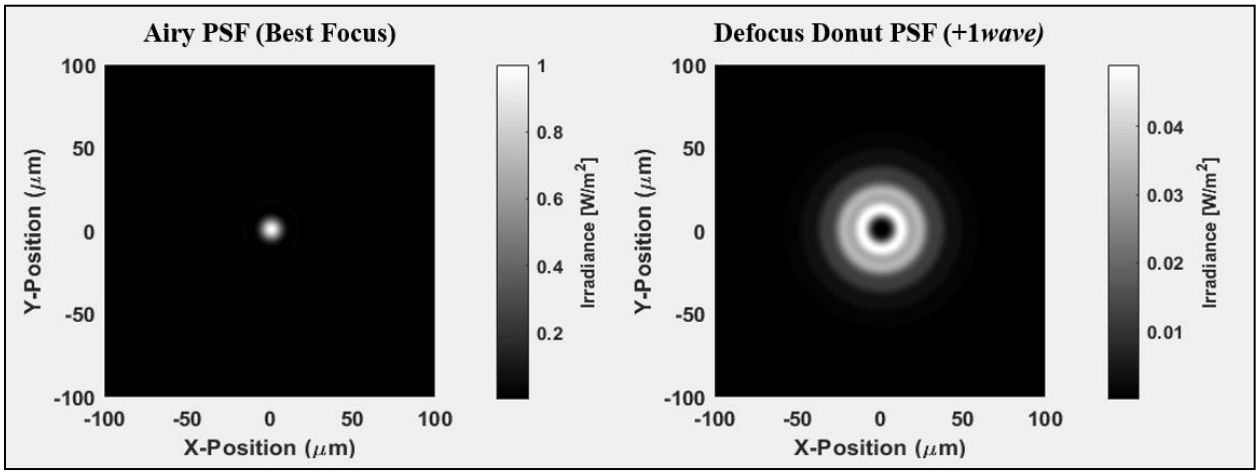

Figure 40 – Airy vs Defocus PSF

Defocusing the beam spreads energy from the central core of the Airy PSF to a bright ring surrounding a dark center. However, as seen in Figure 40, a lot of that energy is also spread into peripheral outer rings[13]. Because the sail would have to ride atop this donut's first ring, the large portion of energy in these outer rings would miss the sail entirely. This has the effect of further decreasing the power transfer efficiency (η_b) described in Equation 14. With the launch beam's optical power being 100 billion Watts, and with each Watt expected to cost around $0.01 to generate, it is economically necessary that the sail catch as much of the PSF's energy as possible.

The second method for generating a donut PSF is through manipulation of the propulsion light's phase profile at the launch projector's aperture. For the case of the Airy disk PSF, the phase and amplitude are equal across the exit aperture. When this phase profile diffracts to the focal plane, its PSF can be described by taking the 2D Fourier Transform of the phase profile. A donut PSF with a tighter bright ring than defocus can be generation by manipulating the launch projector's phase profile vary azimuthally from 0 to 2π. This 'spiral phase,' when propagated to the focal plane, generates a much more favorable donut PSF (Figure 41)[31].

[13] PSF were simulated on a system with a f = 1000m lens and a 1mm diameter entrance pupil

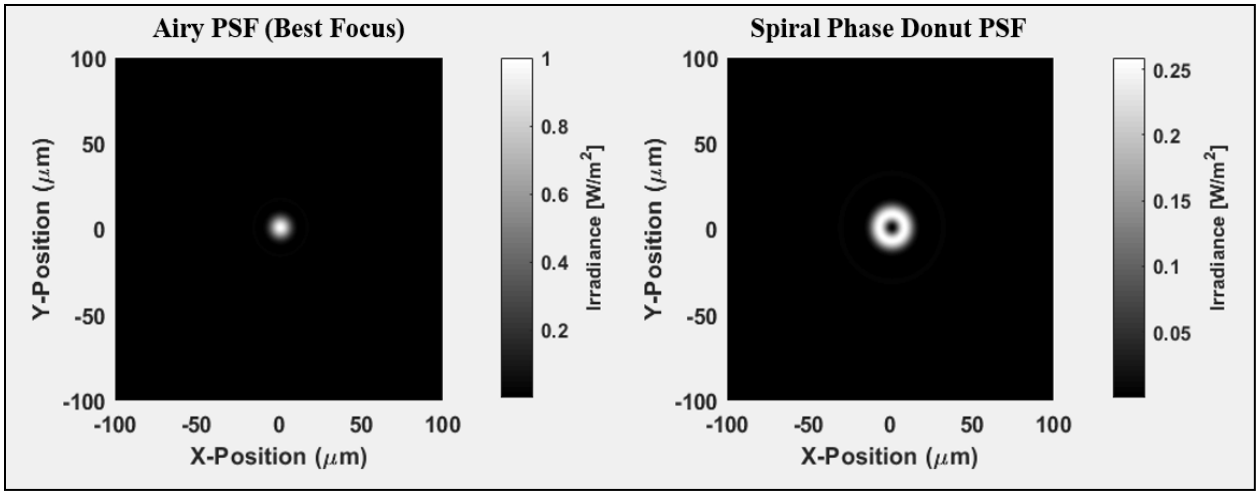

Figure 41 – Airy vs Spiral Phase Donut PSF

The majority of the beam's energy is contained within one bright ring. This is advantageous because the power transfer efficiency for this donut is much higher than for defocus. This is illustrated by the comparison of each PSF's encircled energy (Figure 42).

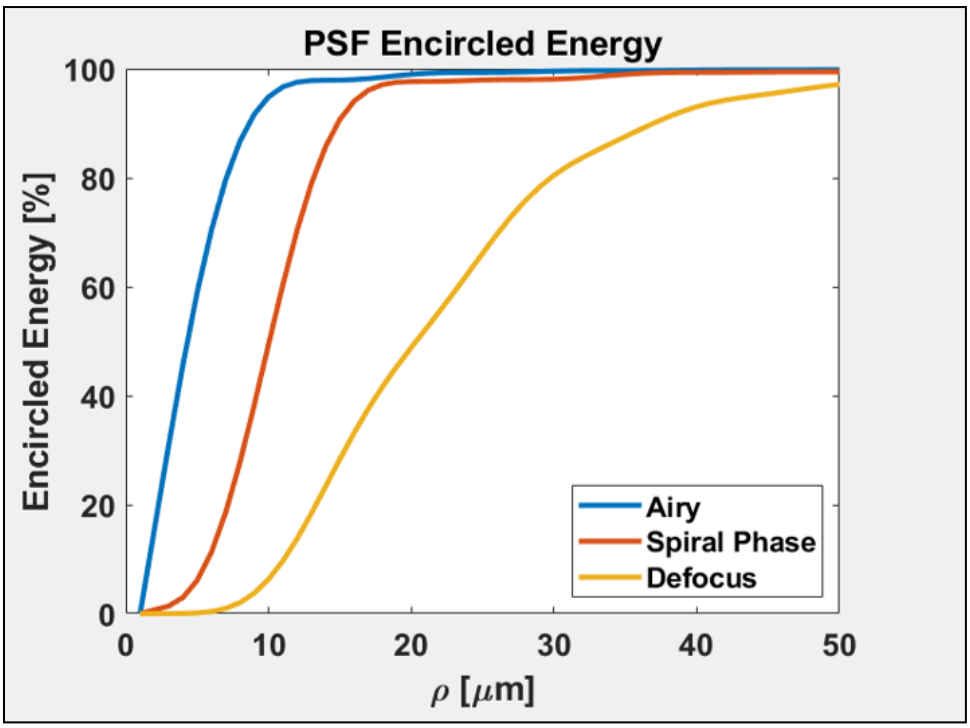

Figure 42 – PSF Encircled Energy

The diameter of a spiral phase donut is given by the following equation:

$$\boldsymbol{D_{Donut} = \frac{2}{3} D_{Airy} = \frac{2}{3} 2.44 \lambda F_{\#}} \quad \textbf{(38)}$$

This beam/sail geometry is an effective way to passively re-center the sail following a perturbance because the force field around the sail behaves like a potential energy well. The further the sail is away from the donut's center the more potential energy (PE) it has. As it moves back to the center, its potential energy is converted into kinetic energy (KE). Once recentered, its momentum carries it to the same potential energy height on the opposite side of the donut. This means that a perturbance with a given energy (E_p) will set the sail into a pendulum like oscillation across the donut. So long as E_p is below the escape energy of the donut's potential well (E_{esc}), the sail will not escape the beam. However, because this is occurring in the vacuum of space, these oscillations have no drag force with which to be damped and therefore continue indefinitely. This presents the problem that, throughout the launch, the sail's total lateral energy at any given time *t* is the sum of all the perturbances it experienced up to that point ($E_{lat}(t) = \Sigma E_{p,i}$) For the sail to stay within the beam, at no point can its total energy sum exceed that of the potential well's escape energy ($E_{lat}(t) < E_{esc}$). In the donut's case, this occurs when the sail has achieved an oscillatory amplitude that brings it up and over the peak of the donut (Figure 43).

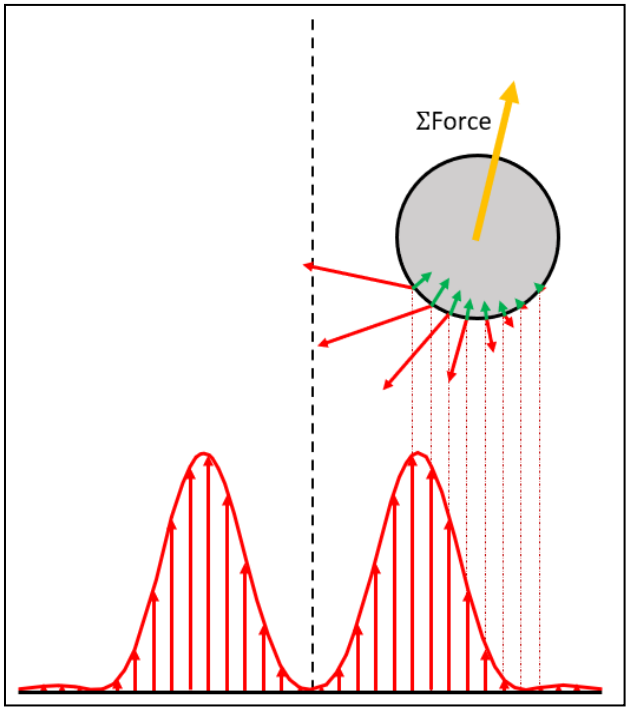

Figure 43 – Depiction of Sail Escape

3.2 Flight Stability Statistics

Whether a series of perturbances will sum to exceed E_{esc} depends on their sign, magnitude, and frequency of occurrence. The two perturbing forces on the sail are 1) the momentary decentering of the beam's pointing which arises from residual tip/tilt error in the launch beam and 2) momentary asymmetries in the beam's irradiance distribution which arise from post-correction residual wavefront aberrations. The frequency of occurrence of these perturbing forces is given by the Greenwood Frequency (f_G), while their signs and magnitudes depend on some statistical distribution. The Greenwood Frequency depends on the turbulence of the atmosphere at a given sight and the angle observed through that atmosphere. The more turbulent an area of the atmosphere is, the faster aberrations present themselves and, therefore, the faster perturbances arise. To determine if the sail can be expected to remain within the beam's focus throughout launch, a statistical analysis of these forces was performed. In this thesis, the effects of residual tip/tilt error on the sail's stability are discussed and analyzed, and their limits are defined[14].

Wavefront tip and tilt describe the angle between a wavefront's normal and the optical axis. In OPD, it is the difference between the edge of the wavefront from the edge of its reference plane (Figure 44).

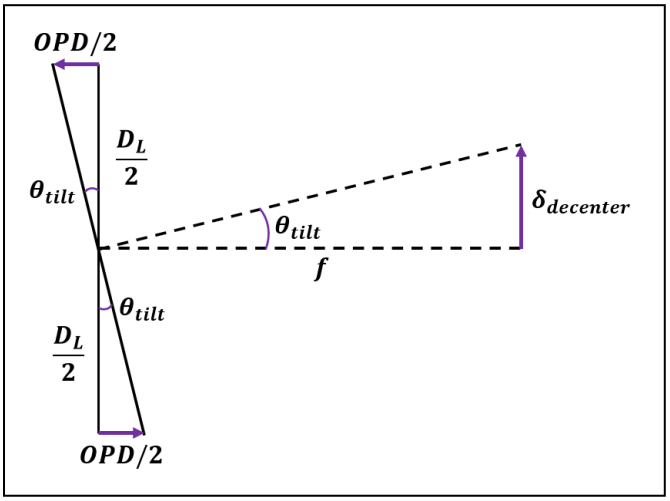

Figure 44 – An Illustration of Wavefront Tilt Error

The shape of a system's PSF is not affected by wavefront tip or tilt. Rather, the effect is to decenter the PSF from its ideal on-axis location. The amount of decenter depends on the aperture's size, the distance to focus, and the OPD of the wavefront from its reference plane:

$$\boldsymbol{\delta_{decenter} = OPD\,\frac{f}{D_L} = OPD * F_{\#}} \tag{39}$$

The frequency at which a wavefront's tip and tilt changes is slower than the Greenwood Frequency, at around one ninth f_G[32]. This frequency, referred to as the *Tyler Frequency* (f_T), describes how

[14] The effects of residual correction errors on the sail's flight stability is a current topic of research by other members of the University of Arizona's Starshot team.

often the wavefront's tip/tilt OPD changes, and therefore, how often the sail is perturbed by the decentering of the donut PSF from the optical axis (See Appendix A).

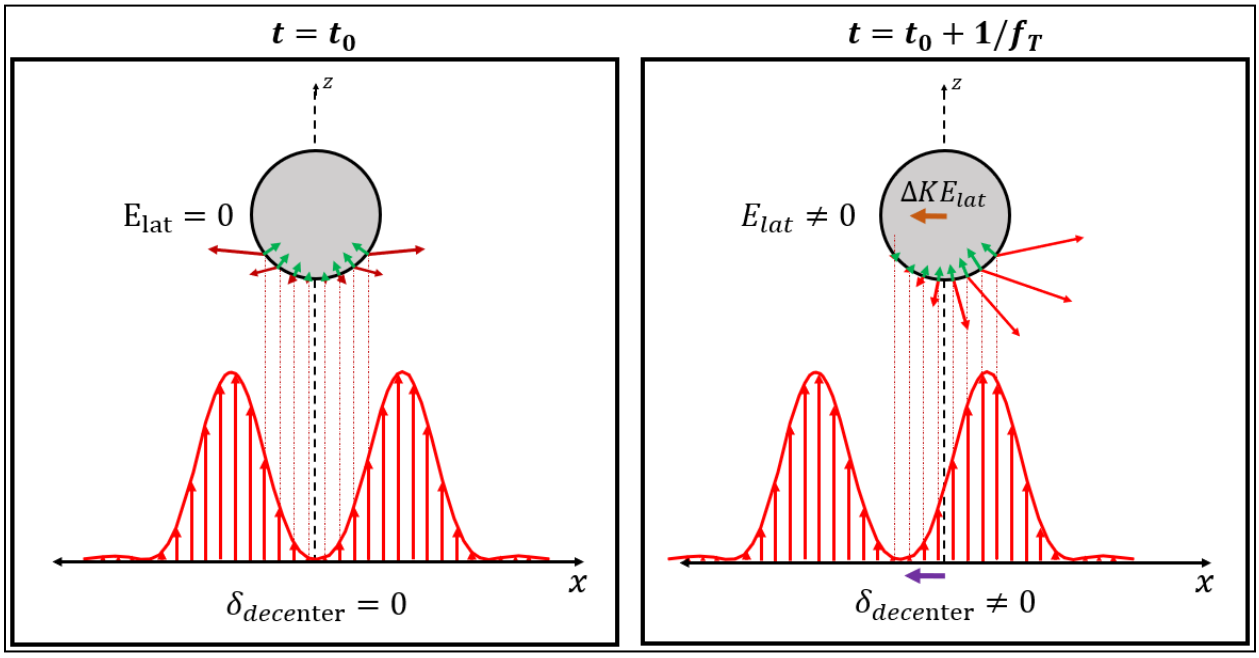

Figure 45 – Tip/Tilt Sail Perturbance

Figure 45 illustrates how the sail is perturbed by wavefront tip and tilt. At some time $t = t_0$, the sail is perfectly centered within the potential well, has no lateral energy, and the propulsion beam has no tilt. After a Tyler period ($1/f_T$) has elapsed, the potential well has decentered a distance $\delta_{decenter}$. At this time ($t = t_0 + 1/f_T$), the sail experiences a force towards the new central location of the potential well. This momentary nudge, or perturbance, changes the magnitude of the sail's lateral kinetic energy (KE_{lat}) in the direction of the potential well's new center.

With the sail set in motion, any future nudges as the result of tip/tilt will either add or subtract from the sail's lateral energy. If the well decenters in the same direction that the sail is moving at that moment, the sail's E_{lat} will increase. Conversely, if the well decenters in the direction opposite to the sail's motion, E_{lat} will decrease. Because the sail's oscillation is periodic, it spends the same amount of time with a positive lateral velocity as it does with a negative velocity. Additionally, the magnitude distribution of tip/tilt error, by the Central Limit Theorem, is expected to follow a normal distribution whose mean (μ) is 0 and whose standard deviation (σ) depends on the tip/tilt correction quality of the AO system[33]. The combination of these two facts means that it is equally likely that, at any moment during flight, a perturbance will either increase or decrease the sail's E_{lat}. In statistical terms, the conditional expectation of the sail's E_{lat} after a perturbance is equal to the sail's E_{lat} before the perturbance[34].

Having a conditional expectation of the next value in a sequence equal to the present value is an example of a Wiener process[35]. An intuitive example of a Weiner process is the running sum of wins and losses of a coin toss game. A win (heads) awards 1 point, while a loss (tails) subtracts 1 point. Because heads and tails are equally likely, the conditional expectation of one's earnings after a coin toss is equal to how much they had earned before the coin flip. Of course, with a coin

flip, the value must increase or decrease, so the running sum of earnings will walk randomly up and down.

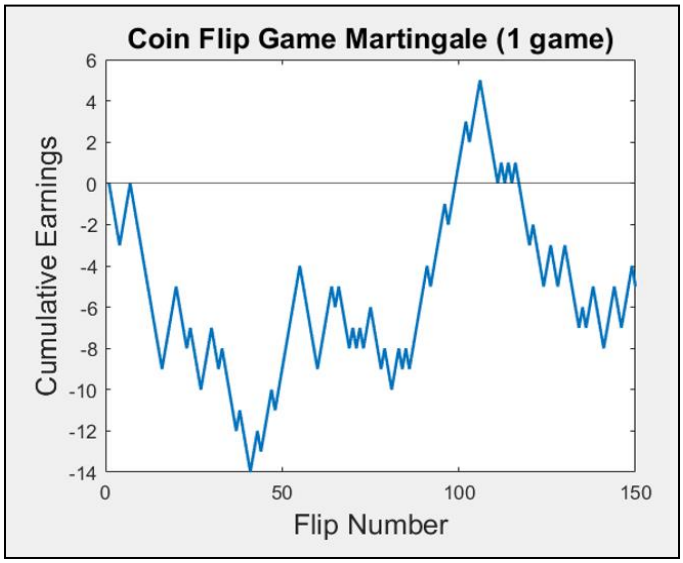

Figure 46 – Coin Flip Martingale for 150 Flip Iterations

The pattern that results is known as a continuous-time Martingale. Like the running sum of the coin toss game, the sail's E_{lat} cumulative value also generates a Martingale pattern. This stochastic process is also known as Standard Brownian Motion[36].

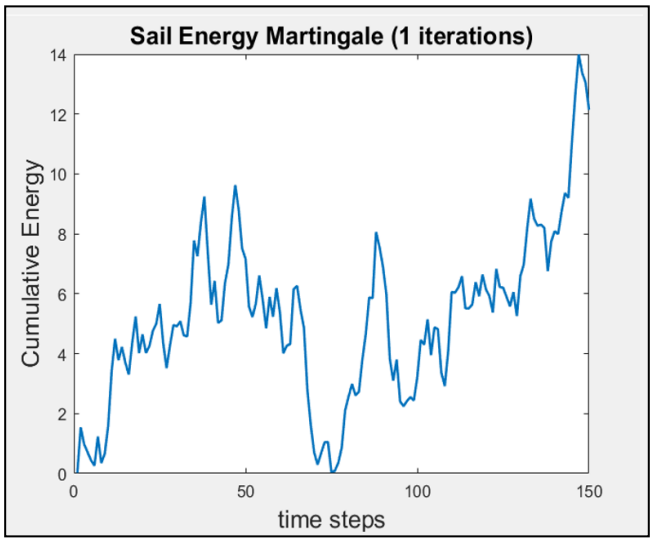

Figure 47 – Sail Energy Martingale for 150 Perturbance Iterations

Figure 47 shows the Martingale pattern generated in the same manner as the coin toss game except that the next value of X was chosen from a normal distribution with a $\mu = 0$ and a $\sigma = 1$. This pattern more accurately simulates how the sail's cumulative energy will behave. Unlike the coin toss game, however, cumulative energies for a sail's simulation are strictly positive, as they are proportional to the amplitude of oscillation. This was accounted for in Figure 47 by plotting the absolute value of the accumulated energy. However, the process that governs its random walk

remains the same. Like the coin toss game, the shape of this martingale pattern can change widely depending on random values that arise step by step.

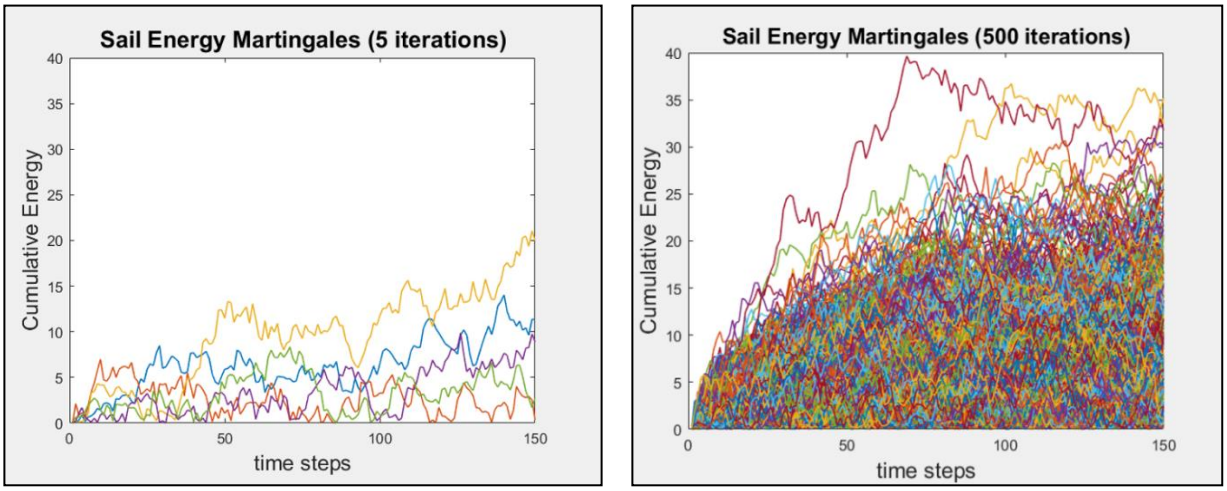

Figure 48 – Sail Energy Martingales for 5 Simulations (left) and 500 Simulations (right)

Although the growth of the lateral energy is random, Figure 48 demonstrates that there is some statistical distribution on what maximum lateral energies are. Qualitatively, the maximum achievable energies given the above simulations seems to be around 30-40. Quantitatively, the probability distribution function that describes the distribution of maximum accumulated values for a Martingale is known as an Inverse Gaussian Probability Distribution Function (PDF)[37], and is described by:

$$f(x;\mu,\lambda) = \sqrt{\frac{\lambda}{2\pi x^3}}\, exp\left(-\frac{\lambda(x-\mu)^2}{2\mu^2 x}\right) \quad \textbf{(40)}$$

Where μ is the mean and λ is its shape factor. This distribution can be illustrated by fitting the distribution of maximum accumulated energies for a 100,000 run Martingale simulation:

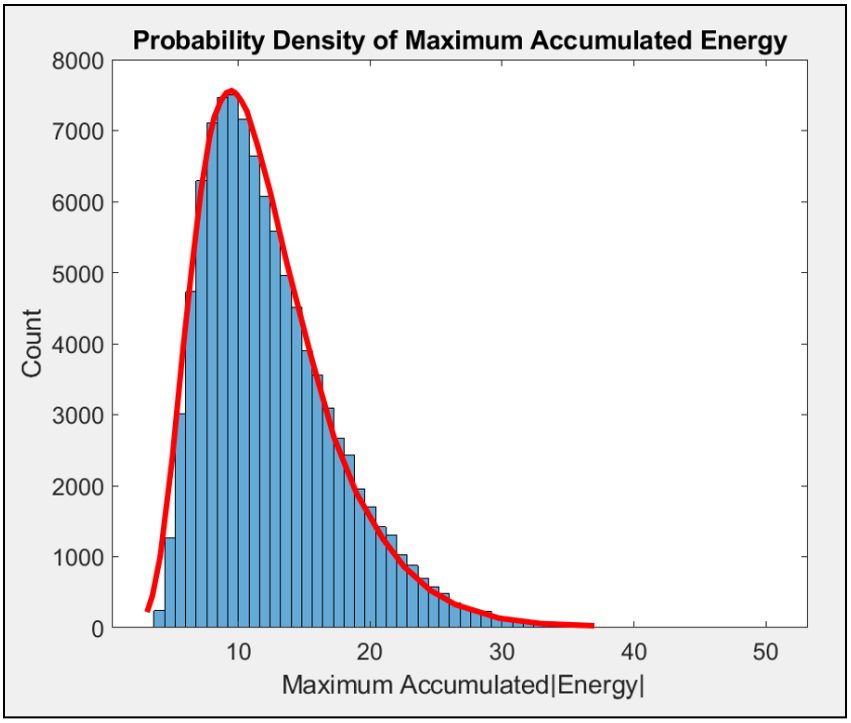

Figure 49 – The Inverse Gaussian Distribution of Max Accumulated Energy

The shape of the Inverse Gaussian PDF can be understood by two heuristics. First, it is unlikely that the maximum achieved accumulated energy is low (close to 0). In terms of the coin toss game, this would require flipping a heads after every tails, and tails after every heads, for 100,000 consecutive flips. Second, it is unlikely the maximum accumulated energy is incredibly high. This would require flipping heads (or tails) for the majority of 100,000 consecutive flips.

As suspected from Figure 48, the upper limit for achievable maximum accumulated energies shown in Figure 49 is around 30-40. In general, this 'limit' on achievable maximum accumulated energy is controlled by the standard deviation of the tip/tilt error's normal distribution. The larger the standard deviation, the bigger the perturbances possible, and the faster energy is accumulated over the same time period.

For the sail to remain within the projection beam throughout launch, the random walk of the sail's lateral energy must not exceed the escape energy of the donut's potential well. Since the sail's maximum achievable energy is a probability, this requirement must be restated in turns of probability of success. In statistical terms, this requirement can be restated: for the sail to have a 90% chance of staying within the projection beam throughout launch, the Inverse Gaussian Cumulative Distribution Function for the maximum accumulated E_{lat} must be less than or equal to 0.9 at the value E_{esc}. A cumulative distribution function (CDF) gives the probability that X will take on a value less than or equal to *x*. Mathematically, it is the integration of a PDF from -∞ to x

(Equation 41). If the CDF is equal to 0.9 at the well's escape energy, then there is a 90% change the sail will not exceed this limit.

$$\boldsymbol{F(X;\mu,\lambda)} = \int_{-\infty}^{\boldsymbol{x}} \boldsymbol{f(x;\mu,\lambda)} \tag{41}$$

To determine how the sail's probability of success responds to various tip/tilt standard deviations, a flight stability model was created to simulate the motion of a spherical sail within a spiral phase donut PSF. This model simulates normally distributed tip/tilt perturbations and tracks the accumulated E_{lat} by the sail over time. This model is then iterated several thousand times to generate a distribution of E_{lat} martingales whose maximum values can be fit to an Inverse Gaussian PDF to determine their expected performance. Once this is performed on several distributions of tip/tilt, the mathematical relationship between tip/tilt magnitude and percent flight success can be established.

3.3 Flight Stability Model

To generate an E_{lat} martingale for a sail within a donut PSF over a given launch, a Dynamic Numerical Model for the motion of a circular sail with the cross-section of a decentering spiral phase donut potential well was created. This 1D simulation operates under the assumption that tip and tilt are orthogonal. In other words, by determining the $E_{lat,x}$ Martingale distribution's relationship to tip, the $E_{lat,y}$ distribution's relationship to tilt is assumed to be the same. This has the added benefit of not being computationally demanding.

The potential well of the beam's focus was modelled by taking the central cross section of the 2D Fourier Transform of a circular aperture with a spiral phase profile. This cross section could then be scaled horizontally using Equation 38 and scaled in amplitude (and irradiance) to satisfy that a sail in the center of the donut experiences a 100 N propulsion force in the direction of the optical axis. The reflective surface can be modelled simply with the equation of a semi-circle with radius $r_S = 2m$.

The component of the system's power transfer coefficient that is affected by diffraction, η_b, is related to the ratio between the sail's radius and the radius of the donut ($r_d = D_{donut}/2$). A sail whose radius is smaller than the donut's will experience a deeper potential well but will miss too much energy. The bigger the sail's radius, the more light it will catch. However, increasing the sail's radius also reduces the depth of the potential well it feels. This is because the sail will catch more light from the peak opposite from its position relative to the optical axis thus reducing the lateral restoring component of the propulsion force vector (Figure 50).

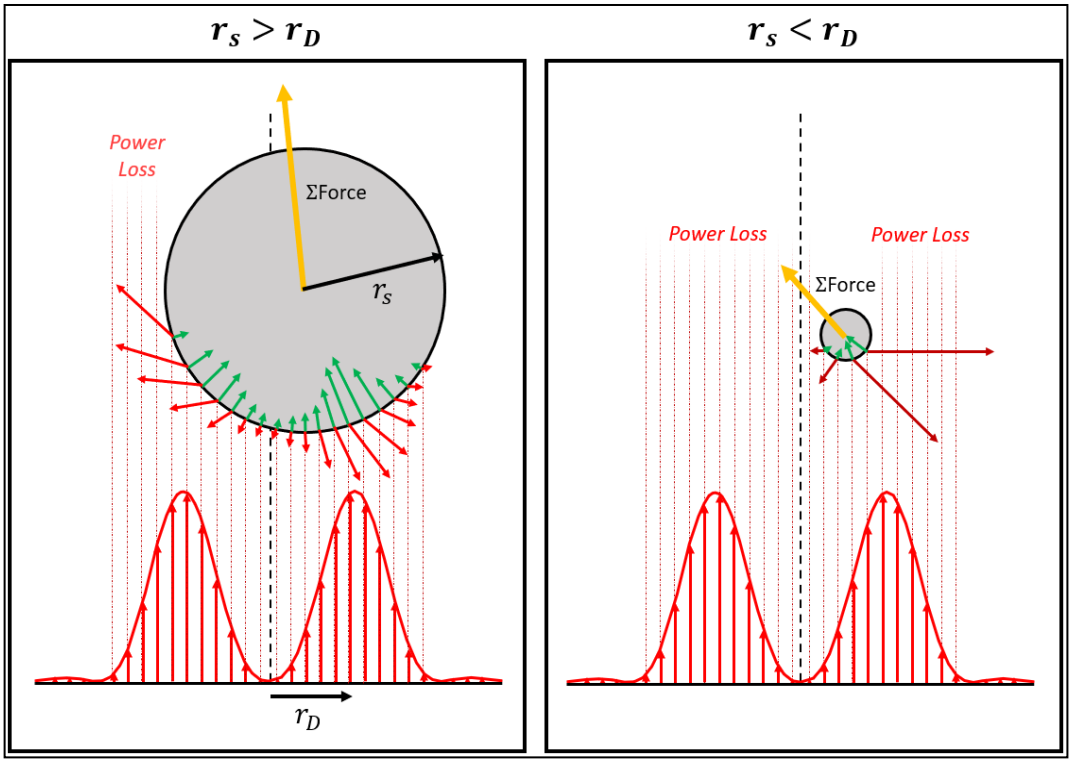

Figure 50 – Sail Radius vs Potential Well Radius

It was assumed that the sail's radius throughout the launch is equal to the radius of the donut ($r_s = r_D$). As long as the diffraction limit of the donut at the farthest focal distance does not exceed the sail's radius, this assumption could be achieved by the launch projector through selective apodization of its aperture throughout launch. Although this is not expected to be the case at the distances the nanocraft is expected to reach at the end of 10 minutes, this assumption represents the best case scenario for the sail's power capture efficiency.

For sufficiently small time steps, the sail's lateral acceleration, velocity, and position can be calculated using Equation 36-39 and the same Dynamic Numerical Modelling method described in section **Error! Reference source not found.** (here thereafter the "Flight Stability Dynamic N umerical Model" or FSDNM). The position of the sail's center relative to the optical axis is defined x_s. To simulate the effects of tilt in the beam, the Spiral Phase PSF is *decentered* relative to the optical axis by the parameter x_d. At the beginning of the simulation ($t = 0$), $x_s = x_d = 0$. As time progresses, the position of the sail (x_d) decenters by $\delta_{decenter}$. The frequency at which x_d moves to a new $\delta_{decenter}$ is given by f_T, and the magnitude of $\delta_{decenter}$ is defined by a normal distribution with a mean $\mu = 0$ and a parameterizable standard deviation (σ).

3.4 Stability Model Results

Given a sail and donut radius of $r_s = r_D = 2m$, the shape of the potential well is determined by the FSDNM. The sail is released some distance x_s from the optical axis (where the PSF will be fixed) and the maximum lateral velocity it achieves over one period of oscillation is measured[15]. This maximum velocity can be used to determine the maximum lateral kinetic energy (KE_{lat}) which is equal to the potential energy associated with the well at the position x_s.

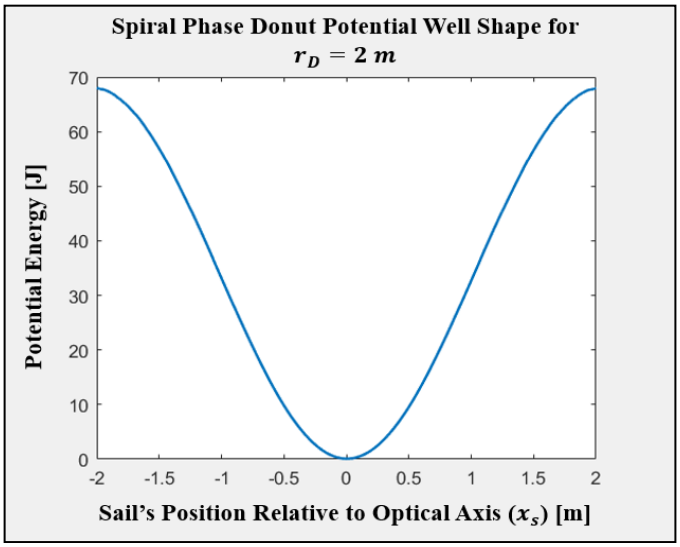

Figure 51 – Spiral Phase PSF Potential Well Shape for a 2m Sail

The escape energy of Spiral Phase PSF's potential well is $E_{esc} = 68$ J (Figure 51). Therefore, the sail's lateral energy at any given point in time must not exceed this limit. Because of the potential well's shoulders, the oscillation frequency is not uniform for every initial displacement (x_s). For example, when $|x_s|$ approaches r_d, the sail feels less and less radiation pressure in the direction towards the center of the well. At the extreme of $|x_s| = r_d$, there is no oscillation, and the sail rests unstably on top of the donut's ring (much like the scenario depicted in Figure 28. However, for values of $|x_s| < 0.9 * r_d$, the oscillation frequency of the sail in this well is approximately 35 cycles per second (Hz). This is pretty fast for an object 4 m in diameter, but it is expected given such immense radiation pressures.

To demonstrate one simulation of the FSDNM, a sail is placed at the center of the above potential well and its position over time is tracked given an initial arbitrarily defined $\delta_{decenter}$ standard deviation and a Tyler Frequency $f_T \approx \frac{1}{9} f_G \approx 100Hz$. For Figure 52 below, the $\delta_{decenter}$ standard deviation was set to $\sigma = 15mm$.

[15] Assuming the same system parameters defined in section **Error! Reference source not found.**: $m_{nano} = 1g$, $P0 = 100GW$, and $Reflectivity = 1$.

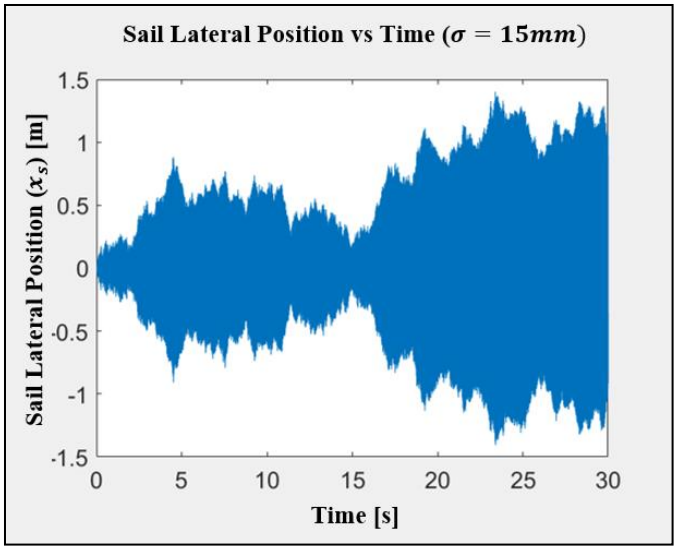

Figure 52 – Sail Lateral Position vs Time for a Single 30 second Simulation

Because the sail's oscillation frequency is around 35 Hz, its motion from one side of the well to the other cannot be seen over this long of a time scale. However, the amplitude of its oscillation can be seen as the boundary of this shape. To see the side to side oscillatory behavior of the, the data in Figure 52 can be plotted for a shorter time scale.

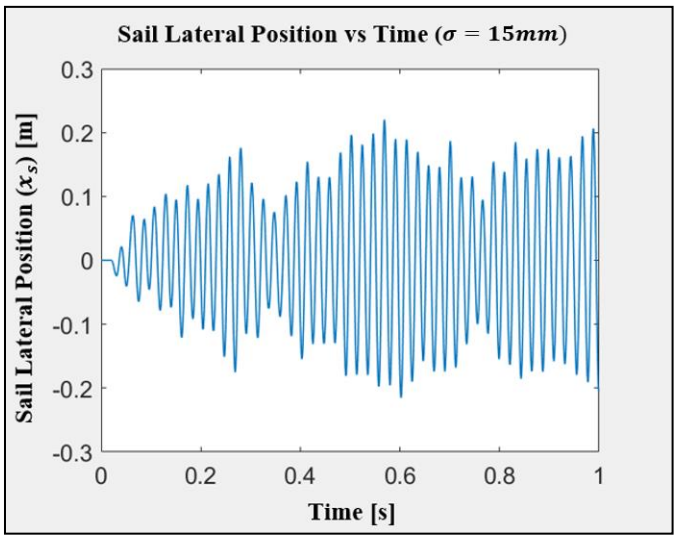

Figure 53 – Sail Lateral Position vs Time for a Single 1 second Simulation

Over this 30 second simulation, the sail's lateral energy over time can be approximated over each of these cycles by the maximum achieved kinetic energy (i.e. the slopes of the sail's position when it crosses the optical axis).

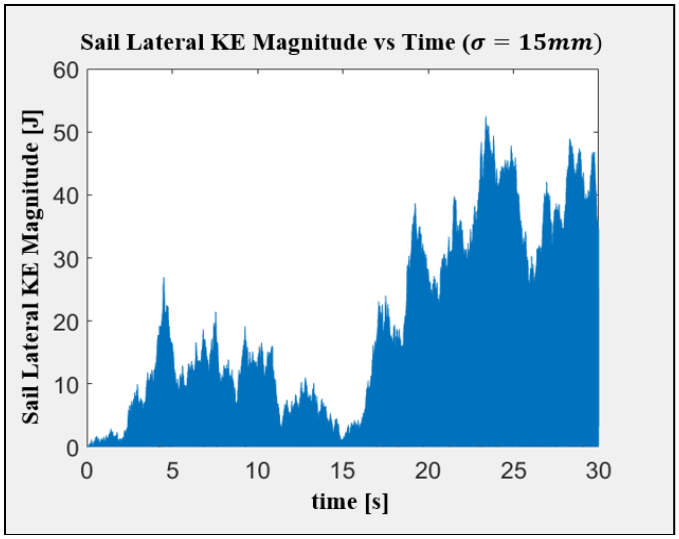

Figure 54 – Sail Lateral Kinetic Energy vs Time for a Single 1 second Simulation

The magnitude of KE_{lat} of sail over time for the simulation ran in Figure 52 is shown in Figure 54. By following the peaks of KE_{lat} for every cycle, the sail's cumulative energy (E_{lat}) can be tracked.

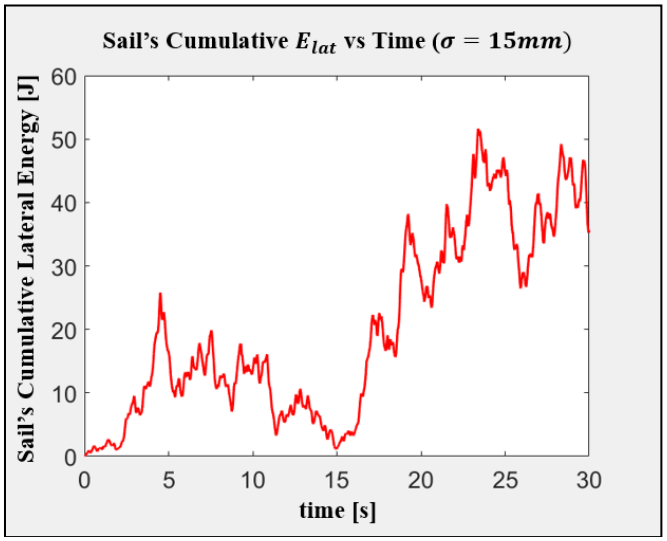

Figure 55 – Sail Lateral Kinetic Energy vs Time for a Single 1 second Simulation

The walk of sail's lateral energy above in Figure 55 is the energy Martingale derived from 1 simulation of the FSDNM. It can be seen that, for this particular simulation, the sail is dangerously close to escaping the beam. This is seen around 24 seconds when the E_{lat} maxed out to just about 15J below E_{esc}. However, this max value only represents 1 possible maximum E_{lat} value and does so for only one value of σ. It is also only a simulation of 1/20th the launch time of 10 minutes. However, the rate of growth of E_{lat} for a σ as small as 15mm is a troubling sight for a system with no method to perform active damping.

To obtain the Inverse Gaussian PDF for a given value of σ, the FSDNM must simulate several thousand martingales (like those in the right portion of Figure 48). Once complete, this process can be repeated with various σ values to identify the relationship between PDF and σ, and ultimately, the relationship between the Inverse Gaussian CDF and σ.

Unfortunately, the FSDNM takes about 6.5 minutes to simulate a single 30 second long martingale. If expanded to the necessary 600 seconds (10 minutes), iterated at least 1,000 times (to generate a distribution that has a low fitting error), and repeat for 5 different σ values, the time required to generate PDF(σ) would be 15 months. Due to the finite timescale of a master's degree, this is an infeasible task.

Fortunately, the mean (μ) and shape factor (λ) of the Inverse Gaussian PDF scale with simulated time. This means that the relationship between σ and PDF can be identified for shorter time period, and then can be scaled analytically to larger time scales. The range of simulated times (t_{sim}) and σ to be used by the FSDNM to generate $PDF(\sigma; t_{sim})$ are listed below. These combinations sum for a more modest 90 hours of computation.

$t_{sim} = 0.25, 0.5, 1, and\ 2\ [s]$	$\sigma = 15, 22, 33, and\ 66\ [mm]$

Table 3 – Inverse Gaussian PDF Independent Variables

For each of the above $t_{sim}; \sigma$ combinations above, 1000 E_{lat} martingales were generated. Figure 56 below depicts 20 of these E_{Lat} trajectories for $t_{sim} = 0.25s$ and $\sigma = 15mm$.

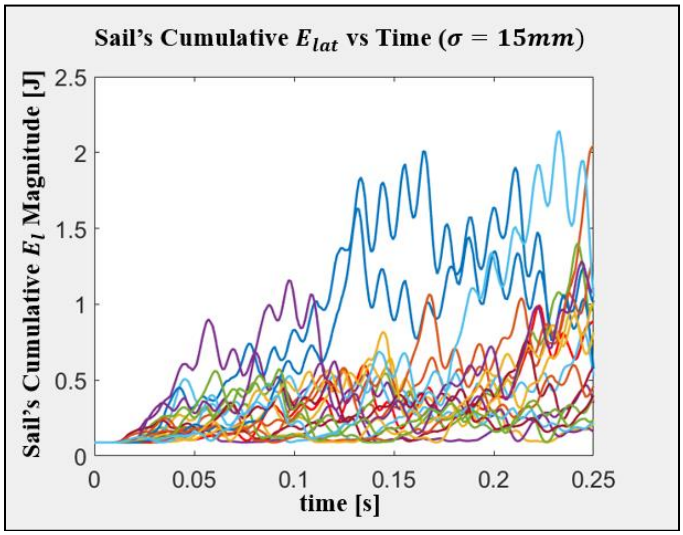

Figure 56 – 20 Simulated Lateral Energy Martingales for $\sigma = 15mm$ and $t_{sim} = 0.25s$

In the patterns above, the time scales simulated are small enough that the individual perturbances to the sail's lateral energy can be seen. The average peak-to-peak distance of the oscillations above is approximately equal to $1/f_T$.

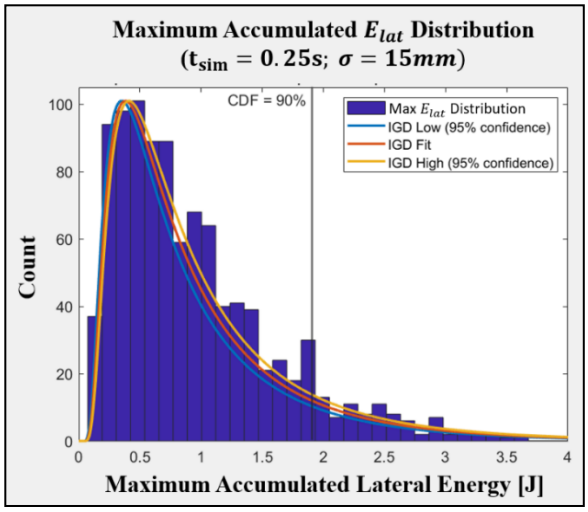

Figure 57 – Spiral Phase PSF Potential Well Shape for a 2m Sail

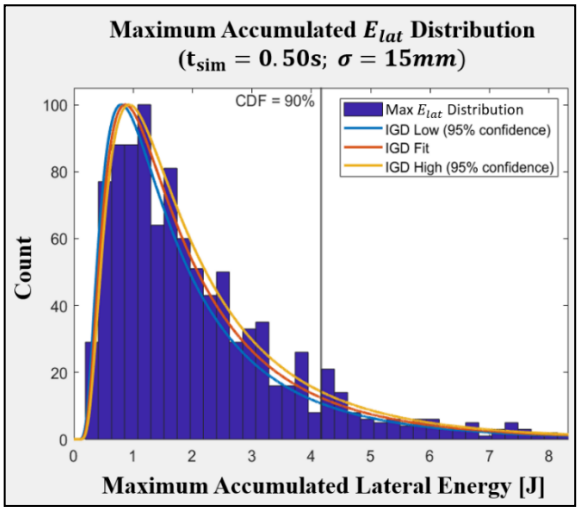

Figure 58 – Spiral Phase PSF Potential Well Shape for a 2m Sail

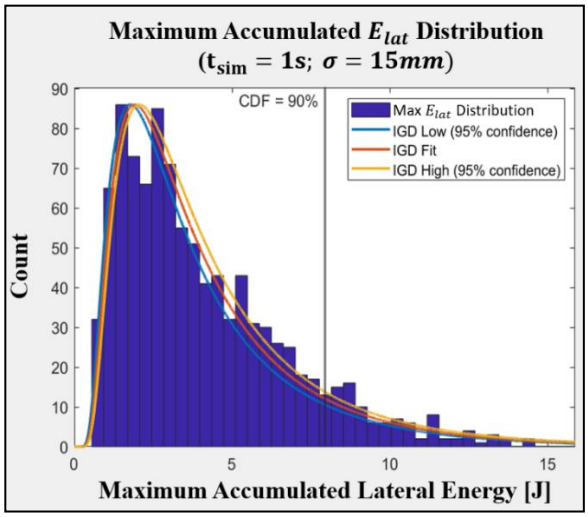

Figure 59 – Spiral Phase PSF Potential Well Shape for a 2m Sail

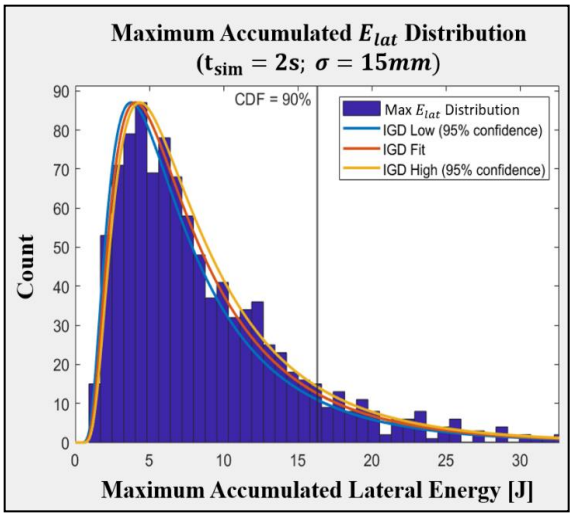

Figure 60 – Spiral Phase PSF Potential Well Shape for a 2m Sail

Figures 57-60 show the four PDF's fits the maximum accumulated E_{lat} given $\sigma = 15mm$. Each distribution was generated with the four t_{sim} values in Table 3. Integrating these PDF's generates their respective CDF. In each of the above four distributions, the E_{lat} that corresponds to the CDF's 90th percentile is marked. As the t_{sim} doubles, so too do the E_{lat} locations of CDF = 90%, roughly. This seems to demonstrate that the distribution of the maximum accumulated E_{lat} of a given σ increases linearly with time.

However, the increase in the 90th percentile could appear to be linear due to the small time difference between respective t_{sim} values, and with more data the fit could look much different. Although this is true, a linear fit is assumed because it represents the best case scenario and other

fits are expected to only exacerbate the growth of the 90th percentile. Given this best case scenario, expanding the CDF's 90th percentile out in time, the simulated time which brings the CDF's 90th percentile to the escape energy E_{esc} is $t_{sim} \approx 8\ seconds$. Because this is drastically below the 600 seconds of the launch period, it is nearly guaranteed that the sail will escape the beam given 15mm of beam decenter standard deviation (σ). This means that the Starshot's system is highly intolerant to tip errors.

Equation 39 can be used to put this in terms of OPD error. Using the largest distance the nanocraft reaches during its launch after 20 minutes as the limiting focal length in the following calculation ($f = r_{nano}(t = 10m) \approx 21{,}000\ Megameters$), the limiting tilt OPD is:

$$OPD_{tilt} = \delta_{decenter}\frac{D_L}{f} = 15mm * \frac{4km}{21{,}000Mm} \approx 3nm\ or\ 0.003\ waves$$

This limit is an unfathomably small amount of residual tilt error, and far exceeds what is expected to be possible within the timeline of the Starshot Program. Therefore, assuming the sail/beam geometry established at the beginning of this section, the nanocraft sail is not expected to ride stably within the beam without some method of dampening.

4. CONCLUSIONS

To determine the viability of a Satellite Laser Guide Star for use by the Starshot Adaptive Optics system, as well as studying the flight stability that would result from adaptive correction, several physical models were created and simulated.

Because of Rayleigh scattering in the Earth's atmosphere, the return light from the nanocraft cannot be used as a beacon source for wavefront detection for the first 30 seconds of launch. The proposed solution is to use a Satellite-based Laser Guide Star as the beacon for wavefront correction. This LGS would be attached to the Mothercraft that releases the Starshot nanocraft in orbit at the moment of launch. For this method to be viable, the satellite's orbit must be chosen such that its beacon does not contribute too much angular or focal anisoplanatic error to the adaptive correction.

To identify if such an orbit exists, a dynamic numerical orbital model was generated. This model simulates the 3D motions of the mothercraft, nanocraft, and launch projector as functions of time for various orbits. In so doing, it can track the amount of mean squared phase aberration the Starshot AO system would expect to have for each orbit.

After performing an optimization on a range of orbits, the set of parameters which are *unviable* for use by the Starshot SLGS are present in *yellow* below:

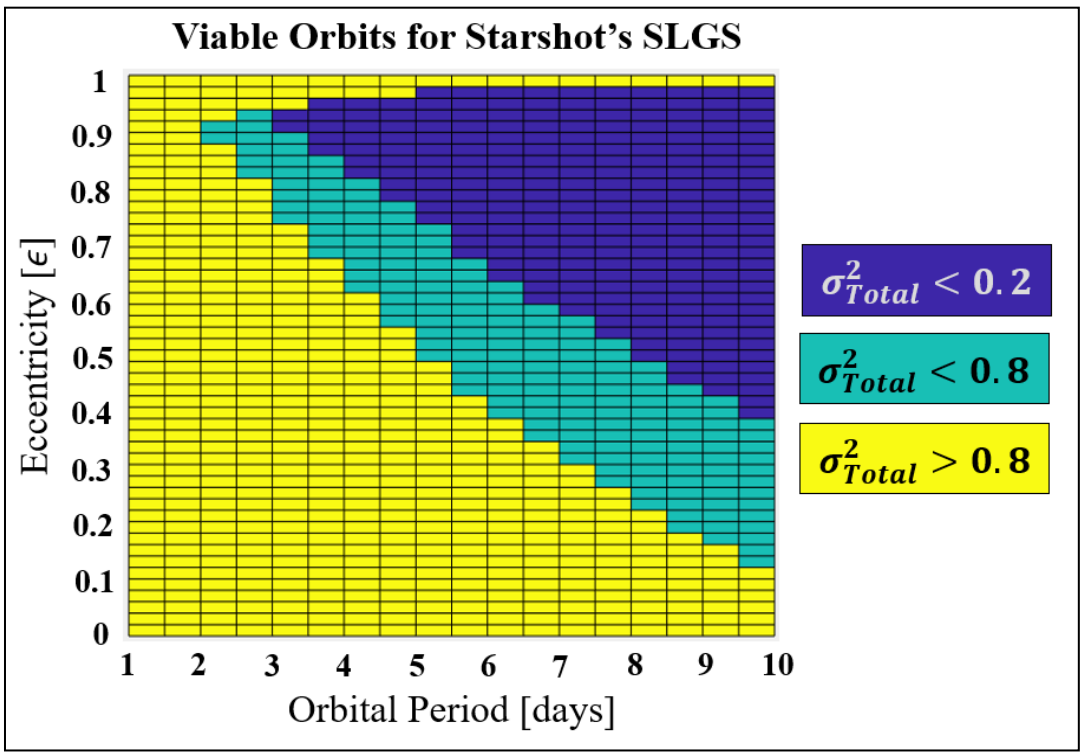

Figure 61 – Viable Orbits for Starshot's Satellite Laser Guide Star

In Figure 61, the parameters of orbits which are potentially viable to Starshot are depicted above in teal/blue. Teal represents those orbits which contribute less than $0.8\,rad^2$ phase aberration to the adaptive correction cause by angular and focal anisoplanatism after a 30 second launch period,

while those in blue contribute less than $0.2\ rad^2$. Because there exist a range of orbits which do not contribute too much angular and focal anisoplanatic error, the use of a Satellite Laser Guide Star for the first 30 seconds of launch is concluded to be a viable beacon configuration.

Next, the flight stability of the sail within the focus of the beam was analyzed. Because of the weight requirement on the nanocraft and its distance from the launch projector, its position relative to the optical axis must be passively stabilized. This can be done with the use of a spherical sail and the PSF of a spiral phase profile. This PSF, shaped like a donut, always draws the sail towards its dark center so long as the sail's lateral energy (Kinetic or Potential) does not exceed the escape energy of the potential well formed by the PSF's irradiance distribution. Because the sail's lateral energy is the sum of random perturbing forces throughout launch, a statistical model was created to determine the likelihood the sail will remain within the beam.

The created model states that the likelihood that a random perturbing force increases or decreases the sail's lateral energy are equal. This statistical equality leads to the random 'Brownian' walk of the sail's energy over time. The statistical distribution that describes the maximum accumulated lateral energy for a sail over a given time period is the Inverse Gaussian Probability Distribution Function (PDF). This PDF describes the likelihood that the nanocraft's sail will accumulate a certain amount of lateral energy during a launch given a certain distribution of perturbing forces. Analyzing a given PDF's Cumulative Distribution Function (CDF), the percentiles of success for a launch given a distribution of perturbing forces can be calculated. So long as the Sail's accumulated lateral energy CDF for a given distribution of perturbing forces is high when evaluated at the donut PSF's escape energy, it can be concluded that the likelihood the sail remains within the beam during launch is also high.

Using a dynamic numerical model similar to the one used on the SLGS mothercraft orbit, the lateral energy of the sail could be tracked given a distribution of perturbing forces, and its maximum accumulated energy PDF and CDF could be found. Assuming the primary perturbing force is a distribution of beam decenters over time, the sail's lateral energy PDF was determined for a perturbing decenter that is normally distributed with a mean $\mu = 0$ and standard deviation $\sigma = 15mm$.

15mm of beam decenter corresponds to an extremely small amount of tip error for the Starshot system, and initially was not expected to be a limiting perturbance magnitude. However, for this amount of perturbance, it was found that the sail is expected, with 90% confidence, to fall out of the beam within 8 seconds of launch (i.e. the sail is expected to accumulate $E_{lat} > E_{esc}$ before 8 seconds into launch for 90% of nanocraft launch). The Starshot system is extremely intolerant to beam tip/tilt errors given the beam/sail configuration $r_s = r_d$. 15mm decenter corresponds to a projector tilt OPD of only 3nm or 0.003waves, which is far beyond what the capabilities of adaptive correction are expected to achieve within the lifetime of the Breakthrough Starshot program. Although the Tyler Frequency assumed was quite large for a well-chosen astronomical site, the conclusions would not change given a more forgiving value. The "time-to-failure" of 8 seconds would change linearly with the inverse of the change in f_T. Although a decrease of f_T by a factor of 100 would bring the time-to-failure to 800 seconds (above the 10 minute requirement), this would only hold for the unfathomably tight OPD tolerance of 3nm, and increasing this tolerance would only decrease the time-to-failure by the same factor. Therefore, for this stability geometry to be viable, some method for dampening the energy of the sail will be necessary.

4.1 Future Work

As seen in Figure 31, the angular separation of the nanocraft and mothercraft only reaches approximately 1.3μrad after 30 seconds. Although this result shows that the SLGS is a viable beacon source for Starshot, it does not represent the global optimal orbit that minimizes angular separation over time. Future work will involve identifying if there exists a pair of globally optimized orbital parameters which keep this separation below θ_0 for the entire duration of the 10 minutes launch. This would greatly reduce the wavefront system's complexity by eliminating the second mode of operation for $t > 30s$.

With regards to flight stability, the sail's tolerance to tip/tilt error is expected to increase the larger the PSF's radius is to the sail's radius. As demonstrated in Figure 50, this scenario would increase the size of the PSF's potential well, and therefore, the stability of the sail. Unfortunately, this would decrease the power transfer coefficient between the projector and the sail. Future work should involve analyzing how the stability of the sail increases as the PSF's size increases, and an analysis should be performed to identify the economic impact of a lower power transfer coefficient.

Beyond the future work related to that presented in this thesis, there are lots of system design problems that need to be faced. Current priority problems already identified and to be addressed by the program's team include: what sail material can withstand 100 N of force while remaining less than 0.5 grams? How do you transmit data from a 0.5 gram nanocraft a distance of 4.25 lightyears with a sufficient receiver signal-to-noise ratio? And how do you co-phase several million 10 cm sub-apertures to create the propulsion beam? These three rather daunting problems represent just how ambitious Breakthrough Starshot is. To many, Starshot may seem like science fiction, but to date, no professional scientist or engineer has found any part of Starshot deemed impossible. Breakthrough Starshot represents this generation's Moonshot, a project that brings together teams from around the world to achieve a common goal that most thought not possible. Much like the Apollo program, the Breakthrough Starshot program will inevitably bring forth new science and technology and, more importantly, expand our view of the universe and our place within it.

APPENDIX A: TYLER FREQUENCY

As mentioned in Section 1.1.2, temporal mismatch between the frequency of the adaptive optics' correction loop and of the atmospheric turbulence can leave the corrected beam with residual wavefront error. However, this atmospheric Greenwood Frequency (f_G) considers all sizes of turbulent eddies, large and small, and as such, is a useful in determining how well a full-scale AO system will perform at a given correction speed. However, the analysis performed in Section 3 of this thesis considers only the effects of large-scale turbulence, namely tip/tilt, which changes with a frequency much slower than the Greenwood Frequency. The difference in frequency between "large" and "small" eddies is a result of the principle of inertia, and each *size* of turbulence has its own characteristic frequency at which it changes[12]. The more large-scale turbulence (tip/tilt) specific frequency is known as the *Tyler Frequency* (f_T) and is around 1/9th the Greenwood Frequency[32].

The specific values that these frequencies take depends on location, angle of observation, and wavelength. Hawaii's Mt. Haleakala site, one of the calmest atmospheric locations for astronomical observation, has a $f_G \approx 20\ Hz$, while less favorable sites could have frequencies as high as a few hundred or even a few thousand hertz. This value defines the slowest an AO system's correction loop can operate[13]. However, the portion of the correction loop which measures and corrects for tip/tilt (i.e. pointing) can operate at about 1/9th this frequency. Since the moment-to-moment change in the atmosphere's tip/tilt occurs at f_T, the frequency at which the Starshot nanocraft sail feels a perturbing force is expected to match f_T since tip/tilt affects a beam's lateral focus position. In Section 3, the f_T was assumed to be $100\ Hz$, with f_G being around $900\ Hz$. The effects of changing this value on the analysis results are discussed in the conclusions section.

REFERENCES

[1] P. Lubin, "A Roadmap to Interstellar Flight," *Journal of the British Interplanetary* Society, vol. 69, 2016.

[2] N. Kulkarni, P. Lubin and Q. Zhang, "Relativistic Spacecraft Propelled by Directed Energy," *The Astronomical Journal*, vol. 1555, no. 4, p. 155, 2017.

[3] Breakthrough Starshot Foundation, Breakthrough Starshot Animation (Full), YouTube (2016).

[4] M. Hart and O. Guyon, "Wavefront Sensing for the Breakthrough Starshot Laser Launch Projector - Proposal," Breakthrough Starshot Foundation, 2017.

[5] E. Hecht, "Chapter 11.3 - Fourier Optics," in Optics, 4rth ed., Addison-Wesley, 2002, pp. 529-532.

[6] E. Hecht, "Chapter 10.3 - Fraunhofer Diffraction," in Optics, 4rth ed., Addison-Wesley, 2002, pp. 469-472.

[7] J. C. Wyant and K. Creath, "Chapter 1 - Basic Wavefront Aberration Theory for Optical Metrology," in *Applied Optics and Optical Engineering*, Academic Press, 1992, pp. 35-39.

[8] R. K. Tyson, "Chapter 7 - Wavefront Sensors," in *Introduction to Adaptive Optics*, SPIE Press, 2000, pp. 73-75.

[9] R. K. Tyson, "Chapter 6 - Systems: Configurations of Adaptive Optics Systems," in *Introduction to Adaptive Optics*, SPIE Press, 2000, pp. 55-60.

[10] R. K. Tyson, "Chapter 5 - Laser Guide Stars," in *Introduction to Adaptive Optics*, SPIE Press, 2000, pp. 45-52.

[11] F. Kamphues, Artist, *Sodium LGS on UT4 at VLT*. [Art]. ESO, 2016.

[12] R. K. Tyson, "Chapter 4 - Atmospheric Turbulence: Anisoplanatism," in *Introduction to Adaptive Optics*, SPIE Press, 2000, pp. 42-45.

[13] R. P. Parenti, "Chapter 2 - System Design and Optimization," in *Adaptive Optics Engineering Handbook*, Dekker, 1999, pp. 29-56.

[14] R. K. Tyson and B. W. Frazier, *Field Guide to Adaptive Optics*, SPIE Press, 2012.

[15] R. K. Tyson, "Chapter 5 - Laser Guide Stars: Focal Anisoplanatism," in *Introduction to Adaptive Optics*, SPIE Press, 2000, pp. 50-53.

[16] A. Grivental, "Kepler's Laws and Conic Sections," *Arnold Mathematics Journal*, vol. 2, pp. 1388-148, 2016.

[17] O. Montenbruck, "Chapter 1 - Coordinate Systems," in *Practical Ephemeris Calculations*, Berlin, Springer-Verlag, 1989, pp. 1-39.

[18] J. Davis, "Of Inclinations and Azimuths," The Planetary Society, 12 April 2012. [Online]. Available: https://www.planetary.org/blogs/guest-blogs/jason-davis/3450.html.

[19] H. D. Curtis, "Chapter 3 - Orbital Positions as Functions of Time," in *Orbital Mechanics for Engineering Students*, Butterworth-Heinemann, 2013, pp. 145-186.

[20] P. B. Laval, "Rotation About an Arbitrary Axis [Math 4490 - Special Topics in Mathematics," Kennesaw State University, 2010

[21] H. D. Curtis, "Chapter 4 - Orbits in Three Dimensions," in *Orbital Mechanics for Engineering Students*, Butterworth-Heinemann, 2013, pp. 187-237.

[22] N. M. Sewdlow, "Kepler's Iterative Solution to Kepler's Equation," *Journal for the History of Astronomy*, vol. 31, pp. 338-341, 2000.

[23] E. J. Haug, "Preface," in *Computer-Aided Kinematics and Dynamics of Mechanical Systems*, Allyn and Bacon, 1989, pp. xi-1.

[24] H. D. Curtis, "Appendix C - Numerical Integration of the n-Body Equations of Motion," in *Orbital Mechanics for Engineering Students*, Butterworth-Heinemann, 2013, pp. 725-731.

[25] K. L. G. Parkin, "The Breakthrough Starshot System Model," *Acta Astronautica*, vol. 152, pp. 370-384, 2018.

[26] Strasbourg Astronomical Data Center, "Proxima Centauri Search Inquiry," SIMBAD Database, 2005. [Online]. Available: http://simbad.u-strasbg.fr/simbad/sim-id?Ident=Proxima+Centauri.

[27] R. Bustos, M. Rubio, A. Otarola and N. Nagar, "Parque Astronómico de Atacama: An Ideal Site for Millimeter, Submillimeter, and Mid-Infrared Astronomy," *Astronomical Society of the Pacific*, vol. 126, pp. 1126-1136, 2014.

[28] H. Riebeek, "Catalog of Earth Satellite Orbits," Earth Observatory, 4 September 2009. [Online]. Available: https://earthobservatory.nasa.gov/features/OrbitsCatalog.

[29] C. R. McInnes, "Chapter 2.3 - The Physics of Radiation Pressure," in *Solar Sailing: Technology, Dynamics, and Mission Applications*, Springer, 2005, pp. 34-40.

[30] M. Pasand, A. Hassani and M. Ghorbani, "A Study of Spacecraft Reaction Thruster Configurations for Attitude Control Systems," *IEEE Aerospace and Electronic Systems Magazine*, vol. 32, pp. 22-39, 2017.

[31] M. W. Beijersbergen, R. P. C. Coerwinkel, M. Kristensen and J. P. Woerdman, "Helical-Wavefront Laser Beams Produced with a Spiral Phaseplate," *Optics Communications*, vol. 112, pp. 321-327, 1994.

[32] G. A. Tyler, "Bandwidth Considerations for Tracking Through Turbulence," *Journal of the Optical Society of America*, vol. 11, 1194.

[33] D. C. Montgomery and G. C. Runger, "Chapter 7.2 - Sampling Distribution and the Central Limit Theorem," in *Applied Statistics and Probability for Engineers*, Wiley, 2019.

[34] M. A. Pinsky, "Chapter 2 - Conditional Probability and Conditional Expectation," in An *Introduction to Stochastic Modelling*, London Academic, 2011, pp. 47-58.

[35] C. Pacati, "Brownian Motion and Geometric Brownian Motion - Financial Mathematics 5002," University of Minnesota, 2001.

[36] S. Karlin and H. M. Taylor, "Chapter 8 - Brownian Motion and Related Processes," in *An Introduction to Stochastic Modelling*., London Academic, 2011, pp. 391-446.

[37] S. Sato and K. Inoue, "Inverse Gaussian Distribution and its Applications," *Electronics and Communications in Japan*, vol. 77, pp. 32-42, 1994.